Vilnius University
Center for physical sciences and technology

Andrius Gelžinis

Spectroscopy of photosynthetic molecular complexes. Theoretical modeling and analysis

Doctoral dissertation
Physical sciences, Physics (02P)

Vilnius, 2017

Doctoral dissertation was prepared at Vilnius University in 2013 – 2017, Vilnius, Lithuania.

Scientific supervisor:

prof. habil. dr. Leonas Valkūnas (Vilnius University, Physical sciences, Physics – 02P).

Vilniaus universitetas
Fizinių ir technologijos mokslų centras

Andrius Gelžinis

Fotosintetinių molekulinių kompleksų spektroskopija. Teorinis modeliavimas ir analizė

Daktaro disertacija
Fiziniai mokslai, fizika (02P)

Vilnius, 2017 metai

Disertacija rengta 2013 – 2017 metais Vilniaus universitete.

Mokslinis vadovas:

prof. habil. dr. Leonas Valkūnas (Vilniaus universitetas, fiziniai mokslai, fizika – 02P).

Acknowledgments

It takes ten hands to score a basket.

JOHN WOODEN

Yess, excellent. Teamwork and cooperation – those are the Predacon watchwords.

MEGATRON, The Transformers Beast Wars

First, I would like to thank my supervisor prof. Leonas Valkūnas for making this thesis possible. His guidance and teaching were invaluable and his motivational skills are truly without peer. I would also like to express my gratitude to prof. Darius Abramavičius, who generously shared his vast knowledge and experience and was very helpful to me, especially in the earliest part of my scientific career.

I also thank all my current and former colleagues in the Department of Theoretical Physics (VU) and the Department of Molecular Compound Physics (FTMC), especially, Juozas Bučinskas, Vytautas Butkus, Vytautas Balevičius Jr., Jevgenij Chmeliov, Vytautas Abramavičius, Vladimir Chorošajev, Ramūnas Augulis, Egidijus Songaila, and last but not least, Stepas Toliautas.

I must thank Jennifer Ogilvie, Bruno Robert, Donatas Zigmantas, Alexander Ruban and their groups for rewarding scientific collaborations.

Many of the computations presented in this thesis were performed using the resources of the High Performance Computing Center "HPC Saulėtekis" at Faculty of Physics, Vilnius University.

Personal thanks go to Gytis Bašinskas and Alina Lipovec.

Finally, I thank my family for the moral support during my long years of studies.

Contents

Common notations and abbreviations

t_2	waiting time
ω_1	excitation frequency
ω_3	detection frequency
2D	two-dimensional
2LS	two-level system
3LS	three-level system
CD	circular dichroism
Chl	chlorophyll
(I)CT	(intramolecular) charge transfer
cR	complex Redfield
ctR	complex time-dependent Redfield
(M)DAS	(modified) decay associated spectra
ESA	excited state absorption
ESE	excited state emission
FCP	fucoxanthin–chlorophyll protein
(Δ)FLN	(Δ) fluorescence line-narrowing
FWHM	full width at half maximum
Fx	fucoxanthin
GSB	ground state bleaching
HEOM	hierarchical equations of motion
HOMO	highest occupied molecular orbital
LD	linear dichroism
LHCII	major light-harvesting complex of higher plants
LO	local oscillator
LUMO	lowest unoccupied molecular orbital
ME	molecular excitation
mR	modified Redfield
Pheo	pheophytin
PSII	photosystem II
RC	reaction center
sR	standard Redfield

Introduction

Sometimes it is hell trying to get to heaven.

THE UNDERTAKER

Throughout the ages all living organisms on Earth have used Sun as the main energy source. The most important metabolic process that occurs in plants, algae and bacteria is photosynthesis. It begins with the absorption of solar light by specific pigments, (bacterio)chlorophylls and carotenoids, which are bound to light-harvesting proteins. Subsequently the energy is transferred to the reaction centers. There the excitation triggers a fast charge separation, through which the excitation energy is transduced into chemical potential. The latter then is used for the production of sugars. Additionally, oxygenic photosynthesis also provides oxygen as a byproduct, making it invaluable to support living conditions for mankind on the planet [1, 2].

Despite tremendous progress, a lot of open questions on the timescales and mechanisms of excitation energy transfer and charge separation in the photosynthetic systems – light-harvesting antennae complexes, reaction centers and whole photosystems – remains. Therefore, photosynthesis research is among many scientific fields in physics, chemistry, and biology that requires the development of time-resolved spectroscopic methods with the highest time resolution possible [3, 4]. Between the mid-'70s and the mid-'90s, following the development of the pulsed lasers, the nano- and picosecond time domains became accessible to the pump–probe spectroscopy [5–10]. This technique provided mountains of information about the timescales of the processes involved.

Yet the higher time resolution is desired, the shorter must be the laser pulses used in the experiments. Unfortunately, due to the Heisenberg uncertainty principle, the shorter the laser pulse, the less defined is its energy. Thus, achieving exact selective excitation with high temporal resolution is a fundamentally challenging task. To circumvent this unavoidable limit, an echo technique, now termed two-dimensional (2D) electronic spectroscopy, was formulated at the

turn of the century, which provides information on the evolution of the system with both high time (reaching tens of femtoseconds) and spectral resolutions [11]. This technique has now been widely employed for studies of light-harvesting antennas and photosystems [12–19] and led to a number of breakthroughs in the field. Naturally, it has also been applied to other systems, like atomic vapors [20], semiconductor nanostructures [21] or photoreactive molecular species [22] to name only a few. In case the longer timescales are of interest, experimentalists can safely turn to less complicated techniques, such as time resolved fluorescence [23]. Extraction of the relevant information from the ever increasing mountains of experimental data requires understanding of fundamental photophysical processes.

Upon light absorption, separate molecules undergo a transition from the ground state to their excited states. In aggregated conditions molecules with similar optical properties can interact (even strongly) electrostatically although they might not even be in a "physical" contact. In this case new collective energy levels are created with transitions to these levels being (partly) allowed and/or (partly) forbidden since excitations are intimately shared between molecules in the aggregate [24, 25]. Absorption and fluorescence properties of such collective excitations known as Frenkel excitons depend on the relative orientations and positions of the interacting molecules. They are, however, not the only possible excitations in the photosynthetic complexes. Charge transfer (CT) states, relevant in the reaction centers, have to be taken into account to describe charge separation. In this case, electrons and holes are not bound together but can be on separate pigments. Taking CT states into account can severely complicate the theoretical description [26, 27].

Spectral and dynamical properties of the photosynthetic molecular aggregates reflect a complex interplay of electronic excitations interacting with intra- and intermolecular vibrations. These systems are thus an example of open quantum systems [28, 29] sharing similar properties with other systems from the fields of condensed matter and even quantum computing. Theoretically, the key issue is being able to describe both intermolecular interaction and interaction with vibrations on equal footing. In case one type of interaction is weaker than the other, perturbative approaches can be applied [30, 31]. They can reliably and without prohibitive computational costs describe both the dynamics and the spectral properties of the system. Nonetheless, sometimes the accuracy of even similar methods varies widely, thus investigations of known and development of new methods are always needed.

Applications of microscopic theoretical models on real molecular systems, however, are heavily dependent upon the availability of the structural data. Since 1984, when the crystal structure of the bacterial reaction center was first obtained [32], the amount and quality of the structural data improved substantially [33–38]. It is a foundation for all the microscopic models, as it allows calculations of molecular transition dipole moments and the resonance couplings [39]. If no structural data is available, as is the case for the fucoxanthin–chlorophyll protein (FCP) complex from diatoms, only basic and phenomenological models are possible.

Having all this in mind, what is a theorist to do? How can he contribute towards the understanding of the processes in the photosynthetic molecular complexes and their dynamical and spectroscopic properties?

The answer to this question is threefold. First, for systems with no structural data available a theorist can use his knowledge of the system to make detailed analysis of the experimental data and construct simple effective models (see Chapter 1). Second, a theorist can develop general microscopic models and accompanying theories (see Chapter 2). Third, a theorist can apply the relevant models and theories to describe a concrete system by explaining specific experimental data (see Chapter 3). This thesis is the author's attempt to contribute to all three of these areas.

Main goal and tasks of the research work

The **main goal** of this research work is to uncover the identity and properties of the microscopic molecular states participating in the energy transfer and charge separation in the photosynthetic molecular complexes. In order to achieve this goal, the following tasks were formulated:

- Perform a detailed analysis and effective modeling of the experimental two-dimensional spectra of the fucoxanthin–chlorophyll protein complex.

- Develop an accurate but computationally efficient theoretical approach suitable for the calculation of the optical lineshapes of the photosynthetic molecular complexes.

- Develop a tight-binding model of the photosystem II reaction center capable of explaining its linear and non-linear spectra.

Novelty and relevance of the results

Diatoms are a major group of algae, that account for up to a quarter of global primary production. They absorb efficiently in the blue–green spectral region. This is usually ensured by the carbonyl-containing carotenoid molecules, such as peridinins or fucoxanthins. The FCP complex is the main complex of the light-harvesting antenna of diatoms. Characterizing the electronic excitation dynamics in FCP is a particularly challenging task because of a large number of molecules and electronic levels involved. Previously, FCP was investigated using the pump–probe spectroscopy [40–43]. The present thesis summarizes the analysis of the *first* ever 2D spectroscopy experiments of FCP. These results provide important insights to the structural organization of the FCP complex and the energy transfer cascades therein.

Understanding of complex spectroscopic features of the photosynthetic molecular complexes requires the ability to model optical lineshapes. This issue was investigated thoroughly in literature, and exact [44, 45] and approximate [45–53] methods exist. A non-Markovian approach has been derived in the work by Renger and Marcus [47], yet it has never been used in actual calculations. This thesis presents this complex time-dependent Redfield (ctR) theory and shows its advantages over other perturbative methods. In addition, expressions for calculations of both Stark and 2D spectra within the ctR theory are derived here for the *first* time.

Photosystem II (PSII) is the only known biological complex capable of splitting water, thus it is the source of oxygen to all living beings on the planet Earth. The reaction center (RC) of the PSII is responsible for the primary charge separation. Despite intensive studies [54–61], the pathways of charge separation and the identities of the participating states are still under debate. This thesis reports a tight-binding model of the PSII RC with parameters derived from the fits of optical spectra using the ctR theory, applied to the spectroscopic analysis of the PSII RC for the *first* time. Simulations of Stark spectrum are reported, allowing insights to the properties of the charge transfer states in the PSII RC. Additionally, a proof of concept calculations demonstrate how coupling to vibrations can enhance the charge separation.

Statements of the thesis

1. Analysis of the experimental 2D spectroscopy data of the FCP complex, supplemented with theoretical insights and representation in terms of suitable decay associated spectra, enabled to propose both a possible structural scheme and a detailed scheme of energy transfer pathways.

2. Accounting for the lifetime broadening with complex and time-dependent terms significantly improves the quality of spectroscopic lineshapes, when the lineshape function formalism is used. Neglecting the imaginary part means ignoring the time-dependent reorganization and thus induces non-uniform peak shifts, while the Markovian approximation assumes relaxation independent of bath state and thus reduces the overall accuracy of the calculated lineshapes.

3. By using the ctR theory the characteristics of the PSII RC were determined from a fit of multiple spectroscopic data. The primary CT state is identified to be $\mathrm{Chl}^{+}_{\mathrm{D1}}\mathrm{Pheo}^{-}_{\mathrm{D1}}$ from the fits of the Stark spectrum.

Author's contribution and approbation of the results

This thesis is based upon the results that have been presented in seven published and two, as of the time of writing, not yet published scientific papers:

[**P1**] V. Butkus, D. Abramavicius, A. Gelzinis, and L. Valkunas, "Two-dimensional optical spectroscopy of molecular aggregates", Lith. J. Phys. **50**, 267–303, 2010.

[**P2**] A. Gelzinis, L. Valkunas, F. D. Fuller, J. P. Ogilvie, S. Mukamel, and D. Abramavicius, "Tight-binding model of the photosystem II reaction center: application to two-dimensional electronic spectroscopy", New J. Phys. **15**, 075013, 2013.

[**P3**] E. Songaila, R. Augulis, A. Gelzinis, V. Butkus, A. Gall, C. Büchel, B. Robert, D. Zigmantas, D. Abramavicius, and L. Valkunas, "Ultrafast energy transfer from chlorophyll c_2 to chlorophyll a in fucoxanthin–chlorophyll protein complex", J. Phys. Chem. Lett. **4**, 3590–3595, 2013.

[**P4**] F. D. Fuller, J. Pan, A. Gelzinis, V. Butkus, S. S. Senlik, D. E. Wilcox, C. F. Yocum, L. Valkunas, D. Abramavicius, and J. P. Ogilvie, "Vibronic coherence in oxygenic photosynthesis", Nat. Chem. **6**, 706–711, 2014.

[**P5**] A. Gelzinis, V. Butkus, E. Songaila, R. Augulis, A. Gall, C. Büchel, B. Robert, D. Abramavicius, D. Zigmantas, and L. Valkunas, "Mapping energy transfer channels in fucoxanthin–chlorophyll protein complex", Biochim. Biophys. Acta **1847**, 241–247, 2015.

[**P6**] V. Butkus, A. Gelzinis, R. Augulis, A. Gall, C. Büchel, B. Robert, D. Zigmantas, L. Valkunas, and D. Abramavicius, "Coherence and population dynamics of chlorophyll excitations in FCP complex: Two-dimensional spectroscopy study", J. Chem. Phys. **142**, 212414, 2015.

[**P7**] A. Gelzinis, D. Abramavicius, and L. Valkunas, "Absorption lineshapes of molecular aggregates revisited", J. Chem. Phys. **142**, 154107, 2015.

[**p8**] A. Gelzinis, R. Augulis, V. Butkus, B. Robert, and L. Valkunas, "Two-dimensional spectroscoy for biologists: application to fucoxanthin–chlorophyll protein complex", in preparation.

[**p9**] A. Gelzinis, D. Abramavicius, J. P. Ogilvie, and L. Valkunas, "Spectroscopic properties of photosystem II reaction center revisited", submitted to J. Chem. Phys.

The author of this thesis is a theorist. He therefore claims no credit for the experimental work presented here, as it was performed by the experimentalist colleagues. Analysis of the experimental data was always a group effort. The theoretical work was done in a close collaboration with the supervisor and other theorists, making exact attributions difficult. Nonetheless, here the author lists the work that he feels he can safely be credited with. For [**P1**], the author contributed a part of calculations. For [**P2**], the author formulated the model, performed all the calculations and did most of the writing. For [**P3**], the author performed all the calculations, and contributed substantially to the analysis of the experimental data and the writing. For [**P4**], the author performed part of the calculations. For [**P5**], the author performed most of the detailed analysis of the experimental data and did most of the writing. For [**P6**], the author participated in the analysis of the experimental data and contributed to the writing. For [**P7**], the author contributed the idea, performed all the calculations and did most of the writing. For [**p8**] the author performed the majority of manuscript preparation. For [**p9**], the author performed all the calculations and theoretical work, and wrote the majority of the paper.

The author has also co-authored a number of papers that are not included into this thesis:

1. V. Butkus, A. Gelzinis, L. Valkunas, "Quantum coherence and disorder-specific effects in simulations of 2D spectra of one-dimensional J-aggregates", J. Phys. Chem. A **115**, 3876-3885, 2011.

2. A. Gelzinis, D. Abramavicius, L. Valkunas, "Non-Markovian effects in time-resolved fluorescence spectrum of molecular aggregates: tracing polaron formation", Phys. Rev. B **84**, 245430, 2011.

3. V. Balevičius Jr., A. Gelzinis, D. Abramavicius, T. Mančal, L. Valkunas, "Excitation dynamics and relaxation in a molecular heterodimer", Chem. Phys. **404**, 94-102, 2012.

4. V. Balevičius Jr., A. Gelzinis, D. Abramavicius, L. Valkunas, "Excitation energy transfer and quenching in a heterodimer: Applications to the carotenoid–phthalocyanine dyads", J. Phys. Chem. B **117**, 11031-11041, 2013.

5. V. Chorošajev, A. Gelzinis, L. Valkunas, D. Abramavicius, "Dynamics of exciton-polaron transition in molecular assemblies: The variational approach", J. Chem. Phys. **140**, 244108, 2014.

6. J. Chmeliov, A. Gelzinis, E. Songaila, R. Augulis, C. D. P. Duffy, A. V. Ruban, L. Valkunas, "The nature of self-regulation in photosynthetic light-harvesting antenna", Nat. Plants, **2**, 16045, 2016.

7. V. Chorošajev, A. Gelzinis, L. Valkunas, D. Abramavicius, "Benchmarking the stochastic time-dependent variational approach for excitation dynamics in molecular aggregates", Chem. Phys., **481**, 108-116, 2016.

8. J. Pan, A. Gelzinis, V. Chorošajev, M. Vengris, S. S. Senlik, J.-R. Shen, L. Valkunas, D. Abramavicius, J. P. Ogilvie, "Ultrafast energy transfer within the photosystem II core complex", Phys. Chem. Chem. Phys., **19**, 15356-15367, 2017.

The results of the thesis were presented at the following conferences:

1. A. Gelžinis, L. Valkūnas, D. Abramavičius, "Antrosios fotosistemos reakcinio centro dvimatė optinė spektroskopija, 40-oji Lietuvos nacionalinė fizikos konferencija", Vilnius, 2013.

2. A. Gelzinis, V. Butkus, E. Songaila, R. Augulis, A. Gall, C. Büchell, B. Robert, D. Abramavicius, D. Zigmantas, L. Valkunas, "Energy transfer pathways in fucoxanthin–chlorophyll protein complex revealed by two

dimensional optical spectroscopy", 11th Nordic Femtochemistry conference 2014, Vilnius, 2014.

3. A. Gelzinis, V. Butkus, E. Songaila, R. Augulis, A. Gall, C. Büchell, B. Robert, D. Abramavicius, D. Zigmantas, L. Valkunas, "Mapping energy transfer flow in fucoxanthin–chlorophyll protein complex", Workshop on Ultrafast Processes in Photosynthesis. New Vistas at ELI-ALPS, Szeged, Hungary, 2014.

4. A. Gelzinis, V. Butkus, E. Songaila, R. Augulis, A. Gall, C. Büchell, B. Robert, D. Abramavicius, D. Zigmantas, L. Valkunas, "Insights to excitation energy transfer in fucoxanthin–chlorophyll protein complex using two-dimensional electronic spectroscopy", Light-Harvesting Processes, Banz, Germany, 2015.

5. A. Gelžinis, V. Butkus, E. Songaila, R. Augulis, A. Gall, C. Büchell, B. Robert, D. Abramavičius, D. Zigmantas, L. Valkūnas, "Energijos pernaša ir koherentiniai reiškiniai fukoksantinų ir chlorofilų baltyminiame komplekse", 41-oji Lietuvos nacionalinė fizikos konferencija, Vilnius, 2015.

6. A. Gelzinis, S. S. Senlik, J. P. Ogilvie, D. Abramavicius, L. Valkunas, "New simulations of 2D spectra of photosystem II reaction center", The 8th International Conference on Coherent Multidimensional Spectroscopy, CMDS 2016, Groningen, The Netherlands, 2016.

7. A. Gelzinis, J. P. Ogilvie, D. Abramavicius, L.Valkunas, "Spectroscopic properties of photosystem II reaction center revisited", Light-Harvesting Processes, Banz, Germany, 2017.

Chapter 1

Overview of 2D spectroscopy

> Information is victory. One cannot and should not dismiss any data as inconsequential until one is in a position to evaluate its significance, and that only comes with hindsight. So all detail is important until circumstances render it redundant.
>
> ROBOUTE GUILLIMAN in "Know No Fear"
> by Dan Abnett

This chapter is dedicated to the introduction of the 2D electronic spectroscopy and its applications to the FCP complex. Therefore, it is divided into two major parts. In the first part, we introduce the basics of the 2D spectroscopy, discuss its experimental implementations, the most important features visible in the 2D spectra, and different ways of analyzing the experimental data. In the second part, we present the key findings from the 2D spectroscopy studies of the FCP complex, namely a discovery of two chlorophyll (Chl) *c* molecules, with their excited states exhibiting completely different evolution, and the characterization of two spectroscopically distinct fucoxanthin (Fx) species in the complex.

1.1 From pump–probe to 2D spectroscopy

The usual goal of a multidimensional spectroscopic technique is to provide data that is resolved in excitation frequency, detection frequency, and time. This type of data is most naturally represented as time-resolved 2D maps, with one axis representing the excitation, and the other – the detection frequency resolution. Different approaches have their own advantages and disadvantages, relating to resolution, noise, etc. In this section, we will provide a short overview of several

a) Pump–probe spectroscopy

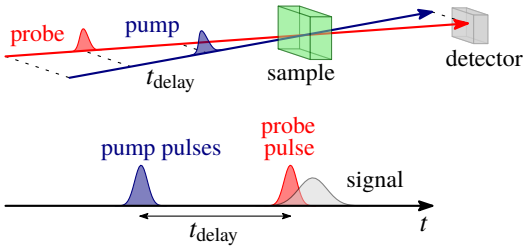

To obtain 2D maps:
Scan t_{delay} and ω_{pump}
Stack obtained spectra

Features:
× Dependent time and frequency resolutions
× Background signals

b) Homodyne transient grating spectroscopy

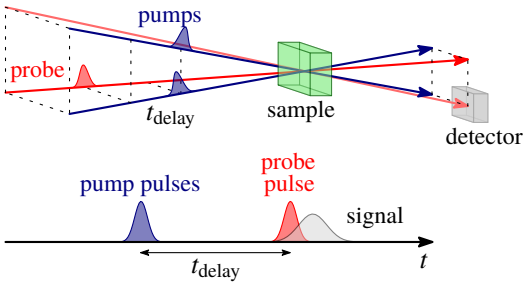

To obtain 2D maps:
Scan t_{delay} and ω_{pump}
Stack obtained spectra

Features:
× Dependent time and frequency resolutions
✓ Background free

c) Colinear self-heterodyne 2D spectroscopy

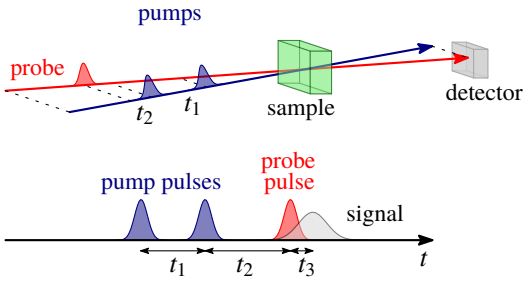

To obtain 2D maps:
Scan t_1, t_2 and t_3
Perform Fourier transform over t_1 and t_3

Features:
✓ Independent time and frequency resolutions
× Background signals

d) Non-colinear heterodyne 2D spectroscopy

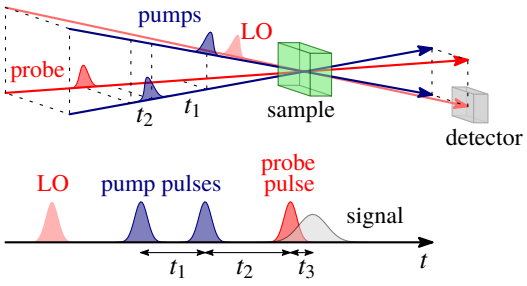

To obtain 2D maps:
Scan t_1, t_2 and t_3
Perform Fourier transform over t_1 and t_3

Features:
✓ Independent time and frequency resolutions
✓ Background free

Figure 1.1: Schematical presentation of multidimensional spectroscopies that can provide excitation frequency, detection frequency and time resolved information. a) pump–probe spectroscopy. b) homodyne transient grating spectroscopy. c) colinear self-heterodyne 2D spectroscopy. d) non-colinear heterodyne 2D spectroscopy. Top left (all parts), the spatial arrangement of the pulses, the sample and the detector; bottom left (all parts), the temporal arrangement of the pulses and the signal; right (all parts), procedure to obtain the 2D maps and the characteristic features of the technique.

types of spectroscopies, from the conventional pump–probe spectroscopy to the non-colinear heterodyne 2D spectroscopy. To this end, in Fig. 1.1 we present the principal schemes of the relevant experimental techniques, together with a short description on how to obtain the time-resolved 2D maps and the advantages and disadvantages of particular approaches. Similar description was presented in a recent review of the experimental implementations of the 2D spectroscopy [62].

In Fig. 1.1a we present the principle scheme of the pump–probe spectroscopy. First, a strong pump pulse (often narrow-band) with central frequency ω_{pump} excites the sample. Then, after a delay time t_{delay}, a weak probe pulse (usually spectrally wide) probes the sample, and the resulting signal is recorded by a detector. A single experimental run thus gives a linear spectrum that represents a broadband detection after t_{delay} has passed since the excitation of the sample with ω_{pump}. Repeating experiments with different ω_{pump} allows one to stack the obtained spectra and to depict a 2D map corresponding to a specific t_{delay}. To observe the temporal dynamics, one then has to repeat the procedure for different t_{delay}. In this way the system dynamics after excitation can be followed. Nonetheless, this scheme suffers from two major drawbacks. The first one is due to the interdependence of the time and excitation frequency resolutions. Narrow-band pulses, which are required for a selective excitation, have wide envelopes in the time domain, obscuring the observed dynamics. Conversely, one can use a wide-band pulse, but then no selective excitation is possible. In practice this means that this technique is suitable when the studied spectral features are well-separated or the timescales of the processes are not too short. Another disadvantage of this technique is that it is not background-free, since the probe pulse and the signal arrive at the detector from the same direction. Therefore, the signal-to-noise ratio is limited, and observation of weak features becomes difficult.

The latter drawback can be circumvented by the transient grating spectroscopy, illustrated in Fig. 1.1b. This is done by dividing a single pump pulse into two, which have different spatial directions. In this way, after the interaction with the probe, the sample emits the signal in the phase matching direction that differs from the probe pulse, thus detector is not polluted by the background signals. The situation can be interpreted as the pump pulses creating a grating of matter response, and the probe pulse undergoing a Bragg diffraction, resulting in the emitted signal at different direction. In this technique the 2D maps are obtained in the same way as in the pump–probe configuration. Correspondingly, the issue of interdependence of the excitation frequency and time resolutions

remains.

Excitation frequency and time resolutions can be decoupled using the Fourier transform methodology [11]. The simplest experimental implementation of this approach results in the colinear self-heterodyne 2D spectroscopy [63], illustrated in Fig. 1.1c. The difference from the pump–probe spectroscopy is that the pump pulse is split into two pulses (using a pulse shaper, for example) with the same wavevector. This gives additional adjustable time delay. Following the accepted nomenclature, the delay between the pump pulses is often called the coherence time and denoted by t_1, the delay between the second pump pulse and the probe pulse is called the waiting time and is denoted by t_2 (it corresponds to t_{delay} in the pump–probe and transient grating experiments), and the delay between the probe pulse and the registered signal is called the detection time and is denoted by t_3. Thus, differently from the pump–probe and transient grating experiments, the excitation frequency resolution is obtained not by scanning the central frequency of the pump pulse, but instead by employing narrow-band pulses, scanning the t_1 delay between the pump pulses, and applying the Fourier transform over it. To obtain the 2D maps at different waiting times t_2, also the t_3 delay has to be scanned and the corresponding Fourier transform (over t_3) applied. Often this is unnecessary, as spectrally dispersed signals are measured directly. The excitation frequency is denoted as ω_1, and the detection frequency – as ω_3. This approach therefore avoids the interdependence of the excitation frequency and time resolution, as the employed pulses can be as narrow as possible. Nevertheless, because of the pump–probe geometry, this technique still suffers from background signals.

By combining the ideas from both the transient grating and the colinear 2D spectroscopy, one comes to the non-colinear heterodyne 2D spectroscopy, illustrated in Fig. 1.1d. Here the pump pulses are separated both in spatial direction and in time. Thus, both the decoupling of excitation frequency and time resolutions (because of Fourier transform methodology) and the removal of background signals (by detecting in direction different from the probe pulse) is achieved. Moreover, one often employs an additional local oscillator (LO) pulse, to ease the detection. The 2D maps are obtained by scanning the delays t_1, t_2 and t_3, and performing the corresponding Fourier transforms over t_1 and t_3. This technique is the current state of the art, and this is what we will have in mind when we refer to the *2D spectroscopy* later in the text. Note that formally one can distinguish between the so-called rephasing and non-rephasing 2D spectra. These are related to signals emitted to different directions, see Ref. [**P1**]. In

this work, however, we will focus on the so-called total 2D spectrum, which is purely absorptive and is a sum of rephasing and non-rephasing contributions.

In this section we presented the different spectroscopic techniques schematically, highlighting only the most important differences. More details can be found in [31, 62, 64, 65].

1.2 Basic principles of 2D spectroscopy

In the previous section, we introduced the experimental basis of the 2D spectroscopy. In this section, its basic concepts, notation and conventions will be explained using the schematic representations shown in Figs. 1.2-1.9.

1.2.1 2D spectra of model systems

1.2.1.1 Single two- (or three-) level system

First, let us consider a two-level system (2LS) as the simplest model usually used to describe the optical transitions in a monomer. The 2LS is characterized by two energy levels, the ground state g and the excited state e. Therefore, the single parameter defining this system is the difference between the energies of these levels ω_{eg} (which coincides with the transition frequency), as shown on the left of Fig. 1.2a. Here and in the rest of the thesis we set $\hbar = 1$ and use frequency units for the energy. The 2D spectrum of such system at zero waiting time ($t_2 = 0$) is displayed in the central part of Fig. 1.2a. The horizontal axis corresponds to the excitation frequency, ω_1, which increases from left to right, and the vertical axis corresponds to the detection frequency, ω_3, which increases from down to up. This is the most often used convention, but sometimes 2D spectra are plotted with excitation and detection axis interchanged, or using wavelength instead of frequency. Also note that there is no universal agreement on the number and the exact positioning of the contour lines. Throughout this thesis we employ a linear scale (with a single exception being Fig. 1.11) with solid lines for positive and dashed lines for negative amplitudes. Also, there is no universal color scheme used to represent the 2D data, though the scheme employed here is encountered often in literature.

In the 2D spectrum given here, only one positive peak is visible, corresponding to the transition between the ground and excited states and determined by the ground state bleaching (GSB) and the excited state emission (ESE) contributions. Their physical origin is the same as in the pump–probe spectroscopy. It is

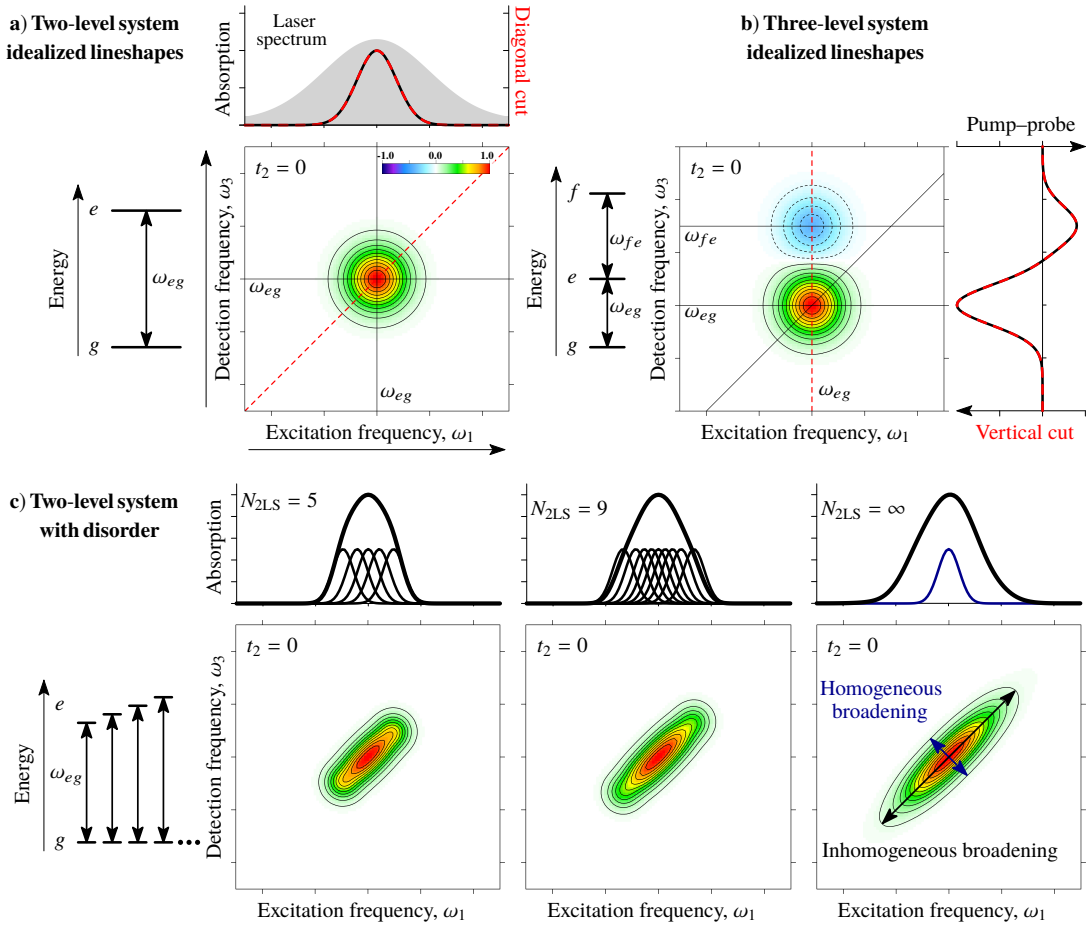

Figure 1.2: Example of the 2D spectra of the simplest electronic systems. a) left, energy level diagram of a 2LS; top, the absorption spectrum of the system (black solid line), along with the assumed laser spectrum (gray filled curve) and a diagonal cut of the 2D spectrum (red dashed line); center, the 2D spectrum of a 2LS with an idealized lineshape at zero waiting time. b) left, an energy level diagram of a 3LS; center, the 2D spectrum of a 3LS with an idealized lineshapes at zero waiting time; right, a vertical cut of the 2D spectrum (red dashed line) and the pump–probe spectrum of the system (solid black line). c) left, the energy level diagram of a 2LS with disorder (inhomogeneous ensemble of 2LSs); right, the 2D spectrum of an ensemble of 5, 9, or ∞ 2LSs at zero waiting time; top, absorption spectra of the corresponding ensembles (thick solid lines) and the constituents (thinner black or blue lines).

centered at ω_{eg} in both the excitation and detection axis. Note that the peak here is presented with an idealized lineshape, which is a two-dimensional Gaussian. For this system the 2D spectra remain constant throughout the waiting time t_2. On the top side of Fig. 1.2a the absorption spectrum of this system is displayed by the solid black line. The laser spectrum is chosen to entirely cover the absorption spectrum of the system (this is also assumed in other figures of this section, unless explicitly noted otherwise) and is given by the gray filled curve. For a 2LS, the diagonal cut (with $\omega_1 = \omega_3$) of the 2D spectrum at zero waiting time can be scaled to perfectly match the absorption spectrum, as shown by the dashed red line.

A slightly more complicated example is a three level system (3LS), which is illustrated in Fig. 1.2b. On the left we show the energy level diagram, which, in addition to the ground state g and the excited state e, also contains the higher excited state f. The energy difference between states f and e is ω_{fg}, which is here assumed to be larger than ω_{eg}. In the central part of Fig. 1.2b we show the corresponding 2D spectrum at zero waiting time. In this case, besides the positive peak, a negative peak is also present, centered at excitation frequency ω_{eg} and detection frequency ω_{fe}. This peak is due to the excited state absorption (ESA), thus it has a negative amplitude. Note, that this sign convention is opposite to the sign used in the pump–probe spectroscopy, as is shown on the right side of Fig. 1.2b. For this simple system the vertical cut of 2D spectrum (red dashed line) can be scaled to match the sign inverted pump–probe spectrum (black line).

Usually, the 2D spectroscopy is performed on a sample consisting of an inhomogeneous ensemble of systems. Constituent molecules often have different electronic excitation energies, due to the slow degrees of freedom of their surroundings (solvent or protein). The system is then considered as having energetic disorder. This affects the 2D spectra of a simple 2LS as shown in Fig. 1.2c. The energy level diagram illustrates a large number of non interacting 2LSs with similar transition frequencies, composing the observed system. The 2D spectra of ensembles of increasing number of 2LSs ($N_{2\mathrm{LS}}$ equal to 5, 9 or ∞) are displayed (right panel), with the corresponding absorption spectra shown above. When $N_{2\mathrm{LS}} = 5$, the absorption spectrum is a sum of 5 one-dimensional Gaussians (given by thinner lines), while the 2D spectrum is a sum of 5 two-dimensional Gaussians centered at different frequencies on the diagonal. Therefore, the 2D peak lineshape becomes elongated along the diagonal as a result of the disorder. The diagonal width of the peak increases with $N_{2\mathrm{LS}}$. When

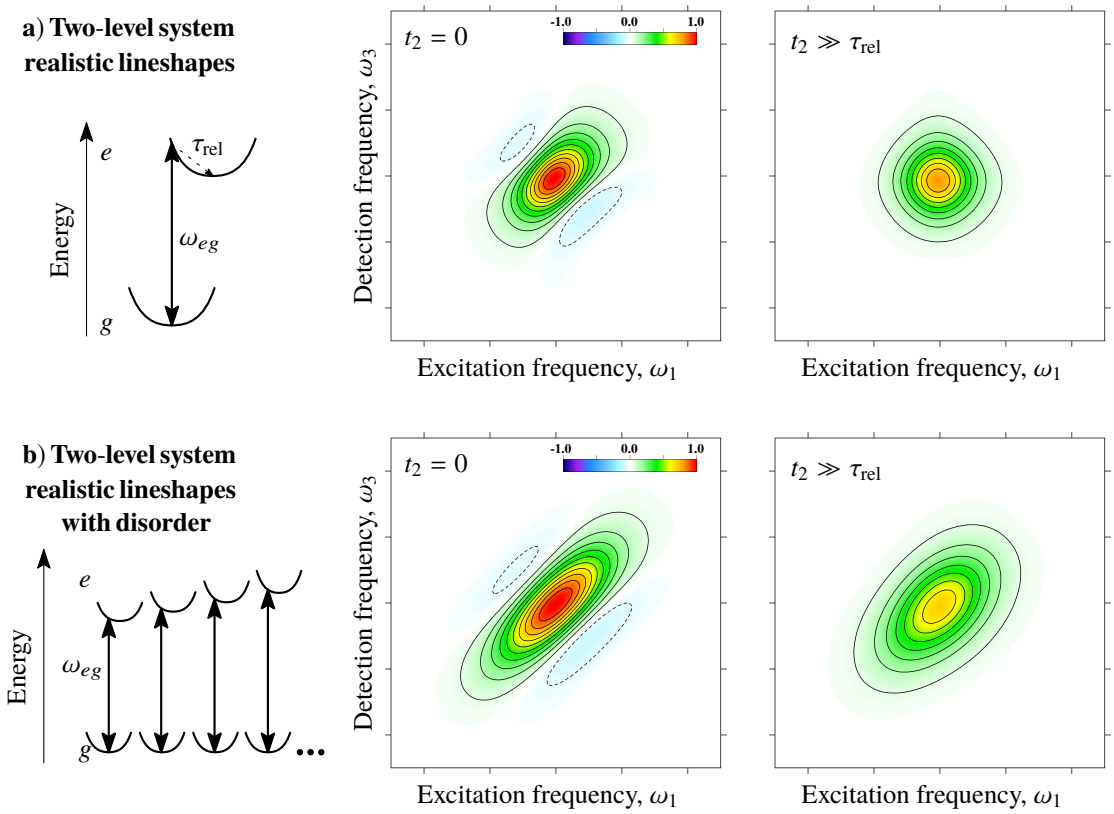

Figure 1.3: Example of the 2D spectra of a 2LS (without or with disorder) with realistic lineshapes. a) left, the energy level diagram of a realistic 2LS, illustrating the potential energy surfaces along some generalized coordinate; right, the 2D spectra of a 2LS with realistic lineshapes at zero and large waiting times. b) left, the energy level diagram of a realistic 2LS with disorder; right, the 2D spectra of a realistic 2LS with disorder at zero and large waiting times. Calculations of these 2D spectra were performed using the approach described in Section 2.5.

$N_{2LS} = \infty$, the peak shape in both the absorption and the 2D spectrum becomes fully Gaussian, and its width along the diagonal and antidiagonal corresponds to the inhomogeneous and homogeneous broadening, respectively. This can be visualized by comparing the absorption spectrum of the ensemble, given by the black line, and the single constituent absorption, given by the thinner blue line. Strictly speaking, the antidiagonal width corresponds to a convolution of a homogeneous lineshape and the inhomogeneous distribution of the transition frequencies and can be denoted as total broadening, though we will not make such distinction here. Ability to separate the homogeneous and inhomogeneous broadening is an advantage of a 2D spectroscopy technique, that is not available in linear spectroscopic measurements.

In real experiments, the lineshapes of the peaks in the 2D spectra are rarely

simple two-dimensional Gaussians, as they are determined by the interactions between the electronic and vibrational degrees of freedom. Examples of 2D spectra with realistic lineshapes is given in Fig. 1.3. First, in Fig. 1.3a realistic lineshapes of a single 2LS are shown. On the left we depict the energy level diagram. Curved lines illustrate the potential energy surfaces of the ground state g and the excited state e along some generalized coordinate. The energy surface of the excited state is shifted relative to that of the ground state. Therefore, transitions do not occur between the minima of the surfaces, and subsequent relaxation occurs (on the order of time τ_{rel}). Accordingly, 2D spectra will evolve during the waiting time t_2, as shown in the right panel of Fig. 1.3a. While at zero waiting time the 2D peak is not symmetric, elongated along the diagonal, and accompanied by negative lobes on its sides, after a waiting time longer than relaxation ($t_2 \gg \tau_{\mathrm{rel}}$), its shape becomes almost round. This is related to the loss of memory of excitation – no matter at what frequency the system was excited, it emits from a relaxed state (corresponding to a thermal distribution).

When disorder is added to such a realistic 2LS, at zero time the peak in the 2D spectrum is more elongated diagonally than in Fig. 1.3a, and similarly as in Fig. 1.2c (see Fig. 1.3b, right panel). With time, the antidiagonal width of the peak increases, but the peak does not become round. Thus, contrasting the 2D spectra at $t_2 \gg \tau_{\mathrm{rel}}$ in both Fig. 1.3a and b, we see that a homogeneous system exhibits round peaks in the 2D spectra at longer times, while the peaks of an inhomogeneous system remain elongated along the diagonal. This qualitative difference is useful for the analysis of experimental data.

1.2.1.2 Two coupled two-level systems – a dimer

Let us now consider a more complicated situation, with a dimer consisting of two resonantly coupled 2LSs. The 2D spectrum of a dimer, along with the illustrating diagrams, is shown in Fig. 1.4. The transition dipole moments (left of the figure) are assumed to be at some angle, and, due to the close proximity of the monomers, resonance interaction between the excited states is not negligible. In the energy diagram (central part of the figure), both molecules have their own ground states, the corresponding excited states are denoted by a and b, and the transition frequency ω_{ag} is assumed to be smaller than that of the other monomer, ω_{bg}. Due to the resonance interaction, the molecular excitation states are no longer the eigenstates of the dimer, which are the delocalized excitations called the excitonic states or excitons [25]. The energy gap between the excitonic states e_1 and e_2 is larger than the energy gap between the molecular states

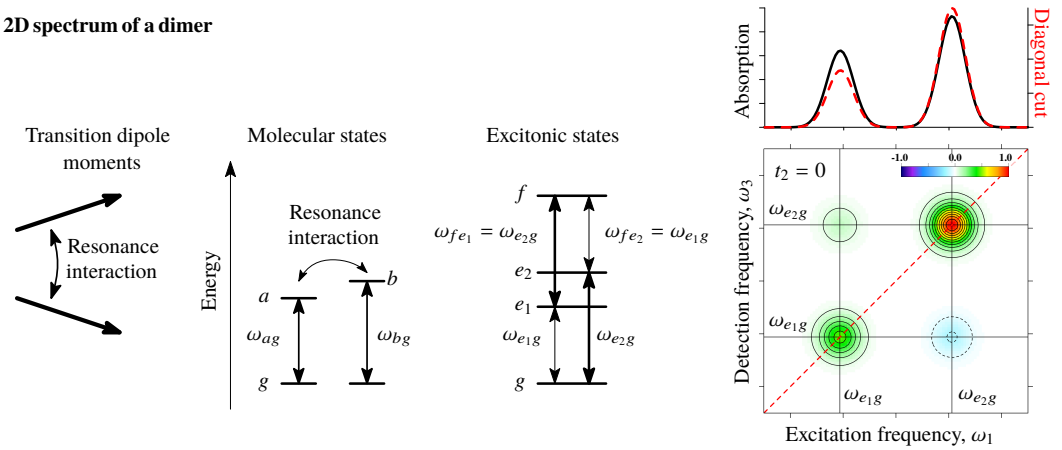

Figure 1.4: Example of a 2D spectrum of a dimer – two coupled 2LSs. Left, a depiction of the orientation of the transition dipole moments; center, the energy level diagrams depicting both the molecular and the excitonic states; right, the 2D spectrum of such a system at zero waiting time; top, the corresponding absorption spectrum (solid black line) and the diagonal cut of the 2D spectrum (red dashed line).

a and b, because of the energy level repulsion. There is also a double-excited state f, which corresponds to the situation when both excitonic states are excited at the same time. Transitions $e_2 \leftrightarrow g$ and $f \leftrightarrow e_1$ are somewhat stronger in this example, thus are drawn with thicker lines.

The 2D spectrum of such a system (Fig. 1.4, right panel) at zero waiting time contains four peaks at excitation and detection frequencies matching the transition frequencies of the excitonic states ω_{e_1g} and ω_{e_2g}. In addition to the diagonal peaks, the cross-peaks arising from the coupling between the monomers can also be observed. As these vanish when the interaction between the molecular states goes to zero, their presence at very early time in the 2D spectra implies interactions between the constituents of the observed system. The lower cross-peak is negative, which indicates that the ESA signal is stronger than the corresponding ESE and GSB signals. Note, that this depends on the spatial arrangement of the constituent transition dipole moments. Above the 2D spectrum the corresponding absorption spectrum (solid black line) and the diagonal cut of the 2D spectrum (dashed red line) are shown. For a system bigger than a single 2LS, the diagonal cut can no longer be scaled to perfectly match the absorption spectrum, as the peak amplitude is proportional to the square of the transition dipole moment in the absorption spectrum, and to the fourth power of the transition dipole moment in the 2D spectrum.

The evolution of this 2D spectrum is shown in Fig. 1.5. In the diagram of

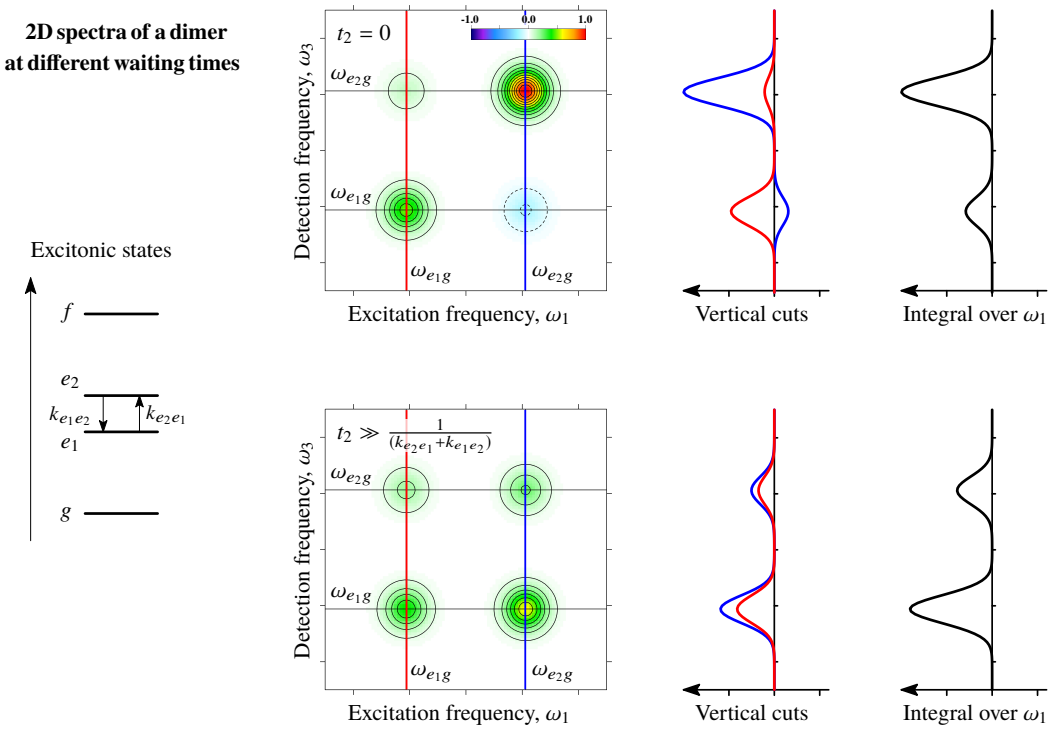

Figure 1.5: Example of the 2D spectra of a dimer at different waiting times t_2. Left, the energy level diagram of the excitonic states of the system, with transition rates ($k_{e_1e_2}$ and $k_{e_2e_1}$) defined between the excitonic states e_1 and e_2; top row, the 2D spectrum of a dimer at waiting time t_2 equal to zero, vertical cuts (red and blue curves) of the 2D spectrum at excitation frequencies equal to ω_{e_1g} and ω_{e_2g}, and integral over excitation frequency ω_1; bottom row, same as top row, but at waiting time $t_2 \gg 1/\left(k_{e_2e_1} + k_{e_1e_2}\right)$, that is, after the relaxation between the excitonic states is complete.

energy levels (left panel), the transition rates between the excitonic states ($k_{e_1e_2}$ and $k_{e_2e_1}$) are introduced. Their sum defines the relaxation timescale in the system. 2D spectra at time $t_2 = 0$ and at time when the energy transfer is completed, i. e. $t_2 \gg 1/\left(k_{e_2e_1} + k_{e_1e_2}\right)$, are plotted in the top and bottom rows of the figure, respectively. At long waiting time, the diagonal peak at $\omega_1 = \omega_3 = \omega_{e_2g}$ shows a considerable loss of amplitude, because the excitation energy was transferred from e_2 to e_1. The lower cross-peak, correspondingly, shows a large increase of the signal amplitude, even going from negative to positive. On the other hand, dynamics of peaks at excitation frequency ω_{e_1g} is much less pronounced. Nonetheless, the diagonal peak shows some loss of the amplitude, because of the uphill excitation transfer from the lower excitonic state to the higher one. This is possible at higher temperatures, when the thermal energy is of similar magnitude to the energy gap between the excitonic states. Correspondingly, the cross-peak shows some increase of the amplitude. Vertical cuts of the 2D

spectrum at excitation frequency ω_1 equal to ω_{e_1g} or ω_{e_2g} (denoted in the right panels of the figure by red and blue lines respectively), in principle, can be compared to the narrow-band pump–probe experiments. Relation of the 2D spectra and the pump–probe spectra will be discussed in Section 1.2.2. Red line shows larger intensity at the detection frequency $\omega_3 = \omega_{e_1g}$, while the amplitude of the cross-peak is much smaller at the initial time. The blue line shows larger intensity at $\omega_3 = \omega_{e_2g}$, while the amplitude of the cross-peak is negative. At longer times the amplitudes of the cuts become somewhat similar, with features corresponding to the lower detection frequency having larger amplitudes. The integral of the 2D spectrum over the excitation frequency ω_1 can be compared to a wide-band pump–probe spectrum. It shows a more global picture – decrease of the amplitude at higher energy and increase of the amplitude at lower energy with increasing waiting time.

1.2.2 Comparison of 2D and pump–probe spectroscopies

The decoupling of time and frequency resolution is one of the main advantages of the 2D spectroscopy versus the pump–probe spectroscopy. In this subsection, we will provide a simplified explanation for these differences. To keep the discussion simple, we will neglect the influence of the pulse overlap effects.

The resolution can be defined along three axis: excitation frequency (ω_1 or ω_{pump}), waiting time (t_2 or t_{delay}) and detection frequency (ω_3 or ω_{probe}). The influence of the laser pulses to the 2D or pump–probe spectra can expressed as:

$$\begin{aligned} \text{2D}\,(\omega_1, t_2, \omega_3) = {} & \text{2D}_{\text{ideal}}\,(\omega_1, t_2, \omega_3) \times \text{Wide band pulse}\,(\omega_1) \\ & * \text{Short pulse}\,(\text{t}_2) \times \text{Wide band pulse}\,(\omega_3); \end{aligned} \tag{1.1}$$

$$\begin{aligned} \text{PP}\,(\omega_1, t_2, \omega_3) = {} & \text{2D}_{\text{ideal}}\,(\omega_1, t_2, \omega_3) * \text{Pump pulse}\,(\omega_1) \\ & * \text{Pump pulse}\,(\text{t}_2) \times \text{Wide band (probe) pulse}\,(\omega_3). \end{aligned} \tag{1.2}$$

Here $\text{2D}_{\text{ideal}}\,(\omega_1, t_2, \omega_3)$ is the ideal 2D spectrum of the system, determined only by the system's characteristics, and the symbols $\times$ and $*$ mean multiplication and convolution, respectively. In both the 2D and pump–probe spectroscopy experiments, the detection frequency resolution is obtained by multiplying the system response with the laser pulse in the frequency domain. Since it is common that the laser pulse is wide, thus covering every relevant transition band, the detection frequency resolution can be very close to the ideal case. Of course, if the laser pulse is narrower than the spectral bandwidth of the system, some

of the spectroscopic features near or outside the edges of the laser pulse become unresolvable (see also discussion in Section 1.2.3). The main differences between the 2D and pump–probe spectroscopy lie in the waiting time and excitation frequency resolution. In the 2D spectroscopy, the excitation frequency resolution is the same as it is for the detection frequency resolution – the system response is multiplied by the laser pulse in the frequency domain. The time resolution, meanwhile, is obtained by convolving the system response with the laser pulse in the time domain. Since the laser is broad in the frequency domain, and thus short in the time domain, both excellent time and excitation frequency resolutions can be achieved. This is in a strong contrast with the pump–probe spectroscopy. There the convolution in the time domain is also employed to obtain the waiting time resolution. Yet to obtain the excitation frequency resolution, the convolution in the frequency domain must be employed with the *same* (pump) laser pulse. The key issue is that short pulses in the time domain mean wide pulses in the frequency domain and, conversely, long pulses in the time domain mean narrow pulses in the frequency domain. Thus, in the narrow band pump–probe (long pump pulse) conditions, selective spectral excitation is achieved, but at the cost of the time resolution, and wide band pump–probe (short pump pulse) experiments have good time resolution, but are not able to discern spectral features. The 2D spectroscopy, however, combines the advantages of both approaches.

To further illustrate this description, in Fig. 1.6 we show a comparison of the frequency and time resolutions in an idealistic 2D experiment, a realistic 2D experiment, and a realistic pump–probe experiment. The system under consideration is a dimer, with two excitonic states separated by 150 cm^{-1} (Fig. 1.6b), a downhill energy transfer rate of $(100\,\mathrm{fs})^{-1}$ and an uphill rate calculated from the detailed balance relation (assuming the experiment is performed at 300 K) of $(205\,\mathrm{fs})^{-1}$. These numbers represent typical values for the photosynthetic complexes [25].

In the idealistic 2D experiment, the width of the laser pulse in the time domain tends to zero (standard deviation $\sigma_t \to 0$), while the width in the frequency domain is infinite ($\sigma_\omega \to \infty$). For the realistic 2D experiment, the width of the laser pulses was fixed at $\sigma_t = 5\,\mathrm{fs}$ (or full width at half maximum (FWHM) $\approx 12\,\mathrm{fs}$), which is at the limit of what is possible with the current experimental setups [**P6**, 66, 67]. Accordingly, in the frequency domain the laser pulses have a width of $\sigma_\omega \approx 1060\,\mathrm{cm}^{-1}$ (or FWHM $\approx 2500\,\mathrm{cm}^{-1}$). Finally, for the realistic pump–probe experiment, the laser pulses controlling the excitation frequency

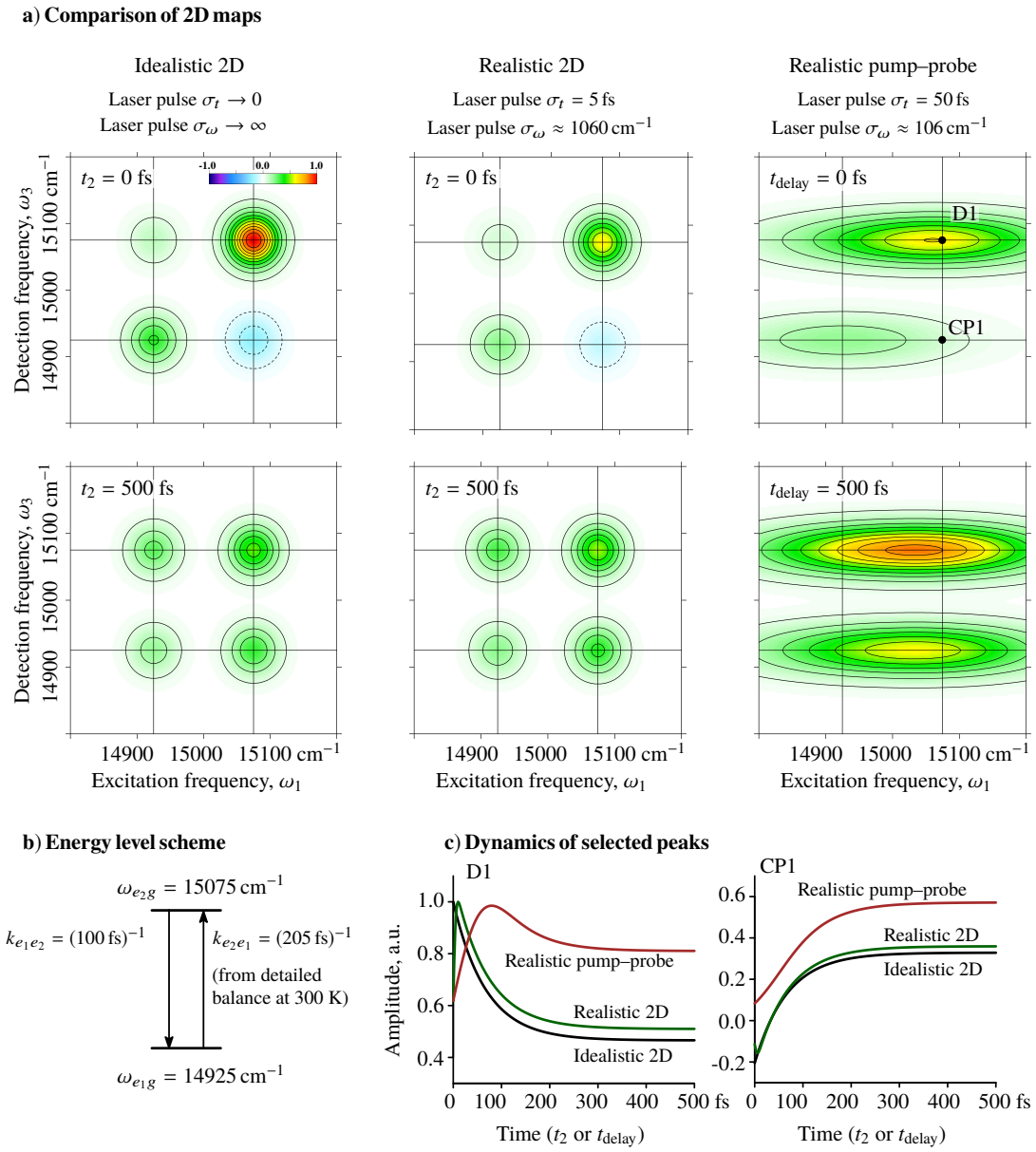

Figure 1.6: Comparison of the frequency and time resolutions provided by an idealistic 2D spectroscopy, a realistic 2D spectroscopy and a realistic pump–probe spectroscopy of a model dimer system. a) a comparison of 2D maps at two waiting times. b) the energy level scheme of the system, depicting the energy transfer rates. c) dynamics of the diagonal peak D1 and cross-peak CP1.

and time resolution were chosen with $\sigma_t = 50\,\text{fs}$ (or FWHM $\approx 120\,\text{fs}$) in the time domain, and $\sigma_\omega \approx 106\,\text{cm}^{-1}$ (or FWHM $\approx 250\,\text{cm}^{-1}$) in the frequency domain. The center frequency of the pulses was set at 15000 cm^{-1}, in the middle between the energies of the two exciton states.

Fig. 1.6a shows a comparison of the 2D maps at two different waiting times. The idealistic 2D spectra show four clearly resolvable peaks (two diagonal peaks and two cross-peaks), centered at the transition frequencies $\omega_{e_1 g}$ and $\omega_{e_2 g}$. The realistic 2D spectra are very similar at both delay times, demonstrating the excellent resolution that can be achieved in the 2D experiments. In contrast, the 2D maps showing the realistic pump–probe spectra are substantially different. Note that such maps could be constructed by stacking many pump–probe experimental data sets obtained at different excitation frequencies as discussed in Section 1.1. First, due to the loss of the excitation frequency resolution, it is not possible to discern four separate peaks – only two peaks, at the detection frequency equal to $\omega_{e_1 g}$ or $\omega_{e_2 g}$ are visible. Moreover, while the lower cross-peak should be negative, there is no negative amplitude in the pump–probe spectra. This can, for instance, prevent extraction of information about the relative orientation of the transition dipole moments. At longer delay times, the maximum of the peak corresponding to the detection frequency equal to $\omega_{e_1 g}$ shifts along the excitation frequency axis, suggesting that there should be at least two states, which are clearly resolved in 2D spectra. Interpretation of the pump–probe data thus often requires more *a priori* knowledge about the system. Finally, Fig. 1.6c depicts the dynamics of the diagonal peak D1 and the cross-peak CP1. While the curves corresponding to the realistic 2D and idealistic 2D are very similar, pump–probe data show considerable differences. For the diagonal peak D1, the slow rise of the amplitude is a result of a convolution with the laser pulse in the time domain, causing difficulties to determine the real decay time. In addition, the relative long time amplitude of the D1 peak is much larger than in the 2D case. For the cross-peak CP1, the dynamics clearly shows an offset amplitude, as discussed before, and the rise time looks slower, due to the convolution effects.

It must be noted, however, that the resolution deficiencies of the pump–probe spectroscopy become important only when the system under consideration has several close bands, and dynamics of those bands is fast. This is the case for the FCP complex discussed in Section 1.3. If the spectroscopic bands are well separated and the timescales of interest are longer, the pump–probe spectroscopy is able to provide the same answers, though some more work to account for the

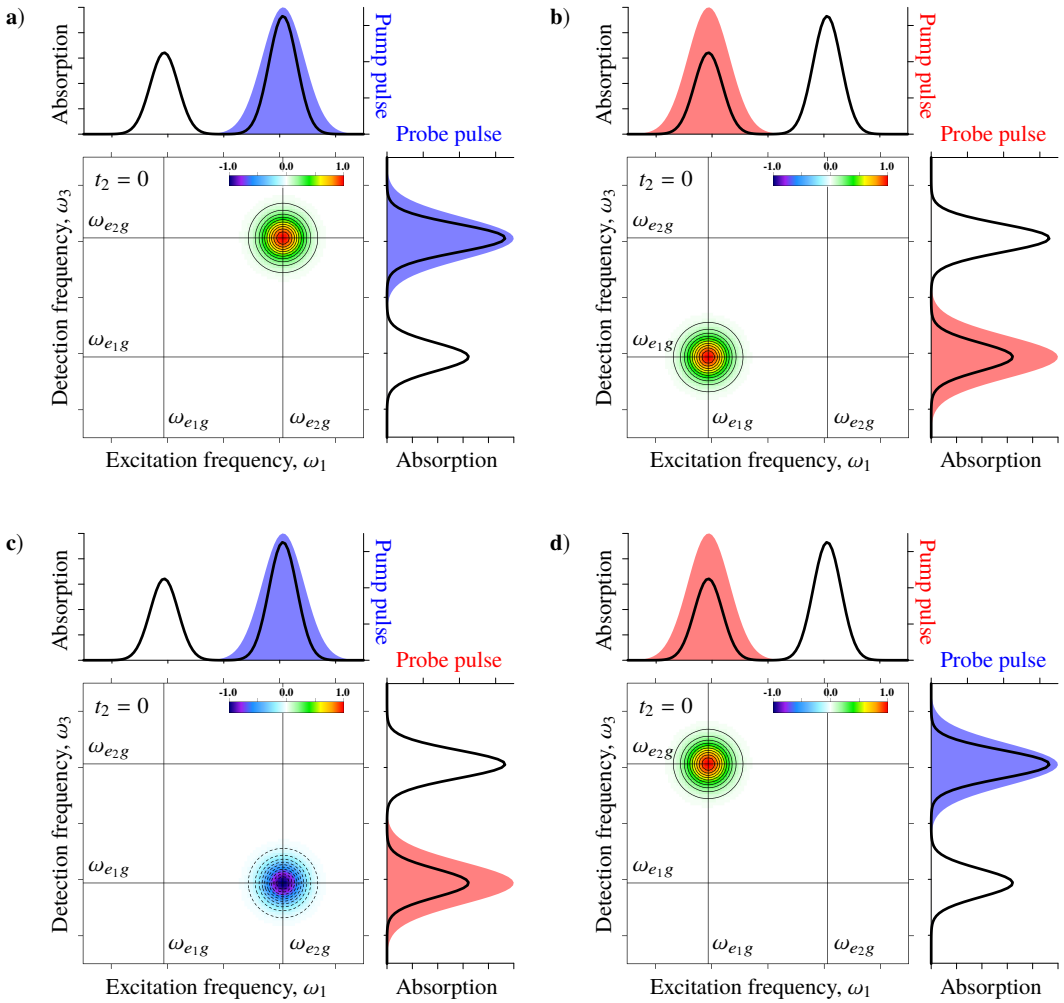

Figure 1.7: Two-color 2D spectroscopy of a dimer. In all parts center panel depicts the 2D spectrum, top panel – the absorption spectrum (solid black line) and the pump pulse (shaded curve), right panel – the absorption spectrum (solid black line) and the probe (and LO) pulse (shaded curve). a) blue–blue case (blue excitation, blue detection). b) red–red case. c) blue–red case. d) red–blue case.

influence of the pulses might be required.

1.2.3 Two-color 2D spectroscopy

This description of the 2D spectroscopy would be incomplete without mentioning the two-color 2D spectroscopy. Conceptually, it is similar to the two-color pump–probe spectroscopy – excitation at one frequency (or color) and detection at another. Nonetheless, due to the experimental difficulties, two-color 2D spectroscopy is relatively rarely employed. Its application to the FCP complex is given in Section 1.3.2. In Fig. 1.7 we illustrate the fundamental concepts of this approach. As the resolution of the 2D spectroscopy depends on the width

and center frequency of the laser pulses, employing narrower pulses, and centering them to different frequencies, leads to the selective extraction of some parts of the 2D spectra along the diagonal. Fig. 1.7a and b show that tuning pump pulses and probe (and LO) pulse to different bands of the absorption spectrum of a dimer leads to the extraction of the lower or higher energy peaks. Extracting the cross-peaks requires the tuning of the pump and probe pulses to different frequencies (as illustrated in Fig. 1.7c and Fig. 1.7d). The main use of the two-color 2D spectroscopy is when the laser pulses are not wide enough to cover all the relevant spectral bands of the system. Then by pumping and probing at different frequencies, information can be obtained from all the relevant parts of the full 2D spectrum.

1.2.4 Analysis of 2D spectra

In this section, we will discuss different ways to present and analyze data of a 2D spectroscopy experiment. This is illustrated in Fig. 1.8. First, let us note that the overall dataset comprises a cube of 2D spectroscopy data (see Fig. 1.8a), with one dimension being the excitation frequency ω_1, another – the detection frequency ω_3, and the third – the waiting time t_2. The 2D data is most often analyzed by taking cuts of this cube along some chosen dimensions.

To demonstrate this we take a model system depicted in Fig. 1.8b. We have two excited eigenstates, e_1 and e_2, with possible transfer between them. Additionally, the higher energy state, e_2, also decays to the ground state. For this system, in Fig. 1.8c we plot the 2D spectra at several waiting times. This corresponds to cuts of the full cube of the 2D data at specific t_2 values. As a first step of analysis, the 2D map corresponding to the earliest waiting time should be considered. This reveals the pattern and the position of the peaks and the sign of the cross-peaks. It would also show the homogenous and inhomogenous broadenings, though in the example here we choose idealized lineshapes for simplicity. Then we can compare the 2D maps at different waiting times and note the differences between them. Here we can immediately notice a decrease of the amplitude of the diagonal peaks, and an increase and a later decrease of the amplitude of the cross-peaks. The lower cross-peak even changes the sign from negative at initial time to positive at later times.

Choosing the most interesting spectral features, we are in position to analyze their temporal dynamics more closely. First, in Fig. 1.8d we present a 2D plot corresponding to the cut of the full cube of 2D data along the specific value of the excitation frequency, $\omega_1 = 15075\,\mathrm{cm}^{-1}$. Thus, the horizontal axis here rep-

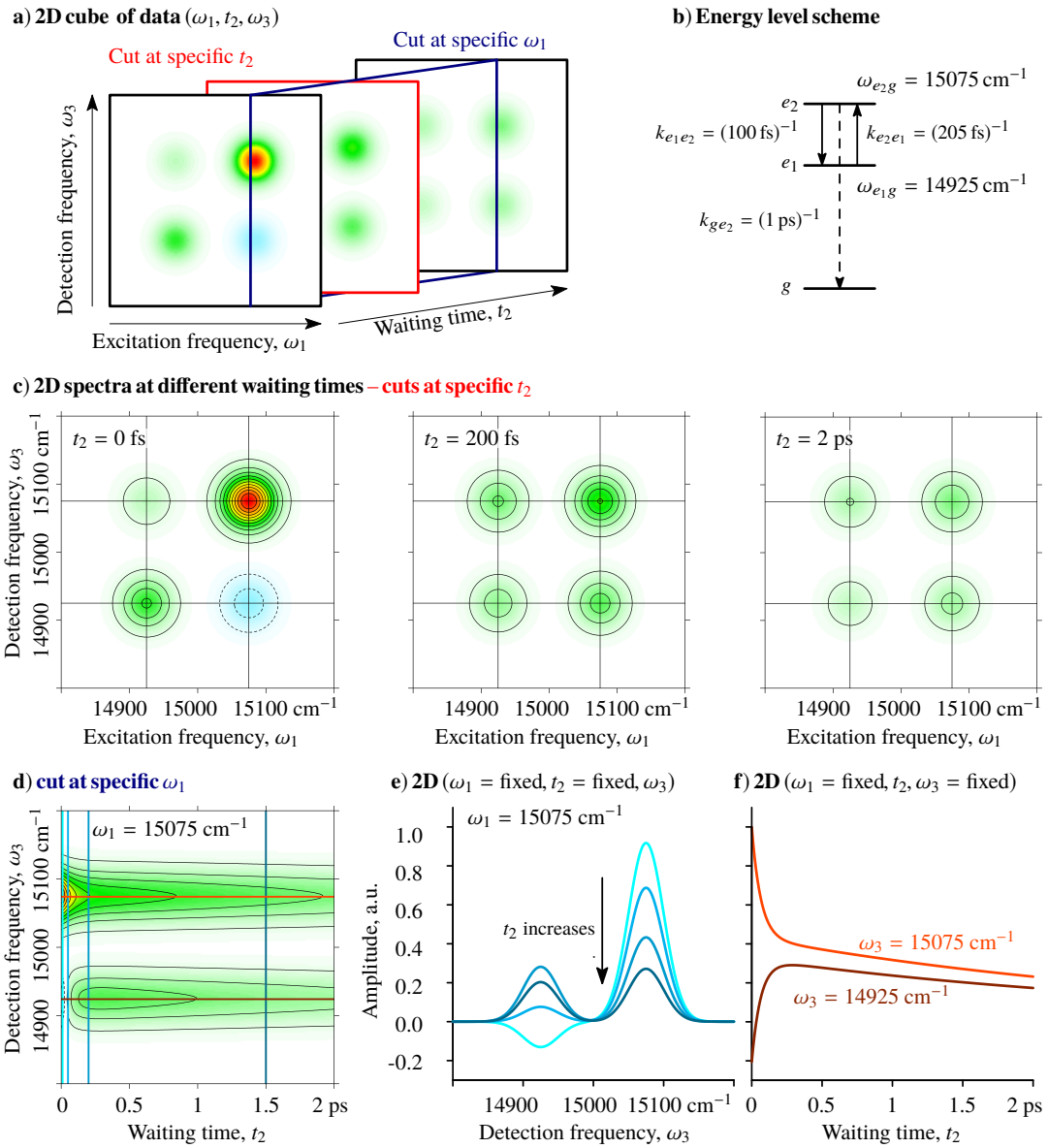

Figure 1.8: Different ways of analyzing the 2D spectroscopy data. a) a graphical representation of the combined three dimensional (two frequency dimensions and one time dimension) data available from the 2D experiment, with colors highlighting specific cuts. b) the energy level scheme of the system, depicting the energy transfer rates. Note that the higher energy excited state can decay to the ground state. c) the 2D spectra at different waiting times, corresponding to the cuts of the full data cube at a specific t_2. d) the cut of 2D data cube at the specific excitation frequency $\omega_1 = 14975\,\mathrm{cm}^{-1}$, with horizontal and vertical axis representing waiting time (t_2) and detection frequency (ω_3) ,respectively. e) the cuts of the full cube of 2D data cube at the specific excitation frequency $\omega_1 = 14975\,\mathrm{cm}^{-1}$ at several waiting time (t_2) values. f) the cuts of the full cube of the 2D data at specific excitation frequency and detection frequency values, representing the kinetics of the chosen spectral features. The color of the lines in parts e) and f) corresponds to the cuts of the 2D map in d).

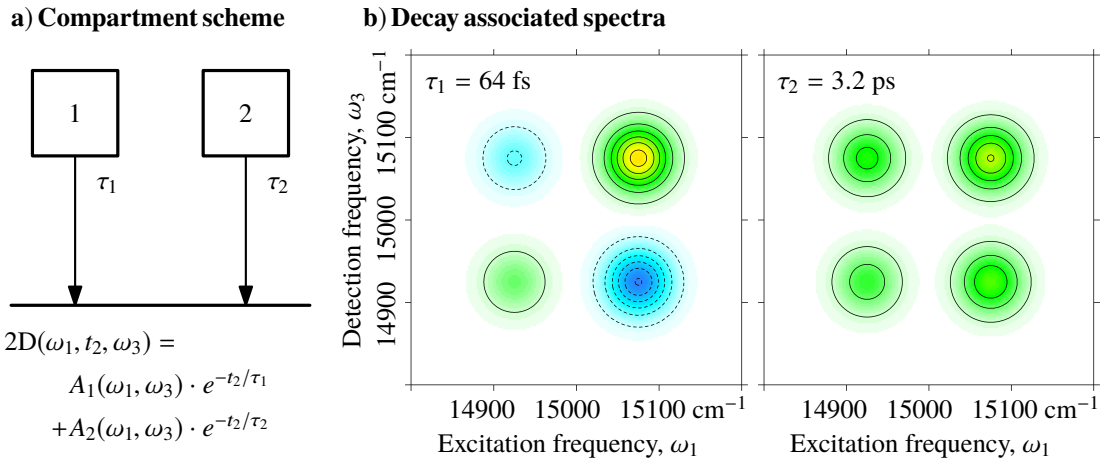

Figure 1.9: Demonstration of DAS analysis of the 2D spectra (data is the same as in Fig. 1.8). a) chosen compartment scheme. b) obtained DAS.

resents the waiting time t_2 instead of the excitation frequency. In this way, we see all the time evolution of the upper diagonal peak and the lower cross-peak. While this type of representation gives nice visualization, for more quantitative analysis it is more convenient to compare the cuts at different t_2 values, as is shown in Fig. 1.8e. Here the colors of the lines correspond to colors of vertical lines in Fig. 1.8d. It depicts the cuts of the full data cube both at fixed excitation frequency ω_1 and fixed waiting time t_2. This type of plot allows to quantitatively compare the amplitudes of the spectral features at specific times. Another way to obtain the temporal dynamics of the selected spectral features is to simply plot their kinetics. This is demonstrated in Fig. 1.8f for the upper diagonal peak (orange line) and the lower cross-peak (brown line), with colors matching the horizontal lines in Fig. 1.8d. This representation corresponds to cuts of the full data cube at fixed excitation and detection frequencies. In this case, we can notice that there are two distinct timescales in the system. Fast timescale corresponds to decay of amplitude of the diagonal peak with the corresponding increase of amplitude of the cross-peak, reflecting energy transfer. A slower timescale corresponds to the decay of both peaks, corresponding to the relaxation of excitation to the ground state.

We must also mention the representation of the 2D data in terms of the decay associated spectra (DAS). Though performed on the pump–probe or time-resolved fluorescence datasets for decades [68], only recently this approach was applied to the 2D spectroscopy results, with different implementations [69, 70]. The main idea is to decompose the full 2D dataset into several distinct 2D spectra, each evolving with distinct timescale. The obtained spectra then correspond

to some compartment in a chosen kinetic model (parallel, sequential, etc.). A more complicated but sometimes revealing analysis is to assume different kinetics for each point of the 2D spectra [14, **P5**], see this type of analysis in Section 1.3.2.

From the dataset of Fig. 1.8 one can obtain the DAS shown in Fig. 1.9. Here we have chosen a simple parallel two compartment scheme, demonstrated in Fig. 1.9a. The obtained DAS with their timescales are given in Fig. 1.9b. In this case, the two DAS can be easily interpreted, with one corresponding to the energy transfer between the excited states with a fast timescale while the other corresponding to the overall relaxation to the ground state. Nonetheless, extreme caution must be applied when interpreting the DAS for larger systems (larger photosynthetic complexes, their aggregates or even whole photosystems), as then the obtained DAS might not correspond to any physical processes, being instead a mathematical representation of a complex non-exponential dynamics arising from multiple constituents, with possibly fluctuating connectivity or spatial positions.

1.3 2D spectroscopy of FCP

In order to collect the solar photons, eukaryotic photosynthetic organisms generally use a complex membrane light-harvesting system, based on the assembly of several light-harvesting proteins belonging to the LHC superfamily [1]. Diatoms are unicellular chromophyte algae inhabiting marine environment. They are the major players in photosynthesis, accounting for nearly a quarter of the global primary production [71–73]. The light-harvesting system of diatoms (and brown algae) is based on the FCPs [74]. Their pigment composition reflects the adaptation to the green–blue light of marine environment. First, Fx molecules are found in greater amounts relative to the carotenoids in the major light-harvesting complex of higher plants (LHCII), and their absorption extends into the blue–green range. Also, Chl *c* displays an intense Soret electronic transition in the blue, due to the higher symmetry of the molecule, and reinforces the ability of FCP to harvest blue photons [75].

As an atomic structure for FCP is still lacking, the crystal structure of the LHCII [36] can be used as a template for pigment organization in FCP, as these two antennae complexes share similar primary sequences [76, 77]. Nonetheless, it cannot be applied directly, as the pigment stoichiometry in FCP strongly differs from that of LHCII. In a recent resonance Raman study, it was shown

that no less than 5 or 6 distinct Fxs per Chl *c*, as well as two distinct Chl *c* should be present in FCPs from the *Cyclotella meneghiniana* diatom [78]. This implies that FCP polypeptides should bind no less than 18 pigments, that is 8 Chl *a*, 8 Fx, 2 Chl *c* – this ratio, though not the exact numbers, was established before [40]. LHCII, on the other hand, contains 8 Chl *a*, 6 Chl *b* and 4 xanthophyll molecules [36]. Sequence analysis suggests that a few helices of LHCII are conserved in FCP, as well as seven of the Chl binding sites [78]. Nevertheless, even if FCP and LHCII share common structural features, the cascades of the excitation energy transfer and the mechanisms involved are expected differ significantly.

The initial events in FCP from diatom *Cyclotella meninghiniana* were analyzed using the pump–probe spectroscopy [40, 41]. This was also done for FCP from the brown algae *Cladosiphon okamuranus* Tokida [43]. Nonetheless, in such a complex system, no less than 8 compartments were necessary to model the data [40]. The main conclusions of that study was that a sizable fraction of excitation was transferred very rapidly from the second, optically allowed excited state of Fx (S_2) to Chl *a*, and that the transfer from Chl *c* to Chl *a* was ultrafast.

Therefore, such a pigment-protein complex, with a particularly complicated network of pigments and several ultrafast excitation pathways, is an ideal system to illustrate the power of the 2D electronic spectroscopy.

1.3.1 Ultrafast energy transfer from Chl *c* to Chl *a*

Previously, the question of Chl *c* to Chl *a* energy transfer in FCP was studied by pump–probe spectroscopy. [40, 42]. Fast transfer was inferred, yet its exact timescale was not established. The role that Chl *c* plays in the energy transfer pathways of FCP is therefore still an open question [43].

To investigate the Chl *c*→Chl *a* energy transfer, we performed 2D spectroscopy experiments at room temperature[1]. More details about the sample preparation and the experimental conditions are given in Ref. [**P3**].

First, in Fig. 1.10 we show the absorption spectrum of FCP at room temperature, together with those of Chl *a* and Chl *c*. While FCP absorbs more strongly in the blue spectral region, in this subsection we consider the lower energy bands, which are highlighted. The Q_y band due to Chl *a* is at $\sim$ 14900 cm^{-1}, while that of Chl *c* is at $\sim$ 15600 cm^{-1}. As can bee seen, these bands are well-covered

[1] Experiments were performed by Egidijus Songaila and Ramūnas Augulis at the lab of Donatas Zigmantas, Lund University, Sweden.

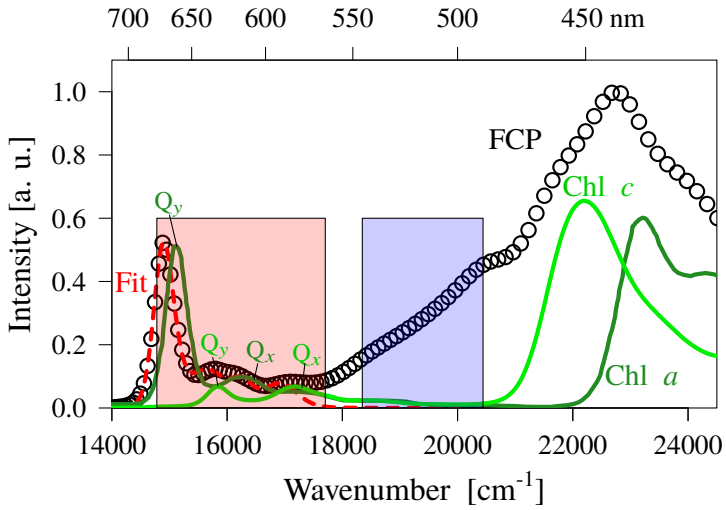

Figure 1.10: Experimental absorption spectrum of FCP at room temperature (open circles). Also, the absorption spectra of isolated Chl *a* [43] (dark green line) and Chl c_2 in acetone [**P3**] (green line), with their corresponding $Q_{y/x}$ bands marked. Soret transitions are in the blue spectral region ($\gtrsim 21000\,\mathrm{cm}^{-1}$). Red dashed line denotes the fit of FCP Chl $Q_{y/x}$ absorption bands (see text for details). Red shaded area illustrates the laser pulse used in the single color 2D experiments and the probe pulse in the two-color 2D experiments. Blue shaded area illustrates the pump pulse used in the two-color 2D experiments. For the exact shapes of the pulses, see Refs. [**P3**, **P6**].

with the laser pulse used in our experiments (see red shaded area). No clear excitonic structure is visible in the spectrum, suggesting relatively small couplings between the pigments.

In Fig. 1.11 we show the experimental and simulated (see below) 2D spectra of FCP. The dominant peak at the initial waiting time $t_2 = 20$ fs is the Chl *a* Q_y band at 14900 cm^{-1} (670 nm). Note that the spectra at earlier waiting times are not shown due to the presence of the pulse overlap effects. There also is another diagonal peak, marked by a red circle, at 15600 cm^{-1} (640 nm), which is due to the transitions to the Q_y band of Chl *c*. Also present is the corresponding cross-peak below the diagonal (marked by a blue circle), though it is relatively weak and is seen only as an elongation of the main diagonal peak along the ω_1 axis. The presence of such cross-peak at very early times suggests that Chl *a* and Chl *c* are excitonically coupled. Discussion about other features in the 2D spectra is given in Ref. [**P3**].

We turn to the time evolution of the 2D spectra. We focus onto the diagonal element of Chl *c* and the corresponding cross-peak with the Chl *a* Q_y band. It can be seen that the diagonal peak disappears very quickly, as it is not visible in

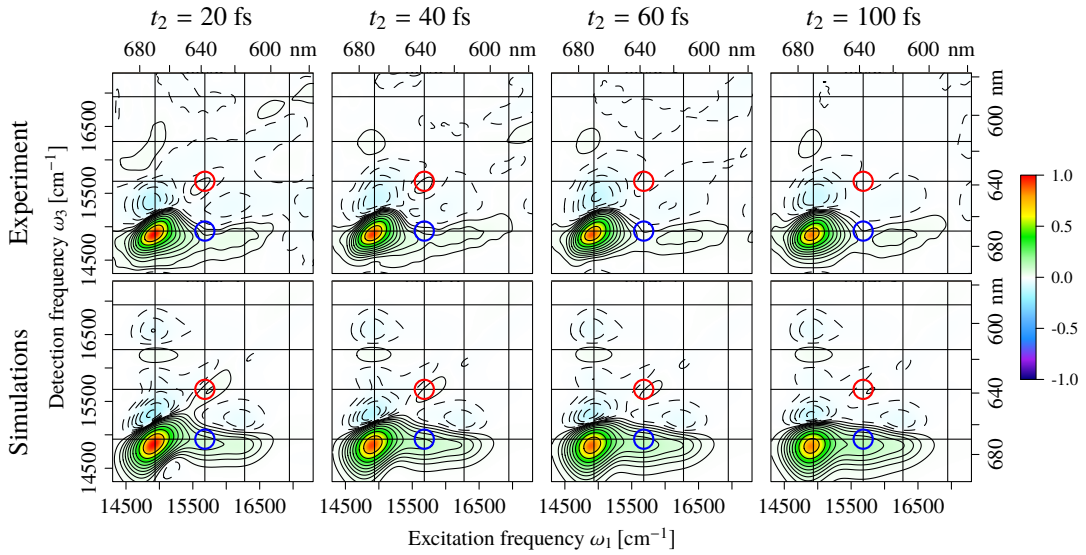

Figure 1.11: Experimental and simulated 2D spectra of the FCP complex at room temperature. Real part of the total spectra is given. Both the experimental and simulated spectra are scaled to the values of their respective maxima at t_2 = 20 fs. Horizontal and vertical lines correspond to the energies of single excitation bands (in order of decreasing energy: Chl *a* Q_y, Chl *c* Q_y, Chl *a* Q_x, Chl *c* Q_x) determined from the fitting procedure. In this figure the contours are plotted in the ArcSinh scale to highlight weak features. Red and blue circles mark the Chl *c* Q_y diagonal peak and Chl *c* Q_y–Chl *a* Q_y cross-peak, respectively.

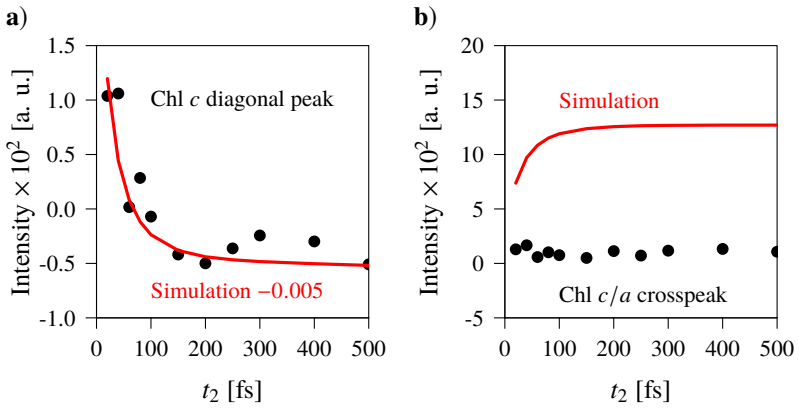

Figure 1.12: Time evolution of a) the Chl *c* Q_y diagonal peak and b) the Chl *c* Q_y–Chl *a* Q_y cross-peak, marked by the red and blue circles in Fig. 1.11, respectively. Black points are experimental data, while red lines denote simulations (see text for details).

the $t_2 = 60$ fs spectrum. It shows a clear exponential decay with the timescale of 60 fs (see Fig. 1.12a for the plot of kinetics) and this can be interpreted as a signature of energy transfer from Chl *c* Q_y to Chl *a* Q_y. Even though no fast rising component is visible in the cross-peak evolution (Fig. 1.12b), this might be related to the decay of the Chl *a* Q_y diagonal peak [**P3**].

To investigate the possibility of such fast energy transfer in FCP, we have performed simulations of the 2D spectra of the FCP complex. Preferably, they would be accomplished using a microscopic model (like described in Chapter 2). Unfortunately, there is still no structure of the FCP complex available. This prevents us from employing explicit microscopic exciton model as it requires the knowledge about the spatial arrangement of the constituent molecules. To circumvent this difficulty, here we present the results based on an effective model of the FCP complex (similar to a four state model in Ref. [79]). The main idea is to describe the main features visible in the 2D spectra with a minimum number of parameters. Below we provide a brief description for our model together with its relevant parameters. At this point a more theory inclined reader might first read Chapter 2, especially Section 2.1, where the relevant Hamiltonian is discussed, and Section 2.5, where the theory behind 2D spectra simulations is presented with more detail. Nonetheless, the model presented here is based on both a simplified Hamiltonian and a simplified theory, thus exact expressions of Chapter 2 are not directly applicable.

In the absorption spectra of the FCP complex (Fig. 1.10), we can distinguish four bands corresponding to the Q_y and Q_x transitions of Chl *a* and Chl *c*. To model only the absorption, we could treat each band as arising from the transitions in a 2LS. This type of formulation, however, would fail to explain the negative ESA features in the 2D spectra. Thus, we model each band as an anharmonic oscillator. This effectively take into account two things. First, multiple excitations of the same band become possible, which is necessary since each oscillator represents a band of states and not a single microscopic state. Second, anharmonicity accounts for the fact that there could be transitions between the $Q_{y/x}$ bands to the higher energy excited states of the same Chl molecule. The system Hamiltonian then is defined as:

$$\hat{H}_{\mathrm{S}} = \sum_{e=1}^{4} \varepsilon_e \hat{a}_e^{\dagger} \hat{a}_e + \frac{1}{2} \sum_{e,e'=1}^{4} \Delta_{ee'} a_e^{\dagger} \hat{a}_{e'}^{\dagger} \hat{a}_{e'} \hat{a}_e. \tag{1.3}$$

Here ε_e is the energy of the e-th band (exciton), $\Delta_{ee'}$ is the anharmonicity matrix, representing the binding energies of the excitons, that describe the energy shifts

arising from the presence of other excitations. These parameters will define the positions of the peaks in the absorption and 2D spectra. $\hat{a}_e^\dagger$ and $\hat{a}_e$ are the bosonic creation and annihilation operators of the e-th exciton. Thus, we have 4 single exciton states and 10 double exciton states, with 4 being overtone states and 6 being combination states. Note that the Hamiltonian presented in Section 2.1 does not include the anharmonic effects.

The bath comprise vibrational degrees of freedom of both the molecules themselves and their environment. We model it as an infinite set of harmonic oscillators linearly coupled to the exciton subsystem (similar as described by Eqs. 2.8 and 2.10). The bath is described by the spectral density. We assume that the energy fluctuations of different excitonic oscillators are uncorrelated. This type of treatment prevents us from modeling any purely coherent contributions to the 2D spectra. In this effective model, the spectral density parameters will define the lineshapes of the peaks in both the absorption and 2D spectra. The shape of the spectral density of molecular complexes is a subject of an active debate [47, 80]. In our effective model, the exact shape is not important, as we only are interested in an adequate reproduction of the spectral lineshapes. For this model we choose Debye spectral density [30], which provides an exponentially decaying bath correlation function and due to its simplicity was employed in many theoretical works [44, 81–85]. Here we use a composite spectral density consisting of two terms that describe fast and slow bath modes, respectively:

$$C_e''(\omega) = \frac{2\lambda_e^{\mathrm{F}}\gamma_{\mathrm{F}}\omega}{\omega^2 + \gamma_{\mathrm{F}}^2} + \frac{2\lambda_e^{\mathrm{S}}\gamma_{\mathrm{S}}\omega}{\omega^2 + \gamma_{\mathrm{S}}^2}. \tag{1.4}$$

The reorganization energy $\lambda_e^{\mathrm{F(S)}}$ describes the coupling strength of the e-th exciton band with the fast (slow) bath modes and $\gamma_{\mathrm{F(S)}}^{-1}$ is the timescale of bath relaxation. The fast bath modes are responsible for Lorentzian spectral shapes (homogeneous broadening) and the slow bath modes induce Gaussian spectral shapes (inhomogeneous broadening). Inclusion of the slow mode thus allows us to represent the static disorder in a computationally convenient way. We choose values $\gamma_{\mathrm{F}}^{-1} = 50\,\mathrm{fs}$ and $\gamma_{\mathrm{S}}^{-1} = 10\,\mathrm{ps}$, which are typical for the photosynthetic pigment–protein complexes [25].

To describe optical experiments, the system has to be coupled to the classical electromagnetic field $\vec{E}(t)$. We assume the dipolar system–field interaction Hamiltonian:

$$\hat{H}_{\mathrm{SF}} = -\sum_{e=1}^{4}\left(\vec{\mu}_e\hat{a}_e^\dagger + \frac{1}{\sqrt{2}}\vec{\mu}_e^{(2)}\hat{a}_e^\dagger\hat{a}_e^\dagger\hat{a}_e + \mathrm{H.c.}\right)\cdot\vec{E}(t)\,. \tag{1.5}$$

Here $\vec{\mu}_e$ is the transition dipole moment vector of the eth exciton state and $\vec{\mu}_e^{(2)}$ is its anharmonic correction corresponding to the transitions from the single exciton state to the overtone state. For simplicity, we assume that all the transition dipole moment vectors are parallel. Even though in the real FCP complex the pigments are not expected to be perfectly oriented, this assumption reduces the number of free parameters, which is very important in an effective model. The electric field pulses are assumed to be δ-shaped. This means that the calculated 2D signal is directly proportional to the relevant third order response function, as discussed in Section 2.5.

Both the linear and 2D spectra are calculated using the response function formalism employing the lineshape functions [86, 87]. We used the expressions given in Ref. [79]. Compared to the theory presented in Chapter 2, those expressions are simpler, neglecting both the ctR theory terms and the microscopic population transfer rates. Nonetheless, for effective simulations of the 2D spectra of the FCP complex these simplifications are adequate. In our model we have the following free parameters to describe the experimental data: the exciton energies ε_e, the anharmonicity matrix $\Delta_{ee'}$, the reorganization energies $\lambda_e^{\mathrm{F(S)}}$, the transition dipole moments $\vec{\mu}_e$ and their corrections $\vec{\mu}_e^{(2)}$. The values of these parameters were obtained by fitting the absorption and 2D spectra.

From the fit of linear absorption spectrum we can determine all the parameters of the single exciton manifold. We used the Markov Chain Monte Carlo fitting procedure [88] and optimized the exciton band energies ε_e (responsible for peak positions), their transition dipole moments $\vec{\mu}_e$ (responsible for peak intensities), and the couplings with the bath $\lambda_e^{\mathrm{F(S)}}$ (responsible for homogeneous and inhomogeneous broadenings). The fitted model parameters are given in Table 1.1, whereas the simulated room temperature absorption spectrum is shown in Fig. 1.10 by the red dashed line.

In order to simulate the 2D spectra, we also need the parameters of the double exciton states. Their energies are $\varepsilon_e + \varepsilon_{e'} + \Delta_{ee'}$. Transitions from the single-excited states to the combination exciton states are fully described by $\vec{\mu}_e$, while transitions to the overtone states are described by $\vec{\mu}_{e,ee} = \sqrt{2}\vec{\mu}_e + \vec{\mu}_e^{(2)}$. Because the fitting of the full 2D maps would be very expensive computationally, we have opted instead to fit the cuts of the $t_2 = 20\,\mathrm{fs}$ 2D spectrum at $\omega_1 = \varepsilon_e$ along the ω_3 axis. In this way we obtained the values of $\Delta_{ee'}$ and $\vec{\mu}_e^{(2)}$. The transition dipole corrections are provided in Table 1.1, while the non-zero anharmonicity matrix values are $\Delta_{11} = 510\,\mathrm{cm}^{-1}$, $\Delta_{21} = 150\,\mathrm{cm}^{-1}$, $\Delta_{22} = 270\,\mathrm{cm}^{-1}$, $\Delta_{31} = 235\,\mathrm{cm}^{-1}$ and $\Delta_{32} = 150\,\mathrm{cm}^{-1}$.

Table 1.1: Single exciton band parameters of the effective FCP model determined by the fit of the linear absorption spectrum and the transition dipole corrections obtained from the fit of the 2D spectra. The single exciton bands $e = \{1, 2, 3, 4\}$ correspond to the Chl *a* Q_y, Chl *c* Q_y, Chl *a* Q_x and Chl *c* Q_x transitions, respectively.

Parameter	Single exciton band			
	1	2	3	4
ε_e $\left[\mathrm{cm}^{-1}\right]$	14935	15680	16275	16945
$\vec{\mu}_{e,x}$ [a. u.]	1	0.57	0.38	0.45
λ_e^{F} $\left[\mathrm{cm}^{-1}\right]$	100	55	60	115
λ_e^{S} $\left[\mathrm{cm}^{-1}\right]$	5	155	50	105
$\vec{\mu}_{e,x}^{(2)}$ [a. u.]	−0.72	−0.13	0	0

Energy transport between the different exciton bands is described by the transfer rates $K_{e' \leftarrow e}$. In a microscopic model these would be calculated from the model parameters (e. g. using Eqs. 2.49 or 2.50 from Chapter 2). In the effective model, the rates cannot be calculated, because of assumed totally independent energy fluctuations. Thus they have to be specified. As the diagonal peak of exciton $e = 2$ (Chl *c* Q_y band) exhibits a single-exponential decay, we set $K_{1\leftarrow 2}^{-1} = 60\,\mathrm{fs}$. The corresponding upward excitation is then calculated from the detailed balance relation [86] and is found to be $K_{2\leftarrow 1}^{-1} = 2000\,\mathrm{fs}$. As no other transfer processes are visible in the experimental 2D spectra [**P3**], no other transport rates were used in the simulations.

We obtain good agreement between our simulated 2D spectra and the experimental results (Fig. 1.11). The shape of the main diagonal peak at initial waiting time $t_2 = 20$ fs together with its qualitative evolution are well reproduced. The negative ESA feature above the diagonal peak is obtained by including a large anharmonic shift of the Q_y overtone state of Chl *a*. Simulated spectra also match the diagonal peak corresponding to the Q_y transition of Chl *c* and the elongated cross-peak below the diagonal.

As our goal is to find whether the simulations can support the conclusion on the ultrafast energy transfer from Chl *c*, here we discuss the evolution of the peaks related to the Q_y band of Chl *c*. Simulated evolutions of the relevant diagonal and off-diagonal peaks are presented in Fig. 1.12. The diagonal peak dynamics fits the experiment very well, though subtraction of a constant is needed. Therefore, our calculations indicate that experimentally observed diagonal peak kinetics can be explained by the $K_{1\leftarrow 2}^{-1} = 60\,\mathrm{fs}$ excitation energy transfer rate. Nonetheless, it has to be noted that the simulated curve for the cross-peak does

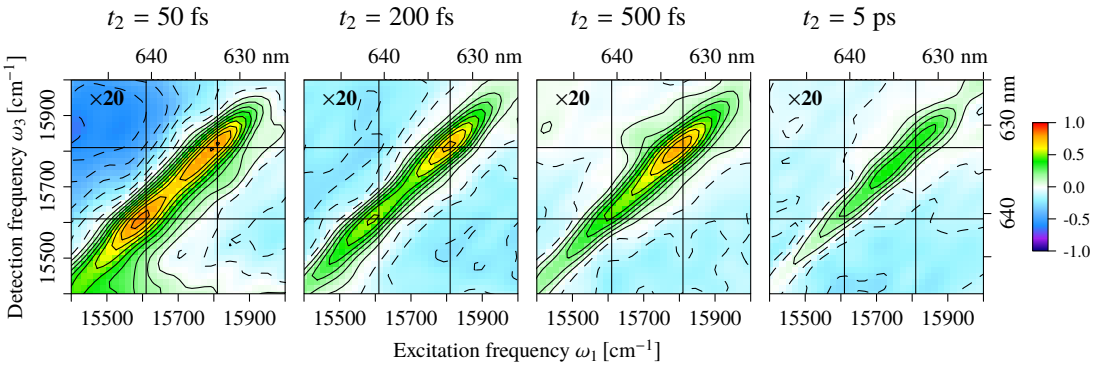

Figure 1.13: Experimental 2D spectra of the FCP complex at 77 K. Real part of the total spectra is given. Only the Chl *c* region is depicted. For the full 2D spectra and more details about the experimental conditions see Ref. [**P6**]. Vertical and horizontal lines at frequencies equal to 15610 and 15810 cm^{-1} highlight two diagonal peaks related to the Chl *c* Q_y transitions. The spectra were normalized to the maximum of the full $t_2 = 50$ fs spectrum, then multiplied by 20 to highlight the weak features.

not match the experimental dynamics. As discussed in Ref. [**P3**], the Chl *a* Q_y band exhibits fast decay, which suggests that some excitation is transferred to a dark state, possibly related to Fx. Adding such a state to the model might help to reproduce the experimental dynamics of the cross-peak. Nonetheless, since its parameters are completely unknown, it would severely complicate our simple effective model.

Thus, we find that our effective model of FCP supports the conclusion regarding the ultrafast energy transfer from Chl *c* to Chl *a* at room temperature.

Nonetheless, to obtain better spatial and temporal resolution, we performed additional 2D spectroscopy experiments[2], this time at 77 K, to narrow the spectral bands. A detailed account about the sample preparation and the experimental conditions is given in Ref. [**P6**].

The low temperature 2D spectra allowed us to separate two distinct diagonal peaks in the Chl *c* Q_y spectral region, as demonstrated in Fig. 1.13. Note that the amplitude of these peaks is more than 20 times lower than the amplitude of the main Chl *a* Q_y band. From the presented spectra the maxima of the two bands were identified to be at 15610 and 15810 cm^{-1} on the diagonal.

Another noteworthy thing visible from the 2D spectra in Fig. 1.13 is the totally different time evolution of the two Chl *c* Q_y bands. While at $t_2 = 50$ fs spectrum both of these bands have similar intensities, already at $t_2 = 200$ fs the

[2]Experiments were performed by Ramūnas Augulis at the lab of Donatas Zigmantas, Lund University, Sweden.

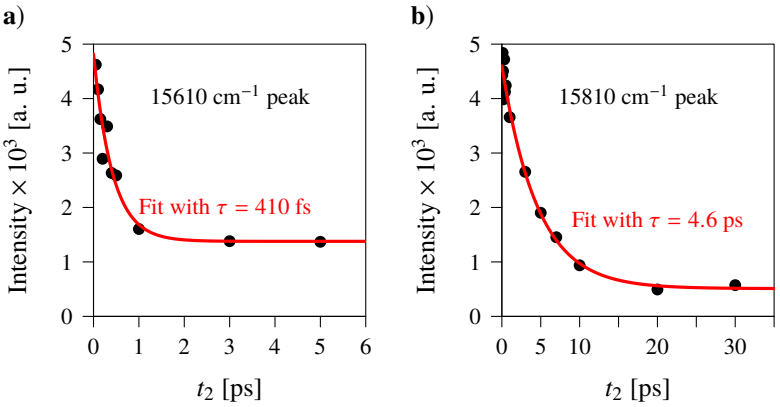

Figure 1.14: Kinetics of a) 15610 cm^{-1} diagonal peak and b) 15810 cm^{-1} diagonal peak extracted from the 2D spectra of the FCP complex shown in Fig. 1.13. Black points denote experimental data, obtained by integrating over a circle of $\sim$ 35 cm^{-1} radius. Red lines denote single exponential fitting, with time constants written in the panels.

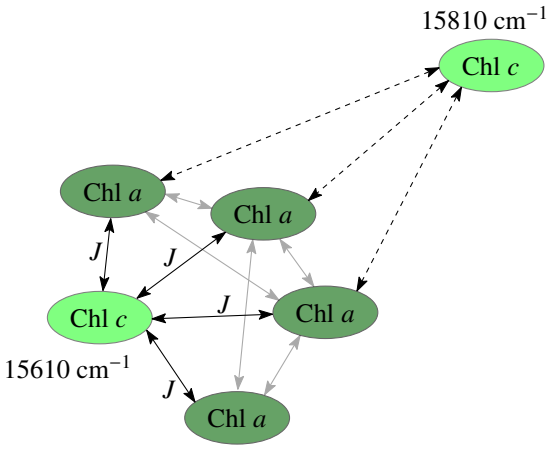

Figure 1.15: Proposed arrangement of the Chl *c* molecules in the FCP complex. The molecule responsible for the 15610 cm^{-1} transition should be surrounded by several Chl *a* molecules, to allow effective transfer. On the other hand, the molecule responsible for the 15810 cm^{-1} transition, should be spatially well separated from most of the molecules in the complex.

15610 cm^{-1} peak has decayed significantly. On the other hand, the 15810 cm^{-1} peak can still be clearly distinguished even at $t_2 = 5$ ps. These results imply completely different evolution of excitation of the two Chl *c* molecules.

To highlight the differences of the time evolutions of the two peaks, in Fig. 1.14 we plot their kinetics. It can be seen that they exhibit clear exponential decays. To verify this, we have fitted the obtained evolutions and found that a single exponential fit was sufficient. These fits are denoted as red lines

in the figure. The kinetics of the 15610 cm^{-1} peak (its first 5 ps) can be fitted with a time constant of 420 fs. Meanwhile, time constant of 4.6 ps is sufficient to explain the first 30 ps of the evolution of the 15810 cm^{-1} peak. For longer times, additional components would be present. It should also be noted that the initial evolution of both of these peaks exhibits oscillatory behavior and this might affect the accuracy of the fitting. Nonetheless, it should not change an order of magnitude difference in the obtained timescales. A detailed analysis of the oscillatory behavior of the 2D spectra of the FCP complex is presented in Ref. [**P6**].

We thus conclude that the obtained two different Chl *c* states directly transfer energy to Chl *a* on different timescales. Notice that energy transfer via intermediate states (presumably from Fxs) is not consistent with the fluorescence-excitation spectrum of FCP [40], which implies 100 % efficiency of Chl *c* to Chl *a* energy transfer, and the fact that significant portions of excitation from Fx S_1/ICT (intramolecular CT) state, a possible bridge between Chl *c* and Chl *a*, are lost due to the decay to the ground state (see Section 1.3.2).

Recent studies of FCP also suggested that there are two Chl *c* molecules in the complex [78]. Moreover, some of them can be of different types (i.e., Chl c_1, c_2, or c_3) that have slightly different absorption spectra [43]. Even if the discussed spectral features are caused by the chlorophylls of different types (thus, causing signals in different frequencies), the temporal dynamics of the corresponding peaks indicate that their interaction with the rest of the system or a surrounding environment is different. The simplest picture is that one Chl *c* is situated in the periphery of the FCP complex and is weakly coupled to the rest of Chl *a*. Thus, the excitation transfer to the core pigments is slow and we observe a picosecond decay of the peak at 15810 cm^{-1}. At the same time, the protein environment causes it to have higher energy. Another, internal Chl *c*, absorbing at 15610 cm^{-1}, must be coupled to Chl *a* stronger for faster excitation transfer. Since the cross-peak between these two transitions as well as the relevant ESA contribution is absent, the two Chls *c* in FCP are not coupled. This implies that they probably are spatially well separated.

Nevertheless, the fast energy transfer from the internal Chl *c* state still remains an issue to be explained. The strength of coupling between the Chl *c* and Chl *a* is not known, although it may be estimated from LHCII, which shares considerable sequence homology [77]. Couplings between chlorophylls in the LHCII complex were calculated to be less than 140 cm^{-1} [89]. Considering this and the fact that the transition dipole moment of the Q_y band is smaller for

Chl *c* than for Chl *a*, one can be certain that coupling between Chl *c* and Chl *a* in FCP should be even weaker. This is also supported by the absence of intense excitonic cross-peaks between Chl *a* and Chl *c* states in our 2D spectra, and the lack of circular dichroism signal related to Chl *c* [74].

The Förster energy transfer could apply in this range of parameters [30, 90]. Nevertheless, it leads to slower – picosecond – transfer rates. The 420 fs transfer timescale observed in 2D spectroscopy could be explained by using a structural model shown in Fig. 1.15. The internal Chl *c* should be coupled to several Chl *a* molecules. Thus, it transfers energy to a few Chl *a* molecules at once. The rates effectively sum-up and lead to the fast decay of the Chl *c* population. On the other hand, the second Chl *c* molecule should be further away.

The proposed schematic spatial arrangement of Chl *a* and Chl *c* molecules (shown in Fig. 1.15) is comparable to the CP29 photosynthetic antenna of PSII [91, 92]. The structure of the CP29 complex is similar to the LHCII complex, which shares the sequence homology with FCP. In CP29, there are eight Chl *a* and four Chl *b* (the absorption maximum of Chl *b* is around 15675 cm^{-1}, similarly as to Chl *c*) and one more chlorophyll binding site can be occupied by either type of chlorophyll [92], although previously it was assumed that there are 8 Chl *a* and 2 Chl *b* molecules [91]. Nonetheless, in both models, one Chl *b* molecule is well spatially separated from the other, which is strongly coupled to the rest of the Chls a of the complex. Consequently, two bands at 15650 cm^{-1} and 15385 cm^{-1} are observed in the absorption and in the pump–probe spectrum have completely different temporal dynamics: the excitation from the higher energy Chl *b* is transferred to Chl *a* with the rate of 350 fs, while transfer from the lower energy Chl *b* band occurs in 2.2 ps [91]. This implies that having two accessory chlorophylls that are in different spatial situations might be a property shared by a number of light-harvesting complexes. We speculate that it probably has a functional significance.

In a recent study of FCP based on resonance Raman technique [78], signatures of two distinct Chl *c* molecules were observed. In that study, a possible pigment organization scheme in FCP was discussed, based on the pigment binding sites of LHCII from plants [36]. It was suggested that one of Chl *c* should be bound at either the site of a614 (which is preserved in FCP) or a613 (not preserved in FCP), while the other Chl *c* should be bound at the site of b609 (preserved) or a604 (not preserved). For the internal Chl *c*, the site of b609 would be a logical choice, as it is in the vicinity of several pigments. Meanwhile, the peripheral (15810 cm^{-1}) Chl *c* could indeed be situated at the site of

a614, as that site is relatively isolated and would be in accord with slower energy transfer from this pigment. Since this pigment is situated at the periphery of the complex, it might be responsible for the inter-complex Chl *c* to Chl *a* transfer in the FCP–PSII supercomplexes [93].

1.3.2 Energy transfer from Fxs to Chls

In the previous subsection, we have discussed the energy transfer dynamics in FCP only relating to the Chl $Q_{y/x}$ bands. Yet there is also a considerable interest in the excitation dynamics after excitation of the green–blue spectral region [40–43]. As can be seen from Fig. 1.10, FCP absorbs strongly in this range. While the far blue absorption is mostly from the Soret band of Chls, the 18000–21000 cm^{-1} spectral region is due to absorption to the Fx S_2 state. Previous pump–probe studies have established the general scheme of energy relaxation dynamics following the excitation of the latter region. Most of the excitation of the Fx S_2 state relaxes to the S_1/ICT state in less than 100 fs. Note that the Fx S_1 and ICT states are difficult to separate, thus they are often treated as a single state. Meanwhile, some part of the Fx S_2 population is quickly transferred to Chl *a* (within 100–200 fs). The S_1/ICT state undergoes vibrational relaxation on the timescale between 0.5 and 1 ps, while at the same time transferring energy to Chl *a*. The remaining excitation of the S_1/ICT state decays to the ground state with a longer timescale (15 to 35 ps). Some of the previous studies suggested the existence of several spectroscopic species of Fx, yet their distinct roles have not been investigated in detail.

This is why in this subsection we present the results based on the two-color 2D spectroscopy to disentangle the energy transfer pathways in FCP following the excitation of the Fx S_2 state. Application of the two-color 2D ES is very rare due to its extreme experimental difficulty [63, 94–96]. The experimental results presented here[3] (based on Ref. [**P5**]) is the first application of the two-color 2D ES to a complicated light-harvesting complex. In the experiments, the Fx S_2 state was excited, while the Q_y state of Chls was probed (see blue and red shaded regions in Fig. 1.10). More details about the sample preparation and the experimental setup are given in Ref. [**P5**].

A few representative two-color 2D spectra of the FCP complex at different waiting times are presented in Fig. 1.16. The negative features at ω_3 from 15100 to 17400 cm^{-1} are due to the ESA of the Fx S_1/ICT state with some

[3]Experiments were performed by Egidijus Songaila and Ramūnas Augulis at the lab of Donatas Zigmantas, Lund University, Sweden.

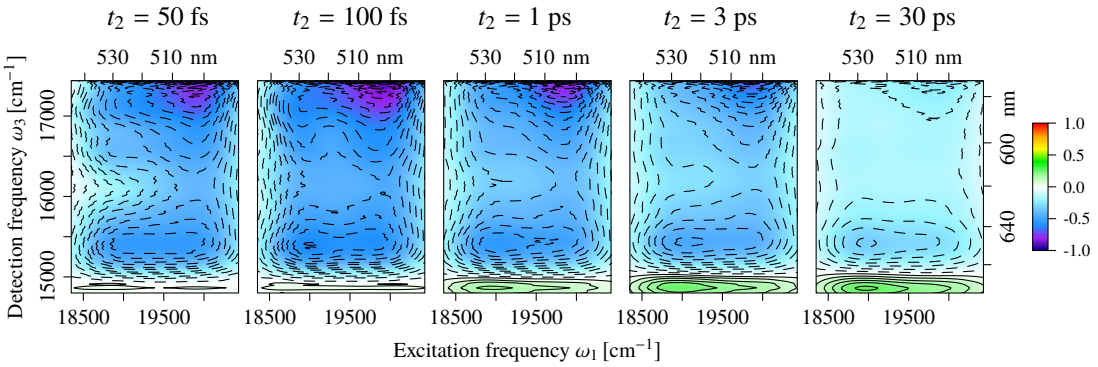

Figure 1.16: Two-color 2D spectra of the FCP complex at room temperature. The spectra are scaled to the maximum value of the spectrum at $t_2 = 100$ fs. Real part of the total spectra is given.

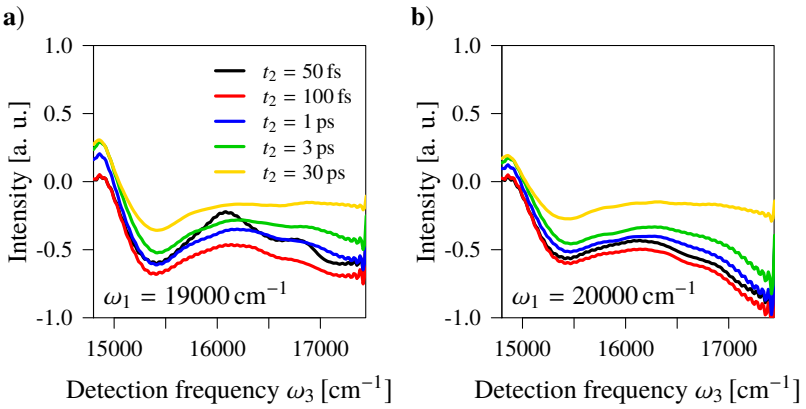

Figure 1.17: Cuts of the experimental two-color 2D spectra of the FCP complex along the ω_3 axis at different waiting times. a) excitation frequency $\omega_1 = 19000\,\mathrm{cm}^{-1}$. b) $\omega_1 = 20000\,\mathrm{cm}^{-1}$.

contributions from the ESA of Chl *a* Q_y at $\approx 15100\,\mathrm{cm}^{-1}$. Positive band at $\omega_3 \approx 14900\,\mathrm{cm}^{-1}$ corresponds to the ESE from the Chl *a* Q_y band [40, 42, 43]. It can be seen from the presented spectra that these two features have different time evolution. The positive ESE feature increases in amplitude both at early times (tens and hundreds of femtoseconds) and at later times (few picoseconds). Later, it starts to decay in tens of picoseconds. On the other hand, the negative ESA feature, while gaining amplitude at very early times (compare $t_2 = 50$ fs and $t_2 = 100$ fs spectra), already starts to decrease in amplitude within a few picoseconds, and continues to do so with tens of picoseconds.

To illustrate the time evolution of the spectral features, in Fig. 1.17 we plot the cuts of the 2D spectra of FCP along the detection frequency ω_3 axis. Since in the 2D spectra presented in Fig. 1.16 we observe differences depending on the

excitation frequency, for comparison we present cuts at excitation frequency $\omega_1 = 19000\,\mathrm{cm}^{-1}$ and $\omega_1 = 20000\,\mathrm{cm}^{-1}$ in Fig. 1.17a and b, respectively. Overall, the observed behavior is similar. The positive ESE feature at $\omega_3 \approx 14900\,\mathrm{cm}^{-1}$ increases rapidly up to the first picosecond, and continues to increase at later times. The negative ESA feature at ω_3 from 15100 to 17400 cm^{-1} shows rapid increases within the hundred femtoseconds, and then decays. Nonetheless, some differences in dynamics at different excitation frequencies can be observed. In Ref. [**P5**], existence of at least two functional Fx species in the FCP was proposed from the analysis of kinetics of several points in the 2D spectra. The $\omega_1 < 19500\,\mathrm{cm}^{-1}$ and $\omega_1 > 19500\,\mathrm{cm}^{-1}$ excitation regions were suggested to correspond to the $\mathrm{Fx}_{\mathrm{red}}$ and $\mathrm{Fx}_{\mathrm{blue}}$ species, respectively.

Time evolution of the 2D spectra can be represented by different sorts of DAS, see also Section 1.2.4. Standard DAS analysis of the 2D spectra [69, 70, 97], which is similar to the global analysis of the pump–probe spectra [68], is a powerful tool to find out the timescales of the dominant processes in the system. Nonetheless, it implies the same kinetics in all spectral region. To distinguish the differences in kinetics in the spectra, the 2D modified DAS (MDAS) [14] can be constructed. They are obtained by fitting the time evolution of each point in the 2D spectrum by a sum of decaying exponentials, and allowing to vary all free parameters of the fit *independently for each data point*. This type of approach allows to obtain the whole spectral distribution of the decay constants. In the following, both types of analysis will be presented for the 2D spectra of the FCP complex. We have chosen a four-exponential fit, because attempts to fit the spectra with smaller number of exponentials proved to be unsatisfactory. The fitting was done using the non-linear optimization algorithm based on the gradient projection method [98], as implemented in the R software [99]. Since the 2D spectra at long times (> 100 ps) show only slow decay on the order of nanoseconds, we used only times up to 100 ps for the fit.

The standard DAS of the two-color 2D spectra of FCP are presented in Fig. 1.18. The first DAS corresponds to ultrafast processes with a timescale of 30 fs. Unfortunately, the experimental $t_2 = 0$ fs spectrum is contaminated by a presence of a strong positive peak and the second lowest t_2 spectra available is that of 50 fs [**P5**]. For this reason we have to neglect the area covered by the gray rectangle in the first DAS. Nonetheless, the first DAS already shows same negative amplitude at $\omega_3 \approx 14900\,\mathrm{cm}^{-1}$, indicating that signal is growing there. Note that negative amplitude means a growth of a positive signal and a decrease of a negative signal and this is reversed for positive DAS amplitude. This im-

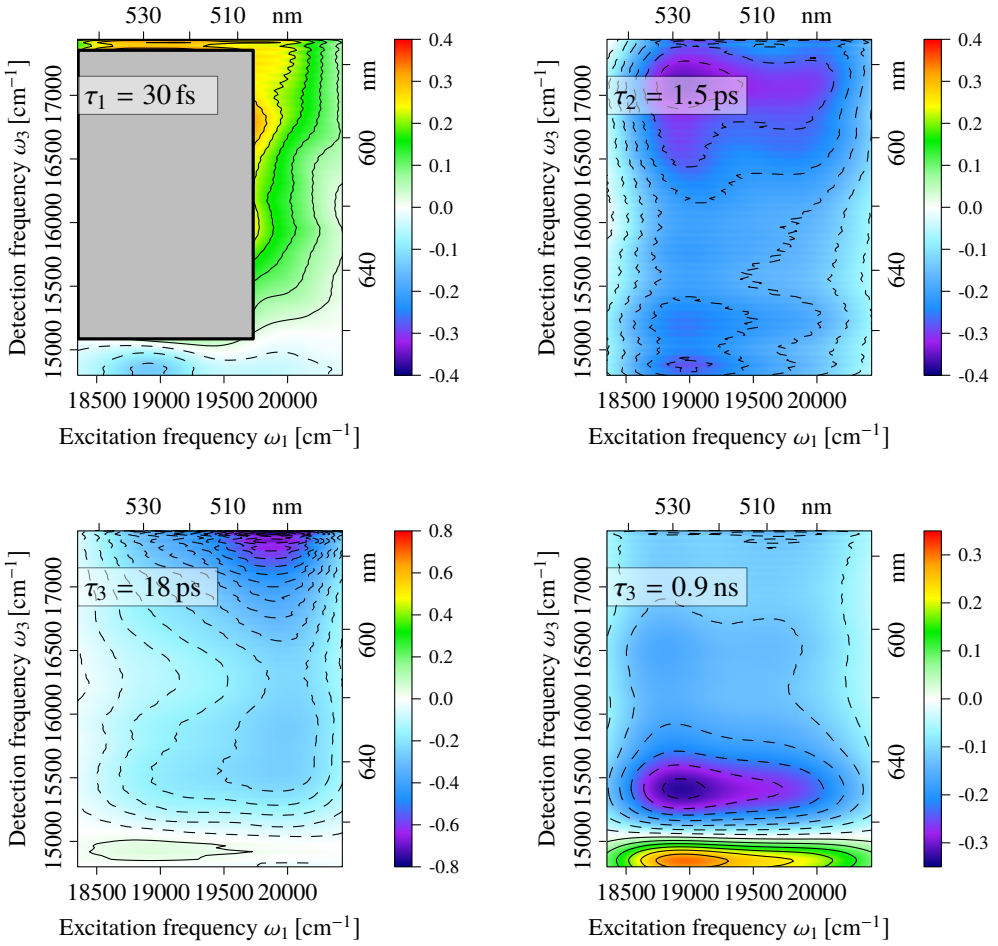

Figure 1.18: Standard 2D DAS of the 2D spectroscopy data of the FCP complex. Each plot represents the amplitude map corresponding to the separate timescale. The four timescales are $\tau_1 = 30$ fs, $\tau_2 = 1.5$ ps, $\tau_3 = 18$ ps, $\tau_4 = 0.9$ ns. Since the 2D spectrum at $t_2 = 0$ fs is contaminated by the presence of the strong positive peak (see Ref. [**P5**]), it affects the short time dynamics, thus we did not analyze the areas marked by a gray rectangle in 30 fs DAS.

plies that some part of excitation is very rapidly transferred from the Fx S_2 state to the Q_y band of Chl *a*. The second DAS, with a timescale of $\tau_2 = 1.5$ ps, has a negative amplitude throughout all the spectral area. Thus, the positive ESE feature at $\omega_3 \approx 14900\,\mathrm{cm}^{-1}$ continues to increase in amplitude, while the ESA signal of the Fx S_1/ICT decreases. The timescale of the third DAS is $\tau_3 = 18$ ps. It has a negative amplitude throughout the ESA region, implying that the amplitude of this signal continues to decrease. Finally, the fourth DAS has a timescale of $\tau_4 = 0.9$ ps and corresponds to the long-lived 2D spectra. Overall, DAS analysis is very much in line to what is known about the kinetics in FCP from the pump–probe studies, as described in the first paragraph of this subsection.

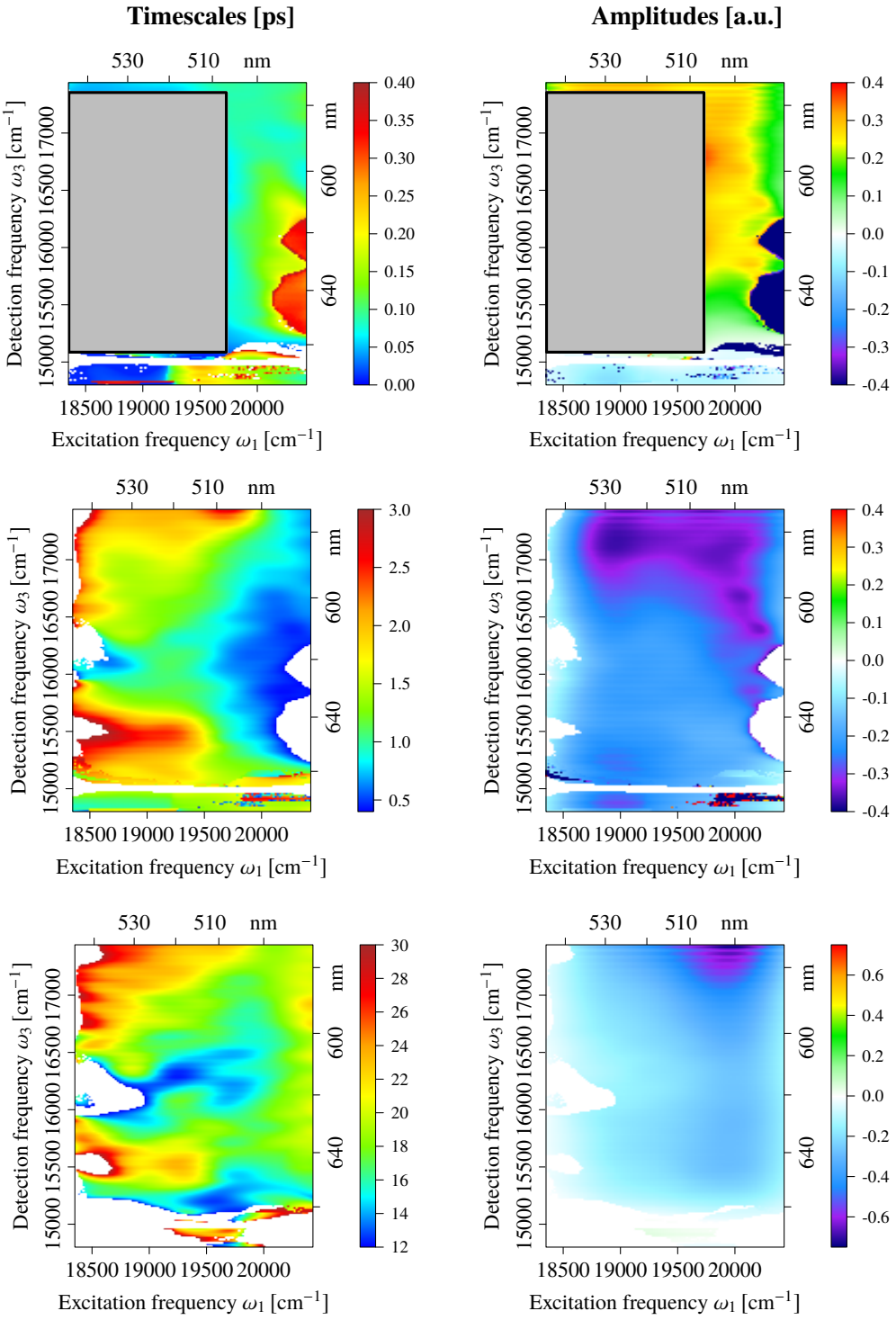

Figure 1.19: 2D MDAS of the 2D spectroscopy data of the FCP complex. The left and the right columns show the timescale and amplitude maps for separate time constant clusters, respectively. Amplitudes exceeding the maximum (or the minimum) value of the color bar are depicted with the color of maximum (or the minimum) allowed value. The amplitude map corresponding to the longest timescale (2 ns) is not shown. The areas covered by a gray rectangle were not analyzed (see text for details).

The analysis of 2D spectra in terms of DAS, however, fails to discern the dependence of the temporal evolution upon the excitation frequency ω_1. Thus, the advantage of the 2D spectroscopy versus the pump–probe spectroscopy is not utilized. The MDAS, on the other hand, can rectify this, as can be seen from Fig. 1.19. There timescale and amplitude maps corresponding to the distinct timescale clusters are shown. The first row corresponds to timescales between 0 and 400 fs, the second – between 0.4 and 3 ps, while the third – between 12 and 30 ps. The longest timescale was fixed to 2 ns, as in Ref. [14], and the obtained amplitude map is very similar to that of 0.9 ns DAS (Fig. 1.18), thus not shown. The most important thing is that the MDAS show significant heterogeneity in both the timescales and the amplitudes.

The MDAS of shortest timescales (first row in Fig. 1.19) illustrate the ultrafast processes on timescales shorter than 400 fs. After excitation of the $\mathrm{Fx_{red}}$ species ($\omega_1 < 19500\,\mathrm{cm^{-1}}$) we observe < 50 fs processes in the Chl *a* Q_y ESE ($\omega_3 \approx 14900\,\mathrm{cm^{-1}}$) and $\mathrm{S_1}$/ICT ESA regions ($\omega_3 \approx 17400\,\mathrm{cm^{-1}}$). Due to the limited number of early time 2D spectra, we cannot resolve the exact timescale of these processes with certainty. The rates of $\mathrm{S_2}$ to $\mathrm{S_1}$/ICT internal conversion and energy transfer from $\mathrm{S_2}$ to Chl *a* must, therefore, be similar. As in the case of $\tau = 30$ fs DAS, we did not analyze the area covered by the gray rectangle. It is important to note that we discern differences depending on the excitation frequency. Excitation of $\mathrm{Fx_{blue}}$ ($\omega_1 > 19500\,\mathrm{cm^{-1}}$) leads to a slower evolution in the Chl *a* Q_y ESE region as the signal there grows with a timescale between 100 and 200 fs. The $\mathrm{S_1}$/ICT ESA region ($\omega_3 \gtrsim 15100\,\mathrm{cm^{-1}}$) evolves with times < 100 fs, again indicating efficient internal conversion.

Processes with timescales between 0.4 ps and 3 ps are represented by the MDAS shown in the second row of Fig. 1.19. Again, $\mathrm{Fx_{red}}$ and $\mathrm{Fx_{blue}}$ spectral regions show different timescale values. After excitation of the $\mathrm{Fx_{red}}$ a 0.9–1.2 ps growth component is observed in the Chl *a* Q_y region ($\omega_3 \approx 14900\,\mathrm{cm^{-1}}$), while the decay constants of the $\mathrm{S_1}$/ICT ESA region ($\omega_3 \gtrsim 15100\,\mathrm{cm^{-1}}$) are 1–3 ps. The $\mathrm{S_1}$/ICT ESA shows faster 0.5–2 ps evolution when the $\mathrm{Fx_{blue}}$ is excited, and the evolution of the Chl *a* Q_y region is slower (1.2–1.6 ps). The amplitude map of this MDAS shows that changes in the Chl *a* Q_y region are more significant when $\mathrm{Fx_{red}}$ is excited. Note that two processes contribute to the $\mathrm{S_1}$/ICT dynamics in this timescale window, namely vibrational cooling of the hot Fx $\mathrm{S_1}$/ICT state and energy transfer to Chls. Unfortunately, our analysis does not allow us to distinguish between these processes, thus, we can not estimate the vibrational cooling rate nor determine whether excitation transfer to Chl *a*

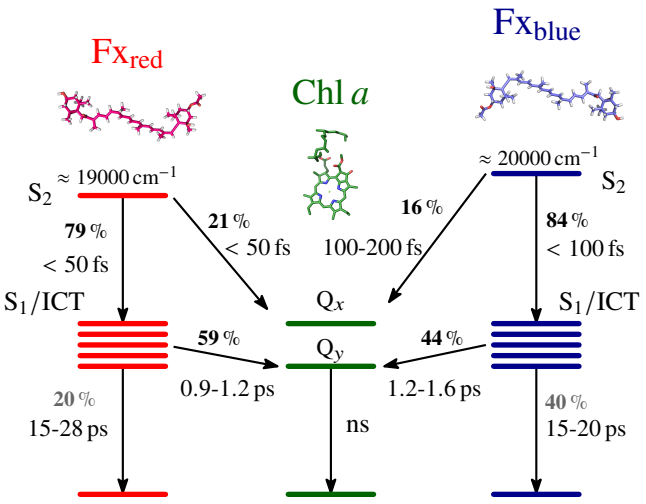

Figure 1.20: Scheme of the energy transfer pathways in the FCP complex obtained from the two-color 2D spectra and the modified decay associated spectra.

occurs via hot or relaxed S_1/ICT states.

Processes with timescales between 12 ps and 40 ps are given by the MDAS shown in the third row of 1.19. The decay timescales of 15–20 ps are slightly faster when the Fx_{blue} is excited, compared to the 15–28 ps timescales obtained upon the Fx_{red} excitation. The amplitude map shows that this decay is much stronger upon Fx_{blue} excitation, implying that the overall transfer efficiency to Chl *a* is lower for Fx_{blue}.

Thus, two-color 2D spectroscopy performed on a photosynthetic protein from diatoms clearly distinguishes "red" and "blue" functional species of Fx and reveals that their excitation results in qualitatively distinct spectral evolutions. From the 2D spectra and subsequent MDAS analysis we conclude that their S_2 energies correspond to the transitions at approximately 19000 cm^{-1} and 20000 cm^{-1}, respectively. Recently it was shown that three Fx species could be distinguished in FCP [100], based on their resonant Raman properties. Our data and analysis indicate that two of these species are preferably excited at 19000 and 20000 cm^{-1}. Meanwhile, the existence of a third Fx species would only be consistent with our data if its excitation energy were $>$ 20500 cm^{-1}, which is not covered with our pulses.

Having all this in mind, we construct a comprehensive energy transfer scheme for the FCP that includes both Fx species (Fig. 1.20). The timescales were obtained from the MDAS analysis. Meanwhile, the relative amplitudes were obtained as follows: from the FCP fluorescence-excitation spectrum given in Ref. [40] the overall transfer yield after Fx_{red} and Fx_{blue} excitation was estimated to be 80 % and 60 %, respectively. The ratios of the S_2 to Chl *a* and

S_1/ICT to Chl *a* transfer were obtained from the amplitude maps of the MDAS given in the first and second row of Fig. 1.19 and the remaining amplitudes were derived from the compartmental model as $A_{S_1/ICT \leftarrow S_2} + A_{Chl\,a \leftarrow S_2} = 1$ and $A_{Chl\,a \leftarrow S_1/ICT} + A_{S_0 \leftarrow S_1/ICT} = A_{S_1/ICT \leftarrow S_2}$.

Our energy transfer scheme in Fig. 1.20 shows the major excitation relaxation pathways. Some excitation energy is very rapidly transferred from both Fx_{blue} S_2 and Fx_{red} S_2 to Chl *a*. This transfer is slower for Fx_{blue}. Nonetheless, most of the excitation from the Fx_{blue} S_2 and Fx_{red} S_2 states relaxes to their respective S_1/ICT states within 100 femtoseconds. From there, Fx_{red} transfers most of its excitation (59 %) to Chl *a*, while this transfer is slightly less efficient from Fx_{blue} (44 %). This transfer step is again slower for Fx_{blue}. From this we conclude that the Fx_{red} pigments should either be more strongly coupled to the Chl *a* pigments (being closer or having a more favorable orientation) or their electronic states must be closer in energy to the Chl *a* states, since the excitation transfer is faster from those pigments both from S_2 and S_1/ICT states. Nevertheless, 20 % (Fx_{red}) or even 40 % (Fx_{blue}) of excitation is not transferred to Chls, but relaxes to the ground state. This might be surprising, since the transfer rates from S_1/ICT to Chl *a* Q_y are much faster than decay to the ground state, and only a small fraction of excitation population should be lost as a result of the latter process. It mus be highlighted, however, that the transfer rates and amplitudes in our scheme represent averaged values, which could be greatly affected if the Fx molecules in the whole complex are distributed non-uniformly. The existence of at least one poorly transferring Fx_{blue} is consistent with previous suggestions [40, 41] and with the amplitude map of the MDAS corresponding to the timescales of tens of picoseconds (third row in Fig. 1.19). We also note that the direct interaction between the S_1/ICT states of Fx_{red} and Fx_{blue} must be weak, because they decay to the ground state with distinct lifetimes, whereas strong interaction would lead to decay with the same rate [84, 85]. Overall, the energy transfer schemes of FCP, obtained from the pump–probe studies [40–43], are mostly consistent with our results. The scheme presented here, however, is more detailed, as it includes not only timescales but also the relative amplitudes of transfer pathways.

1.4 Conclusions

In this chapter, we have introduced the 2D spectroscopy. This technique provides a wealth of information, but its extraction can be difficult. Here we have

attempted to ease the transition from the pump–probe to the 2D spectroscopy by making a detailed explanation of its specific features. This was done by considering numerous examples of simple model systems.

Yet the full force of a spectroscopic technique can be felt only when it is applied to the real-world problems. In this chapter we have reported the 2D spectra of the FCP complex. FCP is the major light-harvesting complex from diatoms, which contribute heavily to the global primary production. Unfortunately, the crystal structure of FCP is not available yet, thus detailed microscopic models (such as of the PSII RC, presented in Chapter 3) are not possible. Thus, this chapter is a demonstration on how detailed analysis and simple modeling of the 2D spectra can provide insights to both functional and structural relationships in a photosynthetic complex.

First, the role of the Chl *c* pigment in FCP was studied. Analysis of the experimental 2D spectra at room temperature suggested an ultrafast energy transfer from Chl *c* to Chl *a* pigments. We have constructed a simple theoretical model, which supported this conclusion. Further analysis of 77 K 2D spectra have shown the existence of two spectrally distinct Chl *c* molecules. Knowledge of the relevant energy transfer mechanisms and their characteristic timescales allowed us to suggest a possible structural arrangement of Chl pigments in the FCP complex.

Second, the energy transfer cascades in FCP after the excitation of the Fx S_2 band was investigated with the help of two-color 2D spectroscopy. Analysis of the experimental data implied that there are two spectroscopically distinct Fx species in the FCP complex. A more detailed picture was obtained from the data analysis in terms of the MDAS, which revealed a considerable heterogeneity in timescales and amplitudes. This lead to a proposed detailed scheme of the energy transfer pathways in the FCP complex.

All this allows us to formulate the **first statement of the thesis**: Analysis of the experimental 2D spectroscopy data of the FCP complex, supplemented with theoretical insights and representation in terms of suitable decay associated spectra, enabled to propose both a possible structural scheme and a detailed scheme of energy transfer pathways.

The introduction to the 2D spectroscopy presented in the first part of this chapter is mostly based on [**p8**] and [**P1**]. Reported results on the 2D spectroscopy of FCP are based on [**P3**, **P5**, **P6**].

Chapter 2

Spectroscopic properties of molecular aggregates

> Sloppiness. Disorganization. As I've tried to teach you, undisciplined thinking can make even the simplest task impossible!
>
> ULTRA MAGNUS, The Transformers G1

In this chapter we formulate the theoretical description of the molecular aggregates and their spectroscopic properties. We introduce the tight-binding Hamiltonian, which extends the Frenkel exciton Hamiltonian by taking into account the CT states. Then we obtain the expressions for the relevant response functions to describe absorption, linear and circular dichroism spectra using the cumulant expansion and the ctR theory. Absorption spectra of a molecular dimer obtained from this description are then compared to other well-known approaches. This theory is then applied to describe the Stark spectroscopy. Finally, the well-known expression for the 2D spectroscopy response functions are extended with ctR theory terms.

2.1 Tight-binding Hamiltonian

To describe the molecular system we use the tight-binding Hamiltonian [**P2**, 101], which is an extension of the Frenkel exciton model [25] that enables the inclusion of CT states. This method is similar to other recent descriptions of Frenkel excitons and CT states in molecular systems [102–104]. In Chapter 3

this model will be applied to the PSII RC, but its formulation is independent of any particular molecular system.

We consider the ground and the single-excited state manifolds, which are sufficient to calculate the linear spectra. The global ground state is denoted by g, and its energy is set to zero. In the single-excited state manifold we have the molecular (pigment) excitation states n^*, with excitation localized on a single site n, and the CT states m^+n^-, which are not accounted for in the Frenkel exciton model. To describe the CT states, we introduce separate creation and annihilation operators for electrons and holes. Thus $\hat{\boldsymbol{e}}_n^\dagger$ ($\hat{\boldsymbol{e}}_n$) creates (annihilates) an electron on site n, and $\hat{\boldsymbol{h}}_n^\dagger$ $\left(\hat{\boldsymbol{h}}_n\right)$ creates (annihilates) a hole on site n. Then molecular excitation (ME) states are described by $\hat{\boldsymbol{e}}_n^\dagger \hat{\boldsymbol{h}}_n^\dagger |g\rangle = |n^*\rangle$ and CT states by $\hat{\boldsymbol{e}}_n^\dagger \hat{\boldsymbol{h}}_m^\dagger |g\rangle = |m^+n^-\rangle$. The electron and hole creation and annihilation operators satisfy the Fermi commutation relations [**P2**, 101].

The total Hamiltonian consists of the Hamiltonians of the system, the bath, and their interaction:

$$\hat{H} = \hat{H}_\mathrm{S} + \hat{H}_\mathrm{B} + \hat{H}_\mathrm{SB}. \tag{2.1}$$

The electronic degrees of freedom compose the system, which is described by the tight-binding Hamiltonian:

$$\begin{aligned}\hat{H}_\mathrm{S} = &\sum_m^N \sum_n^N t_{mn}^{\boldsymbol{e}} \hat{\boldsymbol{e}}_m^\dagger \hat{\boldsymbol{e}}_n + \sum_m^N \sum_n^N t_{mn}^{\boldsymbol{h}} \hat{\boldsymbol{h}}_m^\dagger \hat{\boldsymbol{h}}_n \\ &- \sum_m^N \sum_n^N V_{mn}^{\boldsymbol{eh}} \hat{\boldsymbol{e}}_m^\dagger \hat{\boldsymbol{h}}_n^\dagger \hat{\boldsymbol{h}}_n \hat{\boldsymbol{e}}_m + \sum_m^N \sum_n^{m\neq n} J_{mn} \hat{\boldsymbol{e}}_m^\dagger \hat{\boldsymbol{h}}_m^\dagger \hat{\boldsymbol{h}}_n \hat{\boldsymbol{e}}_n.\end{aligned} \tag{2.2}$$

Here $t_{mn}^{\boldsymbol{e}}$ $\left(t_{mn}^{\boldsymbol{h}}\right)$ is the electron (hole) hopping rate between LUMO (HOMO) orbitals of different pigments. Diagonal elements $t_{mm}^{\boldsymbol{e/h}}$ correspond to the orbital energies. N is the number of molecules, and the total number of states in the single-excited state manifold is $N_\mathrm{tot} = N^2$. J_{mn} is the resonance coupling between the molecular excitations on sites m and n. The term $V_{mn}^{\boldsymbol{eh}}$ corresponds to the electron–hole Coulomb attraction energy between sites m and n (see Eq. (2.25)). Note that the electron–electron and hole–hole repulsion terms are not needed to describe the single excitation manifold. For this Hamiltonian, the energies of the excited states are

$$\langle n^*|\hat{H}_\mathrm{S}|n^*\rangle = \varepsilon_{n^*} = t_{nn}^{\boldsymbol{e}} + t_{nn}^{\boldsymbol{h}} - V_{nn}^{\boldsymbol{eh}}; \tag{2.3}$$

$$\langle m^+n^-|\hat{H}_\mathrm{S}|m^+n^-\rangle = \varepsilon_{m^+n^-} = t_{nn}^{\boldsymbol{e}} + t_{mm}^{\boldsymbol{h}} - V_{nm}^{\boldsymbol{eh}}. \tag{2.4}$$

Here ε_n^* is the energy of the ME state n^* (site energy), $\varepsilon_{m^+n^-}$ is the energy of the CT state m^+n^-. Note that for calculations only the energies and not their constituent terms need to be specified. The couplings between different excited states are

$$\langle n^*|\hat{H}_\mathrm{S}|m^*\rangle = J_{nm}; \tag{2.5}$$

$$\langle n^*|\hat{H}_\mathrm{S}|k^+l^-\rangle = t^{\boldsymbol{e}}_{nl}\delta_{nk} + t^{\boldsymbol{h}}_{nk}\delta_{nl}; \tag{2.6}$$

$$\langle m^+n^-|\hat{H}_\mathrm{S}|k^+l^-\rangle = t^{\boldsymbol{e}}_{nl}\delta_{mk} + t^{\boldsymbol{h}}_{mk}\delta_{nl}. \tag{2.7}$$

Thus, couplings involving the CT states are related, which is not the case if the CT states are treated as additional molecular excitation states [105–107].

All vibrational degrees of freedom of the molecules themselves and their environment compose the bath and are represented by an infinite set of harmonic oscillators with the Hamiltonian:

$$\hat{H}_\mathrm{B} = \sum_j \frac{\omega_j}{2}\left(\hat{p}_j^2 + \hat{x}_j^2\right). \tag{2.8}$$

Here ω_j is the frequency, $\hat{p}_j$ – the dimensionless momentum, and $\hat{x}_j$ – the dimensionless coordinate of the jth bath mode. We remind the reader that we set $\hbar = 1$ throughout the thesis. The system–bath coupling is assumed to be linear in the bath coordinates:

$$\begin{aligned}\hat{H}_\mathrm{SB} = &-\sum_n^N \sum_j \omega_j d^{\boldsymbol{eh}}_{nn,j}\hat{x}_j \hat{\boldsymbol{e}}_n^\dagger \hat{\boldsymbol{h}}_n^\dagger \hat{\boldsymbol{h}}_n \hat{\boldsymbol{e}}_n \\ &-\sum_m^N \sum_n^{m\neq n} \sum_j \omega_j d^{\boldsymbol{eh}}_{mn,j}\hat{x}_j \hat{\boldsymbol{e}}_m^\dagger \hat{\boldsymbol{h}}_n^\dagger \hat{\boldsymbol{h}}_n \hat{\boldsymbol{e}}_m.\end{aligned} \tag{2.9}$$

Here the two terms are separated for future convenience. The parameter $d^{\boldsymbol{eh}}_{nn,j}$ $\left(d^{\boldsymbol{eh}}_{mn,j}\right)$ is the dimensionless displacement of the equilibrium configuration of the jth bath mode between the ground state and the excited state of the nth molecule (n^+m^- CT state). This formulation differs from the previous applications of the tight-binding model, where the bath was coupled to electron and hole orbitals and not to the excited states themselves [**P2**, 101]. The present approach is more natural when describing excitations in a molecular aggregate and not in a solid state system.

We introduce bath operators $\hat{F}_n = -\sum_j \omega_j d^{\boldsymbol{eh}}_{nn,j}\hat{x}_j$ and $\hat{F}_{mn} = -\sum_j \omega_j d^{\boldsymbol{eh}}_{mn,j}\hat{x}_j$, enabling us to rewrite the system–bath coupling Hamiltonian as

$$\hat{H}_\mathrm{SB} = \sum_n^N \hat{F}_n \hat{\boldsymbol{e}}_n^\dagger \hat{\boldsymbol{h}}_n^\dagger \hat{\boldsymbol{h}}_n \hat{\boldsymbol{e}}_n + \sum_m^N \sum_n^{m\neq n} \hat{F}_{mn} \hat{\boldsymbol{e}}_m^\dagger \hat{\boldsymbol{h}}_n^\dagger \hat{\boldsymbol{h}}_n \hat{\boldsymbol{e}}_m. \tag{2.10}$$

For simplicity, we subsequently denote both the ME and the CT states by capital letters $A, B, \ldots$ Then summation over all single-excited states is expressed as

$$\sum_{A}^{N_{\mathrm{tot}}} z_A = \sum_{n}^{N} z_n + \sum_{m}^{N} \sum_{n}^{m \neq n} z_{mn}. \tag{2.11}$$

Here z_A denotes any quantity related to the state A. The reorganization energies of the excited states are defined as $\lambda_A = \sum_j \omega_j \left(d_{A,j}^{\boldsymbol{eh}}\right)^2 /2$.

For a harmonic bath, the key quantities that describe the bath effects are the correlation functions [30, 86, 108]:

$$C_{AB}(\tau_2 - \tau_1) = \mathrm{Tr_B}\left(\hat{F}_A^{\mathrm{I}}(\tau_2)\, \hat{F}_B^{\mathrm{I}}(\tau_1)\, \hat{\rho}_{\mathrm{B}}^{\mathrm{eq}}\right), \tag{2.12}$$

since

$$\mathrm{Tr_B}\left(\hat{F}_A^{\mathrm{I}}(t)\right) = 0. \tag{2.13}$$

Here

$$\hat{F}_A^{\mathrm{I}}(t) = \mathrm{e}^{\mathrm{i}\left(\hat{H}_{\mathrm{S}} + \hat{H}_{\mathrm{B}}\right)t} \hat{F}_A \mathrm{e}^{-\mathrm{i}\left(\hat{H}_{\mathrm{S}} + \hat{H}_{\mathrm{B}}\right)t} = \mathrm{e}^{\mathrm{i}\hat{H}_{\mathrm{B}}t} \hat{F}_A \mathrm{e}^{-\mathrm{i}\hat{H}_{\mathrm{B}}t} \tag{2.14}$$

defines the operator in the interaction representation. The equilibrium bath density operator is

$$\hat{\rho}_{\mathrm{B}}^{\mathrm{eq}} = \frac{\exp\left(-\beta \hat{H}_{\mathrm{B}}\right)}{\mathrm{Tr_B}\left(\exp\left(-\beta \hat{H}_{\mathrm{B}}\right)\right)} \tag{2.15}$$

with $\beta = (k_{\mathrm{B}} T)^{-1}$ being the inverse temperature in energy units, and k_{B} – the Boltzmann constant. The spectral densities

$$C''_{AB}(\omega) = \pi \sum_j \frac{\omega_j^2 d_{A,j}^{\boldsymbol{eh}} d_{B,j}^{\boldsymbol{eh}}}{2} \left(\delta\left(\omega - \omega_j\right) - \delta\left(\omega + \omega_j\right)\right) \tag{2.16}$$

describe the bath in the frequency domain. They show how strongly the system states are coupled to the specific frequency bath modes. From the spectral densities the bath correlation functions can be calculated as

$$C_{AB}(t) = \frac{1}{\pi} \int_{-\infty}^{\infty} \mathrm{d}\omega \frac{1}{1 - \mathrm{e}^{-\beta\omega}} \mathrm{e}^{-\mathrm{i}\omega t} C''_{AB}(\omega)\,. \tag{2.17}$$

The reorganization energies are also related to the spectral densities:

$$\lambda_A = \frac{1}{\pi} \int_{0}^{\infty} \mathrm{d}\omega \frac{C''_{AA}(\omega)}{\omega}. \tag{2.18}$$

Diagonalization of the system Hamiltonian (Eq. (2.2)) leads to the introduction of the generalized exciton basis (denoted as such, because it includes not only Frenkel but also CT excitons):

$$|e\rangle = \sum_{A}^{N_{\text{tot}}} \psi_{e,A}|A\rangle \tag{2.19}$$

with $\psi_{e,A} = \langle e|\hat{U}^{\dagger}|A\rangle$ being the elements of transformation matrix $\hat{U}^{\dagger}$, which satisfies

$$\left(\hat{H}_{\text{S}}\right)^{\text{EB}} = \hat{U}^{\dagger}\left(\hat{H}_{\text{S}}\right)^{\text{SB}}\hat{U}. \tag{2.20}$$

Here the superscript EB (SB) means the generalized exciton (site) basis. We assume that the matrix elements $\psi_{e,A}$ are real. In the generalized exciton basis, the bath correlation functions are

$$\begin{aligned} C_{e_1e_2,e_3e_4}(\tau_2-\tau_1) &= \text{Tr}_{\text{B}}\left(\hat{F}^{\text{I}}_{e_1e_2}(\tau_2)\,\hat{F}^{\text{I}}_{e_3e_4}(\tau_1)\,\hat{\rho}^{\text{eq}}_{\text{B}}\right) \\ &= \sum_{A}^{N_{\text{tot}}}\sum_{B}^{N_{\text{tot}}}\psi_{e_1,A}\psi_{e_2,A}\psi_{e_3,B}\psi_{e_4,B}C_{AB}(\tau_2-\tau_1)\,. \end{aligned} \tag{2.21}$$

with

$$\hat{F}_{e_1e_2} = \langle e_1|\hat{H}_{\text{SB}}|e_2\rangle. \tag{2.22}$$

Similarly one can introduce the spectral density in the generalized exciton basis. The lineshape functions, required to describe the optical lineshapes (see Section 2.2), are defined as

$$g_{e_1e_2,e_3e_4}(t) = \int_0^t \mathrm{d}\tau_2 \int_0^{\tau_2} \mathrm{d}\tau_1 C_{e_1e_2,e_3e_4}(\tau_2-\tau_1)\,. \tag{2.23}$$

When static disorder is present in the system, the energies of the states are different in each particular case of the ensemble. Thus in the system Hamiltonian (Eq. (2.2)) one needs to change $V^{\boldsymbol{eh}}_{nn} \rightarrow V^{\boldsymbol{eh}}_{nn} + \delta\varepsilon_{n^*}$ and $V^{\boldsymbol{eh}}_{mn} \rightarrow V^{\boldsymbol{eh}}_{mn} + \delta\varepsilon_{n^+m^-}$, with $\delta\varepsilon_{n^*}$ and $\delta\varepsilon_{n^+m^-}$ being random numbers from a Gaussian distribution with zero mean and some chosen standard deviations σ_{n^*} and $\sigma_{n^+m^-}$. All observable quantities then have to be averaged over disorder, i. e. $\bar{X} = \langle X\rangle_{\text{dis}}$.

2.1.1 Double-excited states

To simulate 2D optical spectroscopy experiments, we have to describe the double-excited states. There are two excited electrons and two excited holes

in the state $|m^+k^-n^+l^-\rangle = \hat{\boldsymbol{e}}_k^\dagger \hat{\boldsymbol{e}}_l^\dagger \hat{\boldsymbol{h}}_m^\dagger \hat{\boldsymbol{h}}_n^\dagger |g\rangle$ with $k > l$ and $m > n$. Three kinds of double-excited states are possible: ME–ME states m^*n^*, ME–CT states $m^*n^+k^-$ and CT–CT states $m^+n^-k^+l^-$. The total number of double-excited states is $N_{2\text{tot}} = N^2 (N-1)^2 /4$.

To properly describe these states we have to augment the Hamiltonian with a few additional terms:

$$\hat{H}_{\text{S}}^{(\text{II})} = \frac{1}{2}\sum_m^N \sum_n^{m\neq n} V_{mn}^{\boldsymbol{e}} \hat{\boldsymbol{e}}_m^\dagger \hat{\boldsymbol{e}}_n^\dagger \hat{\boldsymbol{e}}_n \hat{\boldsymbol{e}}_m + \frac{1}{2}\sum_m^N \sum_n^{m\neq n} V_{mn}^{\boldsymbol{h}} \hat{\boldsymbol{h}}_m^\dagger \hat{\boldsymbol{h}}_n^\dagger \hat{\boldsymbol{h}}_n \hat{\boldsymbol{h}}_m + \frac{1}{4}\sum_k^N \sum_m^{k\neq m} \sum_l^N \sum_n^{l\neq n} K_{kl,mn} \hat{\boldsymbol{e}}_k^\dagger \hat{\boldsymbol{h}}_l^\dagger \hat{\boldsymbol{e}}_m^\dagger \hat{\boldsymbol{h}}_n^\dagger \hat{\boldsymbol{h}}_n \hat{\boldsymbol{e}}_m \hat{\boldsymbol{h}}_l \hat{\boldsymbol{e}}_k . \tag{2.24}$$

Here $V_{mn}^{\boldsymbol{e}}$ ($V_{mn}^{\boldsymbol{h}}$) is the electron–electron (hole–hole) Coulomb repulsion energy, and the K couplings describe the interaction between the static dipoles of the pigments with other static dipoles or the charges and thus are responsible for the electrochromic shifts. Explicitly, we have

$$V_{mn}^{\boldsymbol{e}} = V_{mn}^{\boldsymbol{h}} = V_{mn}^{\boldsymbol{eh}} = \frac{e^2}{4\pi\epsilon_0\epsilon_r \left|\vec{R}_{mn}\right|}; \tag{2.25}$$

$$K_{mm,nn} = \frac{1}{4\pi\epsilon_0\epsilon_r}\left(\frac{(\Delta\vec{\mu}_m \cdot \Delta\vec{\mu}_n)}{\left|\vec{R}_{mn}\right|^3} - 3\frac{\left(\Delta\vec{\mu}_m \cdot \vec{R}_{mn}\right)\left(\Delta\vec{\mu}_n \cdot \vec{R}_{mn}\right)}{\left|\vec{R}_{mn}\right|^5} \right); \tag{2.26}$$

$$K_{mm,kn} = \frac{e}{4\pi\epsilon_0\epsilon_r}\left(\frac{\left(\vec{R}_{nm} \cdot \Delta\vec{\mu}_m\right)}{\left|\vec{R}_{nm}\right|^3} - \frac{\left(\vec{R}_{km} \cdot \Delta\vec{\mu}_m\right)}{\left|\vec{R}_{km}\right|^3} \right). \tag{2.27}$$

$$K_{nm,lk} = 0.$$

Here e is the electron charge, ϵ_r is the relative dielectric constant, $\vec{R}_{mn} = \vec{R}_m - \vec{R}_n$ is the distance vector from n to m pigments, with $\vec{R}_m$ being the position vector corresponding to the center of the pigment m. $\Delta\vec{\mu}_m$ is the difference between the dipole moments of the excited and the ground states, see Eq. 2.70. Note that Eq. 2.25 is not applicable to $V_{mm}^{\boldsymbol{eh}}$, some effective value should be used instead.

In this formulation, the energies of the double-excited states are:

$$\varepsilon_{m^*n^*} = \varepsilon_{m^*} + \varepsilon_{n^*} + K_{mm,nn}; \tag{2.28}$$

$$\varepsilon_{m^*n^+k^-} = \varepsilon_{m^*} + \varepsilon_{n^+k^-} + K_{mm,kn}; \tag{2.29}$$

$$\varepsilon_{m^+n^-k^+l^-} = \varepsilon_{m^+n^-} + \varepsilon_{k^+l^-} + V^e_{nl} + V^h_{mk} - V^{eh}_{nk} - V^{eh}_{ml}. \tag{2.30}$$

It is obvious that due to the strong Coulomb interaction effects, the energies of the CT–CT states will be significantly shifted, effectively decoupling them from the rest of the double-excited states. Therefore, they will be neglected in the following.

The couplings between the remaining double-excited states are:

$$\begin{aligned} J_{m^*n^*,m'^*n'^*} &= J_{m^*,m'^*}\,(1-\delta_{mm'})\,\delta_{nn'} + J_{m^*,n'^*}\,(1-\delta_{mn'})\,\delta_{nm'} \\ &\quad + J_{n^*,m'^*}\,(1-\delta_{nm'})\,\delta_{mn'} + J_{n^*,n'^*}\,(1-\delta_{nn'})\,\delta_{mm'}; \end{aligned} \tag{2.31}$$

$$J_{m^*n^+k^-,m'^*n'^*} = \delta_{mm'} J_{n'^*,n^+k^-} + \delta_{mn'} J_{m'^*,n^+k^-}; \tag{2.32}$$

$$\begin{aligned} J_{m^*n^+k^-,m'^*n'^+k'^-} &= \delta_{mm'} J_{n^+k^-,n'^+k'^-} + \delta_{nn'}\delta_{kk'}\,(1-\delta_{mm'})\,J_{m^*,m'^*} \\ &\quad + \delta_{mn'}\delta_{nm'}\delta_{kk'} J_{m^*,m^+m'^-} + \delta_{mk'}\delta_{nn'}\delta_{km'} J_{m^*,m'^+m^-}. \end{aligned} \tag{2.33}$$

Here $J_{m^*n^*,m'^*n'^*}$ is the coupling between ME–ME states m^*n^* and $m'^*n'^*$, $J_{m^*n^+k^-,m'^*n'^*}$ is the coupling between ME–CT state $m^*n^+k^-$ and ME–ME state $m'^*n'^*$, $J_{m^*n^+k^-,m'^*n'^+k'^-}$ is the coupling between ME–CT states $m^*n^+k^-$ and $m'^*n'^+k'^-$.

Additionally, we have to augment the system–bath coupling Hamiltonian by

$$\hat{H}^{(\mathrm{II})}_{\mathrm{SB}} = \sum_m^N \sum_n^{m\neq n} \hat{F}^{\boldsymbol{ee}}_{mn} \hat{\boldsymbol{e}}^\dagger_m \hat{\boldsymbol{e}}^\dagger_n \hat{\boldsymbol{e}}_n \hat{\boldsymbol{e}}_m + \sum_m^N \sum_n^{m\neq n} \hat{F}^{\boldsymbol{hh}}_{mn} \hat{\boldsymbol{h}}^\dagger_m \hat{\boldsymbol{h}}^\dagger_n \hat{\boldsymbol{h}}_n \hat{\boldsymbol{h}}_m. \tag{2.34}$$

The bath operators are assumed to be equal to

$$\hat{F}^{\boldsymbol{ee}}_{mn} = \hat{F}^{\boldsymbol{hh}}_{mn} = -\hat{F}_{mn} = -\hat{F}_{nm}, \tag{2.35}$$

due to the sign of the charges involved.

We introduce the double-excitation eigenstates

$$|f\rangle = \sum_{k,l}^{k>l} \sum_{m,n}^{m>n} \Psi_{f,klmn} |m^+k^-n^+l^-\rangle. \tag{2.36}$$

The transformation matrix $\Psi_{f,klmn}$ is calculated by diagonalizing the double-excitation blocks of the system Hamiltonian. We assume that all elements of this matrix are real.

2.2 Linear spectroscopy

2.2.1 Linear absorption

For calculations of the linear absorption one has to include the interaction with a time-dependent electric field in the Hamiltonian, which induces the transitions between the ground and excited states:

$$\hat{H}_{\mathrm{SF}} = -\hat{\vec{\mu}} \cdot \vec{E}\,(t) = -\sum_{n}^{N} \left((\vec{\mu}_n \cdot \vec{o})\, E\,(t) \right) \left(\hat{\boldsymbol{e}}_n^{\dagger} \hat{\boldsymbol{h}}_n^{\dagger} + \hat{\boldsymbol{h}}_n \hat{\boldsymbol{e}}_n \right). \tag{2.37}$$

Here $\hat{\vec{\mu}}$ is the electric dipole moment operator, $\vec{\mu}_n$ is the transition dipole vector for pigment n and $\vec{o}$ is the polarization vector of the electric field. For now we disregarded the static dipole moments (the diagonal elements of the dipole operator). Note that the CT states are dark and carry no transition dipole strength. We also define the scalar dipole moment operator $\hat{\mu} = \hat{\vec{\mu}} \cdot \vec{o}$ for later convenience.

Assuming a linearly polarized incoming light, the linear absorption spectrum is calculated as a one-sided Fourier transform of the linear response function [30, 53, 64, 86]:

$$A\,(\omega) = \omega \mathrm{Re} \int_{0}^{\infty} \mathrm{d}t \mathrm{e}^{\mathrm{i}\omega t} \left\langle R^{(1)}\,(t) \right\rangle_{\mathrm{dis}}. \tag{2.38}$$

The linear response function is formally a tensor

$$R^{(1)}\,(t; \vec{o}_2, \vec{o}_1) = \left\langle \mathrm{Tr} \left[\mathrm{e}^{\mathrm{i}\hat{H}t} \left(\hat{\vec{\mu}} \cdot \vec{o}_2 \right) \mathrm{e}^{-\mathrm{i}\hat{H}t} \left(\hat{\vec{\mu}} \cdot \vec{o}_1 \right) \hat{\rho}_{gg} \right] \right\rangle_{\mathrm{or}}. \tag{2.39}$$

Here $\hat{\rho}_{gg} = |g\rangle\langle g| \hat{\rho}_{\mathrm{B}}^{\mathrm{eq}}$ is the ground state equilibrium density operator, $\vec{o}_1$ and $\vec{o}_2$ denote the polarizations of the incoming light and registered signal, and $\langle \bullet \rangle_{\mathrm{or}}$ denotes orientational averaging, which has to be performed for randomly oriented systems. In this expression we have assumed the rotating wave approximation (RWA). For isotropic systems, the tensorial nature of the response function can be neglected and scalar response function can be defined as $R^{(1)}\,(t) = R^{(1)}\,(t; \vec{o}, \vec{o})$, with $\vec{o}$ being an arbitrary polarization vector.

Using the Condon approximation, i. e. assuming that the dipole moment operator is independent of the vibrational degrees of freedom, the response function in the excitonic basis is expanded as

$$R^{(1)}\,(t) = \sum_{e_1, e_2}^{N_{\mathrm{tot}}} \left\langle \mu_{e_1 g} \mu_{e_2 g} \right\rangle_{\mathrm{or}} \mathrm{Tr}_{\mathrm{B}} \left[\mathrm{e}^{\mathrm{i}\hat{H}_{\mathrm{B}} t} \langle e_2 | \mathrm{e}^{-\mathrm{i}\hat{H}t} | e_1 \rangle \hat{\rho}_{\mathrm{B}}^{\mathrm{eq}} \right], \tag{2.40}$$

where we used the fact that for our model $\langle g|e^{i\hat{H}t}|g\rangle = e^{i\hat{H}_B t}$. Here $\mu_{e_1 g} = \langle e_1|\hat{\mu}|g\rangle$ is the excitonic transition dipole moment. For a molecular system oriented randomly in a sample, orientationally averaged transition dipole moments are [109]:

$$\left\langle \mu_{e_1 g}\mu_{e_2 g}\right\rangle_{\text{or}} = \frac{1}{3}\left(\vec{\mu}_{e_1 g}\cdot\vec{\mu}_{e_2 g}\right) \tag{2.41}$$

In the following we use the so-called secular approximation, i. e. we consider only terms, when $e_1 = e_2$. This means that the coherence transfer effects in Eq. (2.40) are neglected.

We need to evaluate the expression

$$\varphi_{e_1}(t) = \text{Tr}_B\left[e^{i\hat{H}_B t}\langle e_1|e^{-i\hat{H}t}|e_1\rangle\hat{\rho}_B^{\text{eq}}\right]. \tag{2.42}$$

This can be performed using the second order cumulant expansion technique [86]. This procedure is described in more detail in Appendix A. We then obtain [**P7**]:

$$\varphi_{e_1}(t) = e^{-i\varepsilon_{e_1}t - g_{e_1}(t) - \xi_{e_1}(t)}. \tag{2.43}$$

Here $g_{e_1}(t) = g_{e_1 e_1, e_1 e_1}(t)$, and the off-diagonal fluctuation term is

$$\xi_{e_1}(t) = \sum_{e_2\neq e_1}^{N_{\text{tot}}}\int_0^t d\tau_2\int_0^{\tau_2} d\tau_1 e^{i\omega_{e_1 e_2}(\tau_2-\tau_1)}C_{e_1 e_2, e_2 e_1}(\tau_2-\tau_1). \tag{2.44}$$

This is the non-Markovian expression, which was originally derived in Ref. [47]. We denote this term as the *complex time-dependent* Redfield (ctR) theory term. It is responsible for the lifetime broadening, though in a more accurate if compared to the phenomenological approaches (see below).

Recently, a similar but slightly more complicated expression was also obtained [45]. In this thesis the second order cumulant expansion was performed for the matrix elements of the operator $\text{Tr}_B\left[e^{i\hat{H}_B t}e^{-i\hat{H}t}\hat{\rho}_B^{\text{eq}}\right]$, while in Ref. [45] it was done for the whole operator. Note that the cumulant expansion is exact for the autocorrelation of the diagonal fluctuations but not for terms involving the off-diagonal fluctuations. This is because the diagonal fluctuations are characterized by a Gaussian process (for harmonic bath) and thus Wick's theorem applies [108], while off-diagonal fluctuations also include excitonic propagators $e^{i\omega_{e_1 e_2}t}$.

Finally, the response function can be expressed as

$$R^{(1)}(t) = \frac{1}{3}\sum_{e_1}^{N_{\text{tot}}}|\vec{\mu}_{e_1 g}|^2 e^{-i\varepsilon_{e_1}t - g_{e_1 e_1, e_1 e_1}(t) - \xi_{e_1}(t)}. \tag{2.45}$$

Application of the Markovian approximation can be used for the off-diagonal fluctuation term, and the resulting expression is

$$\xi_{e_1}^{\mathrm{M}}(t) = \sum_{e_2 \neq e_1}^{N_{\mathrm{tot}}} t \int_0^\infty \mathrm{d}\tau_1 \mathrm{e}^{\mathrm{i}\omega_{e_1e_2}\tau_1} C_{e_1e_2,e_2e_1}(\tau_1)\,. \tag{2.46}$$

This level of theory (denoted by us as the *complex* Redfield (cR) theory) was extensively used in previous studies [47, 110–112].

In a phenomenological way, the off-diagonal fluctuations are assumed to induce the lifetime broadening, which can be expressed as

$$\xi_{e_1}^{\mathrm{LB}}(t) = \frac{t}{2\tau_{e_1}}. \tag{2.47}$$

The excited state lifetime τ_{e_1} can be calculated from the transfer rates as

$$\frac{1}{\tau_{e_1}} = \sum_{e_2 \neq e_1}^{N_{\mathrm{tot}}} K_{e_2e_1}. \tag{2.48}$$

Either the standard Redfield (sR) theory transfer rates [30, 90]

$$\begin{aligned} K_{e_2e_1}^{\mathrm{sR}} &= 2\mathrm{Re} \int_0^\infty \mathrm{d}\tau_1 \mathrm{e}^{\mathrm{i}\omega_{e_1e_2}\tau_1} C_{e_1e_2,e_2e_1}(\tau_1) \\ &= \left(1 + \coth\left(\frac{\beta\omega_{e_1e_2}}{2}\right)\right) C''_{e_1e_2,e_2e_1}\left(\omega_{e_1e_2}\right) \end{aligned} \tag{2.49}$$

or those of the modified Redfield (mR) theory [90, 113]

$$\begin{aligned} K_{e_2e_1}^{\mathrm{mR}} = 2\mathrm{Re} \int_0^\infty \mathrm{d}t \mathrm{e}^{\mathrm{i}\omega_{e_1e_2}t} \exp\Big\{ &- g_{e_2e_2,e_2e_2}(t) - g_{e_1e_1,e_1e_1}(t) + g_{e_1e_1,e_2e_2}(t) \\ &+ g_{e_2e_2,e_1e_1}(t) - 2\mathrm{i}\left(\lambda_{e_1e_1,e_1e_1} - \lambda_{e_2e_2,e_1e_1}\right) t \Big\} \\ \times \Big\{ &C_{e_2e_1,e_1e_2}(t) - \left[\dot{g}_{e_1e_2,e_2e_2}(t) - \dot{g}_{e_1e_2,e_1e_1}(t) - 2\mathrm{i}\lambda_{e_1e_2,e_1e_1}\right] \\ &\times \left[\dot{g}_{e_2e_2,e_2e_1}(t) - \dot{g}_{e_1e_1,e_2e_1}(t) - 2\mathrm{i}\lambda_{e_2e_1,e_1e_1}\right] \Big\} \end{aligned} \tag{2.50}$$

have been used [46, 49, 114]. Here dot denotes the time derivative and

$$\lambda_{e_1e_2,e_3e_4} = \frac{1}{\pi} \int_0^\infty \mathrm{d}\omega \frac{C''_{e_1e_2,e_3e_4}(\omega)}{\omega} \tag{2.51}$$

is the reorganization energy in the excitonic basis. We note that taking only the real part of Eq. (2.46) results in accounting of the off-diagonal fluctuations by the

sR theory lifetimes with Eqs. (2.47)−(2.49). To obtain the equivalent expression with the mR lifetimes a slightly different derivation and more approximations must be used [49]. The sR and mR theories thus simply account for the lifetime broadening as in Eq. (2.47) with Eqs. (2.49) and (2.50), respectively. Note that these names are here used only in the context of describing off-diagonal fluctuations. Formally, using the Redfield theory for calculations of the absorption lineshape requires to solve the time local quantum master equation and the modified Redfield theory was originally developed to describe only population transfer [90, 113].

2.2.2 Linear dichroism

Linear dichroism (LD) spectroscopy is performed on oriented samples (they are no longer isotropic). For simplicity we orient the molecular coordinate system in such a way that the membrane normal lies along the z axis. The LD spectrum then corresponds to a difference between two absorption measurements: one where the incoming light is polarized parallel to the membrane plane, the other, when the incoming light is polarized perpendicular to the membrane plane [115]:

$$LD\left(\omega\right) = A_{\parallel}\left(\omega\right) - A_{\perp}\left(\omega\right). \tag{2.52}$$

The required absorption spectra are then defined by

$$A_{\parallel/\perp}\left(\omega\right) = \omega \mathrm{Re} \int_{0}^{\infty} \mathrm{d}t \mathrm{e}^{\mathrm{i}\omega t} \left\langle R^{(1)}\left(t; \vec{o}_{\parallel/\perp}, \vec{o}_{\parallel/\perp}\right)\right\rangle_{\mathrm{dis}}. \tag{2.53}$$

The response functions are calculated using the same approximations as above. The relevant orientational average is

$$\left\langle \left(\vec{\mu}_{e_1 g} \cdot \vec{o}_{\parallel}\right)^2 - \left(\vec{\mu}_{e_1 g} \cdot \vec{o}_{\perp}\right)^2 \right\rangle_{\mathrm{or}} \propto \mu^2_{e_1 g,x} + \mu^2_{e_1 g,y} - 2\mu^2_{e_1 g,z}. \tag{2.54}$$

Finally, the LD spectrum can be calculated as

$$LD\left(\omega\right) = \omega \mathrm{Re} \int_{0}^{\infty} \mathrm{d}t \mathrm{e}^{\mathrm{i}\omega t} \left\langle R^{(1)}_{\mathrm{LD}}\left(t\right)\right\rangle_{\mathrm{dis}}, \tag{2.55}$$

with

$$R^{(1)}_{\mathrm{LD}}\left(t\right) = \sum_{e_1}^{N_{\mathrm{tot}}} \left(\mu^2_{e_1 g,x} + \mu^2_{e_1 g,y} - 2\mu^2_{e_1 g,z}\right) \exp\left(-\mathrm{i}\varepsilon_{e_1} t - g_{e_1}\left(t\right) - \xi_{e_1}\left(t\right)\right). \tag{2.56}$$

2.2.3 Circular dichroism

The circular dichroism (CD) spectrum is defined as a difference between the absorption of left and right polarized light [25, 115, 116]:

$$CD\left(\omega\right) = A_{\mathrm{L}}\left(\omega\right) - A_{\mathrm{R}}\left(\omega\right). \tag{2.57}$$

To properly describe the CD spectrum, one has to take into account the coupling with the magnetic field. Therefore, in this case the system–field coupling Hamiltonian is

$$\begin{aligned}\hat{H}_{\mathrm{SF}} &= -\hat{\vec{\mu}}\cdot\vec{E}\left(t\right) - \hat{\vec{m}}\cdot\vec{B}\left(t\right)\\ &= -\sum_{n}^{N} E\left(t\right)\left(\vec{\mu}_n\cdot\vec{o}_E\right)\left(\hat{\boldsymbol{e}}_n^{\dagger}\hat{\boldsymbol{h}}_n^{\dagger} + \hat{\boldsymbol{h}}_n\hat{\boldsymbol{e}}_n\right)\\ &\quad -\sum_{n}^{N} B\left(t\right)\left(\left(\vec{m}_n\cdot\vec{o}_B\right)\hat{\boldsymbol{e}}_n^{\dagger}\hat{\boldsymbol{h}}_n^{\dagger} + \left(\vec{m}_n^{*}\cdot\vec{o}_B\right)\hat{\boldsymbol{h}}_n\hat{\boldsymbol{e}}_n\right).\end{aligned} \tag{2.58}$$

Here $\hat{\vec{m}}$ is the magnetic dipole moment operator and $\vec{o}_B$ is the polarization vector of the magnetic field. Following Ref. [53], we use an effective molecular magnetic dipole moment defined as

$$\vec{m}_n = \frac{\mathrm{i}}{2}\varepsilon_{n^*}\left[\vec{R}_n\times\vec{\mu}_n\right]. \tag{2.59}$$

Here $\vec{R}_n$ is the position vector corresponding to the center of the pigment n. The CD spectrum can also be calculated from the response function:

$$CD\left(\omega\right) = \omega\mathrm{Im}\int_0^{\infty}\mathrm{d}t\mathrm{e}^{\mathrm{i}\omega t}\left\langle R_{\mathrm{CD}}^{(1)}\left(t\right)\right\rangle_{\mathrm{dis}}. \tag{2.60}$$

The relevant response function is found to be [53]:

$$R_{\mathrm{CD}}^{(1)}\left(t;\vec{o}_2,\vec{o}_1\right) = \left\langle\mathrm{Tr}\left[\mathrm{e}^{\mathrm{i}\hat{H}t}\left(\hat{\vec{\mu}}\cdot\vec{o}_2\right)\mathrm{e}^{-\mathrm{i}\hat{H}t}\left(\hat{\vec{m}}\cdot\vec{o}_1\right)\hat{\rho}_{gg}\right]\right\rangle_{\mathrm{or}}. \tag{2.61}$$

For isotropic medium, we can again set $R_{\mathrm{CD}}^{(1)}\left(t\right) = R_{\mathrm{CD}}^{(1)}\left(t;\vec{o},\vec{o}\right)$, though note that the same vector $\vec{o}$ is taken as both arguments. Using the same level of theory as above, the response function is:

$$R_{\mathrm{CD}}^{(1)}\left(t\right) = \frac{1}{3}\sum_{e_1}^{N_{\mathrm{tot}}}\left(\vec{\mu}_{e_1g}\cdot\vec{m}_{e_1g}\right)\exp\left(-\mathrm{i}\varepsilon_{e_1}t - g_{e_1}\left(t\right) - \xi_{e_1}\left(t\right)\right). \tag{2.62}$$

Here $\vec{m}_{e_1g} = \langle e_1|\hat{\vec{m}}|g\rangle$ is the excitonic magnetic dipole moment.

We note that this level of theory neglects the intrinsic CD of the pigments. In addition, the CD spectra can be affected by couplings to the higher energy states [25, 117], which we ignore in the present treatment.

2.3 Calculations of linear absorption of molecular dimer

In this section we compare the ctR theory and other approaches described in Section 2.2.1 by calculating the absorption lineshapes for a simple dimer system [**P7**]. Here all the calculations are of the absorption lineshapes (not spectra), thus factor ω in Eq. (2.38) is not included. For benchmark calculations of the absorption lineshape we used an exact HEOM (hierarchical equations of motion) method as described in Ref. [44].

The system Hamiltonian of the dimer under consideration is given by

$$\hat{H}_{\mathrm{S}} = \begin{pmatrix} \tilde{\varepsilon} + \Delta & J \\ J & \tilde{\varepsilon} \end{pmatrix}. \tag{2.63}$$

We set the molecular transition dipole moments to be of the same length and perpendicular to each other, to avoid coherence transfer effects. Then the secular approximation is valid.

For simplicity, we assume that fluctuations for both sites are described by the same Debye spectral density:

$$C''(\omega) = \frac{2\lambda\gamma\omega}{\omega^2 + \gamma^2}. \tag{2.64}$$

Here, λ is the reorganization energy and γ is the bath relaxation rate. For numerical calculations, we expanded the resulting correlation functions in terms of exponentials using the $[K - 1/K]$ Padé approximant [118].

Our system under consideration is completely characterized by 5 parameters: the difference between site energies Δ, the resonance coupling J, the reorganization energy λ, the bath relaxation rate γ and the temperature T (we set the overall energy shift $\tilde{\varepsilon}$ to 15000 cm^{-1}). We investigate the absorption lineshape dependence on all these parameters in turn, holding the others constant. The fixed parameters for our investigations are $\Delta = 100\,\mathrm{cm}^{-1}$, $J = 100\,\mathrm{cm}^{-1}$, $\lambda = 50\,\mathrm{cm}^{-1}$, $\gamma^{-1} = 50\,\mathrm{fs}$, $T = 77\,\mathrm{K}$. These are typical values for the realistic photosynthetic complexes [25].

To describe the quality of the approximate methods, we use a simple quality parameter – the intersection area of the lineshape obtained from an approximate method with that from HEOM divided by the union area of the said lineshapes:

$$Q = \frac{\int_{-\infty}^{\infty} \mathrm{d}\omega \left(A^{\mathrm{HEOM}}(\omega) \cap A^{\mathrm{approximate}}(\omega) \right)}{\int_{-\infty}^{\infty} \mathrm{d}\omega \left(A^{\mathrm{HEOM}}(\omega) \cup A^{\mathrm{approximate}}(\omega) \right)}. \tag{2.65}$$

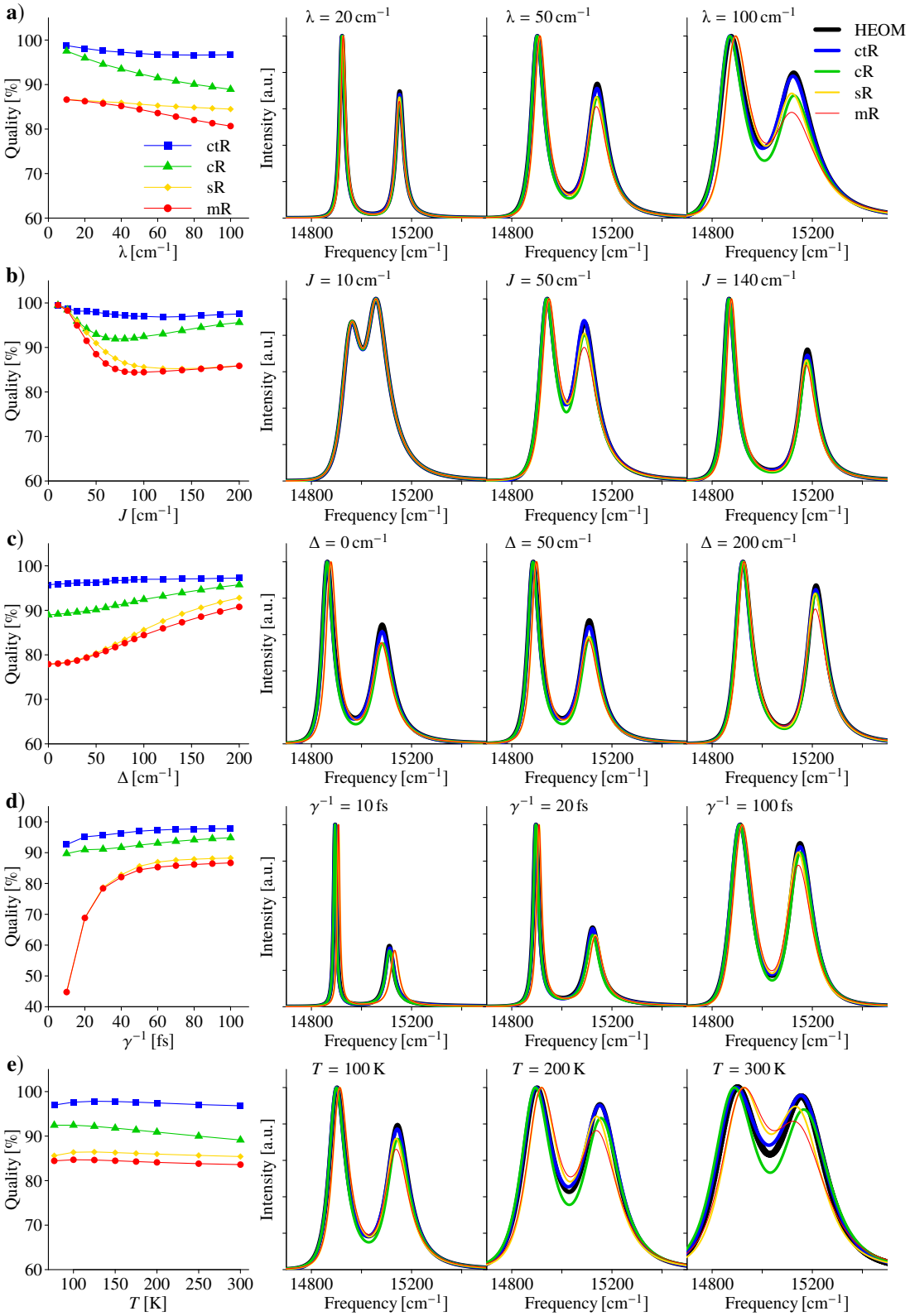

Figure 2.1: Quality of the approximate methods (left) and the absorption lineshapes (right) in dependence on: a) reorganization energy λ; b) resonance coupling J; c) difference between site energies Δ; d) bath relaxation rate γ; e) temperature T. Other parameters are listed in the text.

This parameter is equal to 100 % when the lineshapes perfectly match, and decreases, when they begin to differ. Q value of 0 % means no overlap between the lineshapes. Note that we normalize every lineshape to its maximum value.

First, we analyze the absorption lineshape dependence on the reorganization energy – in Fig. 2.1a we plot the quality of the approximate methods and the lineshapes for a few reorganization energy values. To remain in the regime where the approximate methods are expected to perform adequately, we limit the reorganization energies to the value of the resonance coupling, when $\lambda < J$. Other parameters are set to their fixed values. The ctR theory shows very good agreement for all considered λ values. The quality of the cR theory decreases with increasing λ, but is still considerably better than using either the sR or mR approaches, that give deviations of peak positions for larger reorganization energies. While the mR theory is close to the sR theory for small reorganization energies, it falls off rapidly with increasing λ.

Now we turn to the absorption lineshape dependence on the resonance coupling J (see Fig. 2.1b). For small J values, corresponding to localized excitations, all theories give good description of the lineshape, but only the ctR theory remains good elsewhere. The agreement between HEOM and other theories worsens with increasing J, though the cR theory performs considerably better than simple lifetime theories. Overall, the mR theory gives the worst agreement with HEOM. It should also be noted that the quality of approximate methods becomes better for large J values, and this improvement is the most dramatic for the cR theory.

The absorption lineshape dependence on the site energy difference Δ is shown in Fig. 2.1c. The ctR theory gives good results for all Δ values. The cR theory performs slightly worse, while the sR and mR theories are even worse. These theories show better agreement with HEOM as Δ increases, going from delocalized to localized excitations.

Next we consider the influence of the bath relaxation rate γ (see Fig. 2.1d). For slow baths, the quality of approximate methods is mostly constant, but it deteriorates for Markovian baths. This is especially noticeable for the sR and mR theories. As can be seen from the given absorption lineshapes for $\gamma^{-1} = 10\,\mathrm{fs}$, these theories fail to capture correct peak positions. This results in low Q values, despite that obtained peak amplitudes and linewidths are adequate.

The absorption lineshape dependence on temperature is given in Fig. 2.1e. Even though the change of temperature strongly influences the lineshapes, the quality of the approximate methods remains mostly the same for the consid-

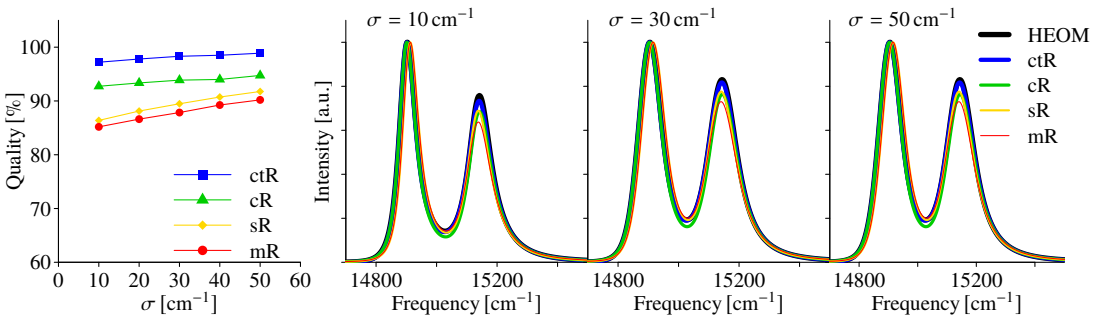

Figure 2.2: Quality of the approximate methods (left) and the absorption lineshape (right) in dependence on disorder standard deviation σ. Other parameters are set to fixed values (see text).

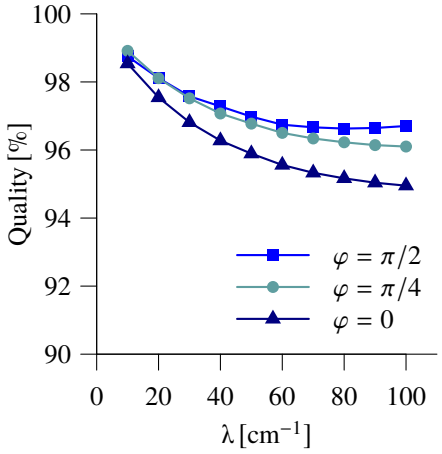

Figure 2.3: Dependence of the quality of the absorption spectrum using the ctR theory on the reorganization energy λ for several angles φ between the transition dipole moments. Other parameters are set to fixed values (see text).

ered T range. For these parameters, the ctR theory gives results very close to the HEOM, the cR theory is somewhat worse, the sR theory is still worse and the mR theory is the worst of all considered theories. An interesting feature is that the sR and mR theories give smaller gap between the peaks with increasing temperature. This might seem surprising as these theories do not include the imaginary part of the off-diagonal fluctuation term. However, from the analysis of contributions of separate excitonic transitions (see supplementary material of Ref. [**P7**]) it becomes apparent that the decreasing gap is a result of the increasing overlap between the peaks due to the lifetime broadening term.

We also investigated the absorption lineshape dependence on the diagonal disorder, which is characterized by the standard deviation of the excited state energies σ. These results are shown in Fig. 2.2. The ctR theory again gives very

good agreement with the HEOM lineshapes, and the other theories are worse, with the cR being considerably better than both sR and mR theories. While the quality of the ctR theory remains more or less constant, other theories give better results with increasing σ, but the increase of quality is not dramatic.

All the preceding calculations were made by considering a dimer with perpendicular transition dipole moments of equal length. To investigate how the coherence transfer contribution affects the absorption lineshape, we also calculated the quality parameter dependence on the reorganization energy for angles between the transition dipole moments equal to 0, $\pi/4$ (coherence transfer present) and $\pi/2$ (no coherence transfer, as before). Calculations were performed using the ctR theory. These results are plotted in Fig. 2.3. The ctR theory gives good agreement with exact lineshapes even for non-perpendicular transition dipole moments. This implies that non-secular contributions are relatively minor for the considered parameter range.

Our calculations clearly show that application of the ctR theory gives the best lineshape compared to the exact HEOM method. This theory results in an expression that is complex and time dependent. Our results demonstrate that both of these two features are important in order to accurately calculate the absorption lineshape. Since the linear response function (Eq. (2.45)) is rapidly decaying due to the presence of the lineshape function in the exponential, it is important to accurately describe the short time effects of the off-diagonal fluctuations. Application of the Markovian approximation means that the information about the short time dynamics is lost. Therefore, the cR theory, used extensively [47, 110–112, 117, 119], gives worse agreement with exact lineshapes.

On the other hand, inclusion of the imaginary part is also very important – our results demonstrate that using only real valued expressions for the off-diagonal fluctuations results in considerably worse quality of the absorption lineshape. Lack of the imaginary part means that some part of the frequency shift due to interaction with the bath is not accounted for, thus using the sR and mR expressions for lifetime broadening gives incorrect peak positions. Note that this *cannot* be corrected by a common frequency shift, as different excitonic transitions experience different shifts, which is most obviously seen in the absorption spectra at 300 K shown in Fig. 2.1e.

Here we considered the Debye spectral density, which might not be suitable to describe low temperature experiments [80]. It was chosen because the solutions can be readily compared to the exact HEOM method, which has problems incorporating more structured spectral densities. Nonetheless, all expressions

required for the application of the ctR theory (Eq. (2.44)) can be calculated by straightforward numerical methods for arbitrary spectral densities. Moreover, when the bath correlation function can be expressed as a sum of exponentials (which is the case for a variety of spectral densities [120]), the integrals of the ctR theory can be calculated analytically. Thus, the speed of numerical calculations can be improved substantially.

Even though we performed simulations only for a dimer, our conclusions remain valid for bigger systems. In our view, the ctR theory should be considered for simulations of larger aggregates, if an exact method is not available or too expensive computationally. Its application to the PSII RC is presented in Chapter 3. We note that a very similar approach to the ctR was recently proposed [45]. It does not invoke the secular approximation, thus can include coherence transfer effects. Nonetheless, this approach scales with the system size worse than the ctR, because the numerical evaluation of an exponent of an operator is required. Therefore, we suggest the ctR theory as the most practical approach, since our calculations show that the coherence transfer effects are not very important when calculating the absorption spectra.

In another recent study, an approach based on a systematic perturbative treatment of the off-diagonal fluctuations was proposed [53]. Application of the secular and Markovian approximations gave expressions corresponding to the cR theory. In addition, the first order correction was also incorporated, which accounted for the coherence transfer effects, that were shown to give only minor contributions to the absorption lineshape. The authors concluded that the secular approximation combined with the Markovian approximation for the off-diagonal fluctuations is a sufficient level of theory by describing the absorption lineshapes. While our results confirm the validity of the secular approximation in the limit of relatively weak system–bath coupling, they show that the application of the Markovian approximation (going from ctR to cR theory) gives somewhat worse results. Nonetheless, the non-secular corrections proposed in [53] can be used together with ctR theory to yield even closer results to the exact lineshapes.

A very important finding is that using the mR lifetimes to account for the off-diagonal fluctuations gives the worst results of all the approximate theories considered. Thus, the question whether the sR or the mR theory provides more accurate description of the lifetime broadening [53], can now conclusively be answered in favor of the former. This might be surprising, as in deriving the mR transfer rates only the off-diagonal fluctuations are taken as a perturbation,

instead of the full system–bath coupling Hamiltonian as in the sR theory [90, 113]. It was also shown that the mR theory is able to reproduce the results of the Förster theory in the localized excitation limit [90]. Recently the mR theory was further extended to include coherent dynamics [121, 122]. Thus it is superior to the sR theory for the energy transfer calculations. Nonetheless, the calculation of absorption lineshapes is a somewhat different problem. The usage of the mR lifetimes for the absorption lineshapes was already examined in detail [49]. It was shown that a number of approximations are needed to obtain the response function expression with the mR lifetimes. Besides the Markovian approximation and neglect of the imaginary part, both of which we showed to contribute significantly to the reproduction of the exact lineshape, two more approximations are needed. First (i) requires setting $\mathrm{e}^{\mathrm{i}\hat{H}_\mathrm{B}t}\mathrm{e}^{-\mathrm{i}\left(\hat{H}_\mathrm{B}+\hat{F}_{ee}\right)t} \approx \hat{I}_\mathrm{B}$. Another (ii) requires substituting $\hat{\rho}_e^{\mathrm{eq}} = \exp\left(-\beta\left(\hat{H}_\mathrm{B}+\hat{F}_{ee}\right)\right)/\mathrm{Tr}\left(\exp\left(-\beta\left(\hat{H}_\mathrm{B}+\hat{F}_{ee}\right)\right)\right)$ instead of $\hat{\rho}_\mathrm{B}^{\mathrm{eq}}$. Both of these approximations are valid only for small diagonal fluctuations (they can be regarded as zero order approximations) and are against the spirit of the original mR theory [113]. An improved version of the mR theory for optical lineshapes was developed recently [123], which corrected some of the shortcomings of the original approach.

It should be emphasized, however, that the major source of error in using the mR lifetimes for absorption lineshape calculations comes from the phenomenological way of using the lifetimes, i. e. neglect of the imaginary part and the Markovian approximation. This is why the mR theory gives close results to the sR theory for smaller values of system–bath coupling. However, as its strength increases, the quality of the mR theory worsens even compared to the sR theory (see Fig. 2.1a)) due to approximations (i) and (ii). This is different from what one may expect, as in energy transfer problems mR theory can handle stronger system–bath couplings than the sR theory. Therefore, we emphasize that usage of the mR transfer rates for absorption calculations does not improve over the sR rates and should be avoided.

The mR transfer lifetimes were used to account for the off-diagonal fluctuations in a number of studies of optical spectra of photosynthetic complexes: the LHCII of higher plants [114, 124], the light-harvesting complex 2 of purple bacteria [125–129], the PSII RC [**P2**, 101, 105, 106, 130] and other systems [131]. Often, system parameters were obtained from fitting the optical spectra. However, as we have demonstrated, the applicability of the mR lifetimes to the optical spectra is severely limited. As an example, consider a comparison of the absorption spectra of the PSII RC (see Fig. 2.4) calculated using both ctR

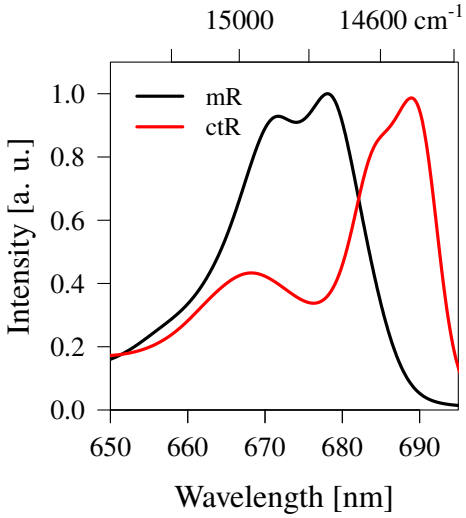

Figure 2.4: Comparison of the PSII RC absorption spectra at 77 K calculated using model parameters from [**P2**] and mR or ctR theories.

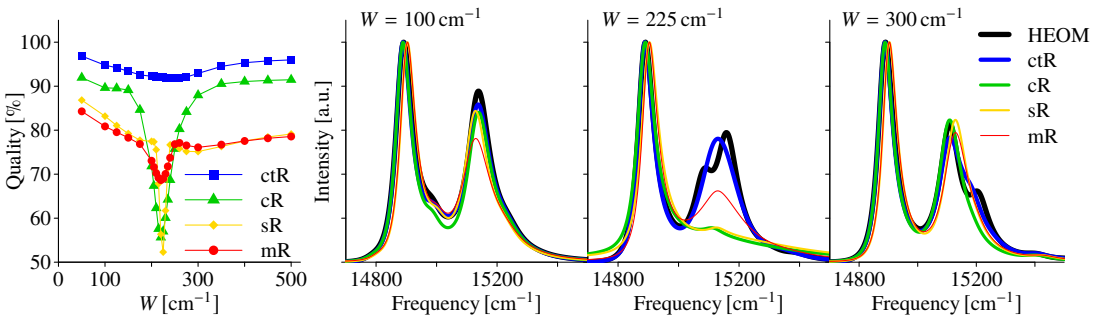

Figure 2.5: Quality of approximate methods (left) and absorption lineshape (right) in dependence on the frequency of vibrational mode W. Other parameters of the vibrational mode are $\lambda_d = 15\,\mathrm{cm}^{-1}$, $\Gamma^{-1} = 500\,\mathrm{fs}$, and all others are set to fixed values (see text).

and mR theories and the *same* parameters from Ref. [**P2**], where mR theory was used to fit the experimental spectrum. As can be seen, huge differences between two theories are obtained, considerably more so than could be expected. Thus, we can conclude that the parameters obtained from the fitting might be misestimated due to inadequate theory and should be revised. This is done for the PSII RC in Chapter 3.

Recently, a number of studies were made about the treatment of specific vibrational modes, which are coupled to the electronic degrees of freedom [132–134]. They can be included by adding damped vibrational modes to the spectral density. However, this should create problems for perturbative methods, especially in the vicinity of resonance (between electronic and vibrational levels) conditions. We have analyzed this by including one damped vibration to the

spectral density:

$$C_{\mathrm{d}}''(\omega) = \frac{2\lambda_{\mathrm{d}}\omega W^2\Gamma}{\left(\omega^2 - W^2\right)^2 + \Gamma^2\omega^2}. \tag{2.66}$$

We chose parameters $\lambda_{\mathrm{d}} = 15\,\mathrm{cm}^{-1}$ and $\Gamma^{-1} = 500\,\mathrm{fs}$. In Fig. 2.5 we plot the quality of the approximate methods and the absorption lineshape dependence on the frequency of vibrational mode W. Other dimer parameters are the same as before. For this system the excitonic energy splitting is $\approx 224\,\mathrm{cm}^{-1}$. We can see that in near resonance conditions, all methods diverge from the HEOM lineshapes. The ctR theory remains qualitatively good, but no longer quantitatively good. On the other hand, the quality of the other methods worsens substantially. Clearly, in this regime the Markovian approximation completely breaks down. If correlation function possesses oscillatory term $\approx \omega_{e_1e_2}$, then the integrand in Eq. (2.44) is no longer highly oscillating and its value increases considerably. Then the second order perturbation theory is no longer valid. While the ctR theory still manages to correctly capture the short time behavior of the response function, Markovian theories fail to do that. Thus, in quantitative studies, the vibrational degrees of freedom in near resonance conditions should either be treated exactly via non-perturbative methods like the HEOM, or explicitly as recently described [134]. The ctR theory can be used when vibrations are off-resonant, or perhaps even in resonant conditions if the qualitative result is sufficient.

2.4 Stark spectroscopy

Stark spectroscopy relies on the effect of an applied static electric field on an absorption spectrum and is defined as the difference between the spectrum with the field on and the field off [135]:

$$S(\omega) = A_{\mathcal{E}}(\omega) - A(\omega). \tag{2.67}$$

Theoretically, the key issue is to calculate the absorption spectrum with a presence of the electric field. For this, the system–field Hamiltonian is extended to also include the static field:

$$\hat{H}_{\mathrm{SF}} = -\hat{\vec{\mu}} \cdot \left(\vec{E}(t) + \vec{\mathcal{E}}\right). \tag{2.68}$$

Here the static electric field is denoted by $\vec{\mathcal{E}}$, and we assume that the electric dipole operator $\hat{\vec{\mu}}$ stays constant even in the presence of the electric field – therefore we are describing only the linear Stark effect. The term $-\hat{\vec{\mu}} \cdot \vec{\mathcal{E}}$ can be added

to the system Hamiltonian, because it is constant. Here we can no longer neglect the diagonal elements of the dipole moment operator. In fact, they cause a shift in the excited state energies:

$$\langle A| \left(\hat{H}_\mathrm{S} - \hat{\vec{\mu}} \cdot \vec{\mathcal{E}}\right) |A\rangle - \langle g| \left(-\hat{\vec{\mu}} \cdot \vec{\mathcal{E}}\right) |g\rangle = \varepsilon_A - \Delta\vec{\mu}_A \cdot \vec{\mathcal{E}}. \tag{2.69}$$

Here,

$$\Delta\vec{\mu}_A = \langle A|\hat{\vec{\mu}}|A\rangle - \langle g|\hat{\vec{\mu}}|g\rangle \tag{2.70}$$

is the difference between the dipole moments of the excited and the ground states and will be called the static dipole moment for convenience. We have to subtract the ground state energy, because we have set it to zero. Thus, for simplicity, we redefine the dipole moment operator:

$$\hat{\vec{\mu}} \to \hat{\vec{\mu}} - \hat{I}\langle g|\hat{\vec{\mu}}|g\rangle. \tag{2.71}$$

In this work we follow [136] and use perturbation theory to calculate the Stark spectrum. To this end, we first write the expression for the linear response function in the presence of the static electric field:

$$\begin{aligned} R_{\mathcal{E}}^{(1)}(t;\vec{o}_2,\vec{o}_1;\vec{o}_{\mathcal{E}}) = \\ &\left\langle \mathrm{Tr}\left[\mathrm{e}^{\mathrm{i}\left(\hat{H}-\left(\hat{\vec{\mu}}\cdot\vec{o}_{\mathcal{E}}\right)\mathcal{E}\right)t} \left(\hat{\vec{\mu}}\cdot\vec{o}_2\right) \mathrm{e}^{-\mathrm{i}\left(\hat{H}-\left(\hat{\vec{\mu}}\cdot\vec{o}_{\mathcal{E}}\right)\mathcal{E}\right)t} \left(\hat{\vec{\mu}}\cdot\vec{o}_1\right) \hat{\rho}_{gg} \right] \right\rangle_{\mathrm{or}} \\ = &\left\langle \mathrm{Tr}\left[\exp_-\left(-\mathrm{i}\int_0^t \mathrm{d}\tau \left(\hat{\vec{\mu}}^{\mathrm{I}}(\tau)\cdot\vec{o}_{\mathcal{E}}\right)\mathcal{E} \right) \mathrm{e}^{\mathrm{i}\hat{H}t} \left(\hat{\vec{\mu}}\cdot\vec{o}_2\right) \right.\right. \\ &\left.\left. \times \mathrm{e}^{-\mathrm{i}\hat{H}t} \exp_+\left(\mathrm{i}\int_0^t \mathrm{d}\tau \left(\hat{\vec{\mu}}^{\mathrm{I}}(\tau)\cdot\vec{o}_{\mathcal{E}}\right)\mathcal{E} \right) \left(\hat{\vec{\mu}}\cdot\vec{o}_1\right) \hat{\rho}_{gg} \right] \right\rangle_{\mathrm{or}}. \end{aligned} \tag{2.72}$$

Here $\vec{o}_{\mathcal{E}}$ is the polarization vector of the static electric field, and $\mathcal{E}$ is its magnitude. If we expand this expression in powers of $\mathcal{E}$ (this is done by expanding the time-ordered exponentials and collecting the terms), then the zeroth order term gives the usual absorption spectrum, the first order term vanishes for isotropic samples, and the second order term is responsible for the Stark signal.

Thus, the Stark spectrum response function is

$$R_S^{(3)}(t;\vec{o}_E;\vec{o}_{\mathcal{E}}) =$$

$$
\begin{aligned}
&- \mathcal{E}^2 \int_0^t \mathrm{d}\tau_2 \int_0^{\tau_2} \mathrm{d}\tau_1 \left\langle \mathrm{Tr}\left[\hat{\mu}^{\mathrm{I}}_{\mathcal{E}}(\tau_1)\,\hat{\mu}^{\mathrm{I}}_{\mathcal{E}}(\tau_2)\,\mathrm{e}^{\mathrm{i}\hat{H}t}\hat{\mu}_E\mathrm{e}^{-\mathrm{i}\hat{H}t}\hat{\mu}_E\hat{\rho}_{gg}\right]\right\rangle_{\mathrm{or}} \\
&- \mathcal{E}^2 \int_0^t \mathrm{d}\tau \int_0^t \mathrm{d}\tau' \left\langle \mathrm{Tr}\left[\hat{\mu}^{\mathrm{I}}_{\mathcal{E}}(\tau)\,\mathrm{e}^{\mathrm{i}\hat{H}t}\hat{\mu}_E\mathrm{e}^{-\mathrm{i}\hat{H}t}\hat{\mu}^{\mathrm{I}}_{\mathcal{E}}(\tau')\,\hat{\mu}_E\hat{\rho}_{gg}\right]\right\rangle_{\mathrm{or}} \\
&- \mathcal{E}^2 \int_0^t \mathrm{d}\tau_2 \int_0^{\tau_2} \mathrm{d}\tau_1 \left\langle \mathrm{Tr}\left[\mathrm{e}^{\mathrm{i}\hat{H}t}\hat{\mu}_E\mathrm{e}^{-\mathrm{i}\hat{H}t}\hat{\mu}^{\mathrm{I}}_{\mathcal{E}}(\tau_2)\,\hat{\mu}^{\mathrm{I}}_{\mathcal{E}}(\tau_1)\,\hat{\mu}_E\hat{\rho}_{gg}\right]\right\rangle_{\mathrm{or}}. \qquad (2.73)
\end{aligned}
$$

Here we have set $\vec{o}_1 = \vec{o}_2 = \vec{o}_E$. Expansion of these three terms in the eigenstate basis of the system Hamiltonian produces many contributions to the Stark spectrum. Nonetheless, the majority of them are non-resonant, i. e. oscillating with factors other than $\mathrm{e}^{-\mathrm{i}\bar{\omega}_e t}$, $\bar{\omega}_e$ being the band gap between the ground and the single-excited state manifolds. In fact, only a single contribution survives the the RWA (this limit was denoted as pure RWA in Ref. [106]):

$$
\begin{aligned}
R^{(3)}_S(t;\vec{o}_E;\vec{o}_{\mathcal{E}}) = -\mathcal{E}^2 \int_0^t \mathrm{d}\tau_2 \int_0^{\tau_2} \mathrm{d}\tau_1 \sum_{e_3}^{N_{\mathrm{tot}}} \sum_{e_2}^{N_{\mathrm{tot}}} \sum_{e_1}^{N_{\mathrm{tot}}} \left\langle \mu^E_{ge_3}\mu^{\mathcal{E}}_{e_3e_2}\mu^{\mathcal{E}}_{e_2e_1}\mu^E_{e_1g}\right\rangle_{\mathrm{or}} \\
\times \mathrm{Tr}_{\mathrm{B}}\left[\mathrm{e}^{\mathrm{i}\hat{H}_{\mathrm{B}}t}\langle e_3|\mathrm{e}^{-\mathrm{i}\hat{H}(t-\tau_2)}|e_3\rangle\langle e_2|\mathrm{e}^{-\mathrm{i}\hat{H}(\tau_2-\tau_1)}|e_2\rangle\langle e_1|\mathrm{e}^{-\mathrm{i}\hat{H}\tau_1}|e_1\rangle\hat{\rho}_{gg}\right]. \qquad (2.74)
\end{aligned}
$$

Here we have denoted $\mu^{E/\mathcal{E}}_{ab} = \langle a|\left(\hat{\vec{\mu}}\cdot\vec{o}_{E/\mathcal{E}}\right)|b\rangle$. Then, using the secular approximation and performing the second order cumulant expansion (see Appendix A) we obtain the following expression, which includes the ctR theory terms to describe the off-diagonal fluctuations:

$$
\begin{aligned}
R^{(3)}_S(t;\vec{o}_E;\vec{o}_{\mathcal{E}}) = -\mathcal{E}^2 \int_0^t \mathrm{d}\tau_2 \int_0^{\tau_2} \mathrm{d}\tau_1 \sum_{e_3}^{N_{\mathrm{tot}}} \sum_{e_2}^{N_{\mathrm{tot}}} \sum_{e_1}^{N_{\mathrm{tot}}} \left\langle \mu^E_{ge_3}\mu^{\mathcal{E}}_{e_3e_2}\mu^{\mathcal{E}}_{e_2e_1}\mu^E_{e_1g}\right\rangle_{\mathrm{or}} \\
\times \exp\left(-\mathrm{i}\left(\omega_{e_3g}t + \omega_{e_2e_3}\tau_2 + \omega_{e_1e_2}\tau_1\right)\right) \\
\times \exp\Big\{ - g_{e_1e_1,e_1e_1}(\tau_1) - \xi_{e_1}(\tau_1) + g_{e_2e_2,e_1e_1}(\tau_1) + g_{e_2e_2,e_1e_1}(\tau_2-\tau_1) \\
- g_{e_2e_2,e_1e_1}(\tau_2) - g_{e_2e_2,e_2e_2}(\tau_2-\tau_1) - \xi_{e_2}(\tau_2-\tau_1) \\
- g_{e_3e_3,e_1e_1}(\tau_2-\tau_1) + g_{e_3e_3,e_1e_1}(\tau_2) + g_{e_3e_3,e_1e_1}(t-\tau_1) \\
- g_{e_3e_3,e_1e_1}(t) + g_{e_3e_3,e_2e_2}(\tau_2-\tau_1) + g_{e_3e_3,e_2e_2}(t-\tau_2) \\
- g_{e_3e_3,e_2e_2}(t-\tau_1) - g_{e_3e_3,e_3e_3}(t-\tau_2) - \xi_{e_3}(t-\tau_2)\Big\}. \qquad (2.75)
\end{aligned}
$$

If we assume magic angle $\left(\cos\left(\theta_{\text{m. a.}}\right) = 1/\sqrt{3}\right)$ between the static and probing electric fields, then the orientational averaging results in [106, 109]:

$$\left\langle \mu^{E}_{ge_3}\mu^{\mathcal{E}}_{e_3e_2}\mu^{\mathcal{E}}_{e_2e_1}\mu^{E}_{e_1g}\right\rangle^{\text{m. a.}}_{\text{or}} = \frac{1}{9}\left(\vec{\mu}_{e_1g}\cdot\vec{\mu}_{ge_3}\right)\left(\vec{\mu}_{e_2e_1}\cdot\vec{\mu}_{e_3e_2}\right). \tag{2.76}$$

The Stark spectrum is finally calculated as:

$$S(\omega) = \omega\text{Re}\int_0^\infty \text{d}t\text{e}^{\text{i}\omega t}\left\langle R^{(3)}_S\left(t;\vec{o}_E;\vec{o}_{\mathcal{E}}\right)\right\rangle_{\text{dis}}. \tag{2.77}$$

Expression (2.75) is one of the major results of this thesis.

2.5 2D spectroscopy

2D spectroscopy was introduced in detail in Chapter 1. Here we provide expressions needed to calculate the so-called total 2D spectrum using the ctR theory.

From the 2D experiment scheme depicted in Fig. 1.1d, we see that the sample is excited by three laser pulses, which have different wavevectors $\vec{k}_1, \vec{k}_2, \vec{k}_3$. Due to the wave-mixing, the outgoing signal is generated at all combinations of the wavevectors $\pm\vec{k}_1 \pm \vec{k}_2 \pm \vec{k}_3$. We are interested in the 2D spectrum recorded in the $\vec{k}_{\text{I}} = -\vec{k}_1 + \vec{k}_2 + \vec{k}_3$ direction. Another direction, $\vec{k}_{\text{II}} = \vec{k}_1 - \vec{k}_2 + \vec{k}_3$ is also of note. Experimental total 2D spectrum, which depends on the excitation frequency ω_1, the waiting time t_2 and the detection frequency ω_3, is

$$S_{\vec{k}_{\text{I}}}(\omega_3, t_2, \omega_1) = \int_{-\infty}^{\infty}\text{d}t_1\text{e}^{-\text{i}\omega_1 t_1}S_{\vec{k}_{\text{I}}}(\omega_3, t_2, t_1). \tag{2.78}$$

Here

$$S_{\vec{k}_{\text{I}}}(\omega_3, t_2, t_1) = \int_0^\infty \text{d}t_3\text{e}^{\text{i}\omega_3 t_3}\vec{E}_{\vec{k}_{\text{I}}}(t_3, t_2, t_1)\cdot\vec{o}_{\text{LO}}. \tag{2.79}$$

is an experimentally available signal [64]. $\vec{E}_{\vec{k}_{\text{I}}}(t_3, t_2, t_1)$ is the outgoing electric field and $\vec{o}_{\text{LO}}$ is the polarization vector of the LO pulse (see Section 1.1). As defined in Section 1.1, t_1 is the time delay between the first two excitation pulses (pump pulses), t_2 is the time delay between the second and third excitation pulses (last pump pulse and the probe pulse) and t_3 is the time delay between the third pulse and the signal. Note, however, that in experiments t_2 and t_3 are always positive, but t_1 can have negative values, which means that the order of the two pump pulses is reversed.

It can be shown that the outgoing electric field is proportional to the induced polarization [86]:

$$\vec{E}_{\vec{k}_\mathrm{I}}(t_3, t_2, t_1) = \mathrm{i}\vec{P}^{(3)}_{\vec{k}_\mathrm{I}}(t_3, t_2, t_1)\,. \tag{2.80}$$

The third order polarization can be calculated using the perturbation theory and the response function formalism [86]. Assuming the RWA, and limiting the consideration to the ultrashort pulses we obtain the following expression for the polarization:

$$\begin{aligned}\vec{P}^{(3)}_{\vec{k}_\mathrm{I}}(t_3, t_2, t_1) = \mathrm{i}^3 \Bigg\{ & \theta(t_1)\, R^{(3)}_{\vec{k}_\mathrm{I}}(t_3, t_2, t_1;\ , \vec{o}_3, \vec{o}_2, \vec{o}_1)\,. \\ & + \theta(-t_1)\, R^{(3)}_{\vec{k}_\mathrm{II}}(t_3, t_2, -t_1;\ , \vec{o}_3, \vec{o}_2, \vec{o}_1) \Bigg\}.\end{aligned} \tag{2.81}$$

Here $\theta(t)$ is the Heaviside step function, $\vec{o}_i$ are the polarization vectors of the electric field that interacts with the system at time moments t_i and $R^{(3)}_{\vec{k}_{\mathrm{I/II}}}$ are specific parts of the full third order response function, which is defined as

$$\begin{aligned}R^{(3)}\left(t_3, t_2, t_1; \vec{E}_4, \vec{E}_3, \vec{E}_2, \vec{E}_1\right) = \Bigg\langle \mathrm{Tr}\Bigg\{ & \left(\hat{\vec{\mu}}\cdot\vec{E}_4\right) \mathrm{e}^{-\mathrm{i}\hat{H}t_3}\left[\left(\hat{\vec{\mu}}\cdot\vec{E}_3\right), \mathrm{e}^{-\mathrm{i}\hat{H}t_2}\right. \\ & \left.\left[\left(\hat{\vec{\mu}}\cdot\vec{E}_2\right), \mathrm{e}^{-\mathrm{i}\hat{H}t_1}\left[\left(\hat{\vec{\mu}}\cdot\vec{E}_1\right), \hat{\rho}_{gg}\right]\mathrm{e}^{\mathrm{i}\hat{H}t_1}\right]\mathrm{e}^{\mathrm{i}\hat{H}t_2}\right]\mathrm{e}^{\mathrm{i}\hat{H}t_3}\Bigg\}\Bigg\rangle_{\mathrm{or}}.\end{aligned} \tag{2.82}$$

Formally the third order response function is a fourth rank tensor, thus it requires four vector arguments to give a scalar. When only three vector arguments are supplied, a fourth rank tensor gives a vector, as is the case in Eq. (2.81). Response functions with a direction index correspond to specific terms of Eq. (2.82), which oscillate as

$$R^{(3)}_{\vec{k}_\mathrm{I}} \sim \mathrm{e}^{-\mathrm{i}\omega_0(t_3 - t_1)}, \tag{2.83}$$

$$R^{(3)}_{\vec{k}_\mathrm{II}} \sim \mathrm{e}^{-\mathrm{i}\omega_0(t_3 + t_1)}. \tag{2.84}$$

Here ω_0 is the characteristic interband frequency, which corresponds to the energy difference between the ground state and the single-excited state manifold. The laser pulses used in experiments should also have similar central frequency. Expressions for the response function terms will be provided below.

Using the expression for the third order polarization, we obtain

$$\vec{E}_{\vec{k}_\mathrm{I}}(t_3, t_2, t_1)\cdot\vec{o}_\mathrm{LO} = \theta(t_1)\, R^{(3)}_{\vec{k}_\mathrm{I}}(t_3, t_2, t_1; \vec{o}_\mathrm{LO}, \vec{o}_3, \vec{o}_2, \vec{o}_1)$$

$$+\,\theta\left(-t_1\right) R^{(3)}_{\vec{k}_{\mathrm{II}}}\left(t_3, t_2, -t_1; \vec{o}_{\mathrm{LO}}, \vec{o}_3, \vec{o}_2, \vec{o}_1\right). \tag{2.85}$$

In the following, we will suppress the vector arguments to the response function, as they will be understood to be as in this expression. Furthermore, we will use the scalar dipole moments $\hat{\mu}^i = \hat{\vec{\mu}} \cdot \vec{o}_i$, with $i = 1, 2, 3, 4 \equiv \mathrm{LO}$.

Combining Eqs. (2.78), (2.79) and (2.85) we obtain the final expression needed to calculate the total 2D spectra:

$$\begin{aligned} S_{\vec{k}_{\mathrm{I}}}\left(\omega_3, t_2, \omega_1\right) = &\int_0^\infty \mathrm{d}t_3 \mathrm{e}^{\mathrm{i}\omega_3 t_3} \int_0^\infty \mathrm{d}t_1 \mathrm{e}^{-\mathrm{i}\omega_1 t_1} \left\langle R^{(3)}_{\vec{k}_{\mathrm{I}}}\left(t_3, t_2, t_1\right)\right\rangle_{\mathrm{dis}} \\ &+ \int_0^\infty \mathrm{d}t_3 \mathrm{e}^{\mathrm{i}\omega_3 t_3} \int_0^\infty \mathrm{d}t_1 \mathrm{e}^{\mathrm{i}\omega_1 t_1} \left\langle R^{(3)}_{\vec{k}_{\mathrm{II}}}\left(t_3, t_2, t_1\right)\right\rangle_{\mathrm{dis}}. \end{aligned} \tag{2.86}$$

The only thing that remains is to develop expressions for the relevant terms of the response function. Here we have also taken the averaging over disorder into account.

The directional response functions can be separated to three terms:

$$R^{(3)}_{\vec{k}_{\mathrm{I/II}}}\left(t_3, t_2, t_1\right) = R^{\mathrm{ESA}}_{\vec{k}_{\mathrm{I/II}}}\left(t_3, t_2, t_1\right) + R^{\mathrm{ESE}}_{\vec{k}_{\mathrm{I/II}}}\left(t_3, t_2, t_1\right) + R^{\mathrm{GSB}}_{\vec{k}_{\mathrm{I/II}}}\left(t_3, t_2, t_1\right). \tag{2.87}$$

They correspond to the ESA, ESE and GSB contributions. Assuming that the excited states of the system under consideration can be separated into the ground state, the single-excited state and the double-excited state manifolds, we can express the molecular dipole moment operator as

$$\hat{\vec{\mu}} = \underbrace{\sum_e^{N_{\mathrm{tot}}} \vec{\mu}_{eg}|e\rangle\langle g|}_{\hat{\vec{\mu}}_{[eg]}} + \underbrace{\sum_e^{N_{\mathrm{tot}}} \vec{\mu}_{ge}|g\rangle\langle e|}_{\hat{\vec{\mu}}_{[ge]}} + \underbrace{\sum_e^{N_{\mathrm{tot}}} \sum_f^{N_{2\mathrm{tot}}} \vec{\mu}_{fe}|f\rangle\langle e|}_{\hat{\vec{\mu}}_{[fe]}} + \underbrace{\sum_e^{N_{\mathrm{tot}}} \sum_f^{N_{2\mathrm{tot}}} \vec{\mu}_{ef}|e\rangle\langle f|}_{\hat{\vec{\mu}}_{[ef]}}. \tag{2.88}$$

Now we can express the response function terms. Remembering (2.82) and using (2.83) and (2.84) we obtain:

$$\begin{aligned} &R^{\mathrm{ESA}}_{\vec{k}_{\mathrm{I}}}\left(t_3, t_2, t_1\right) = \\ &\quad - \left\langle \mathrm{Tr}\left\{\hat{\mu}^1_{[ge]} \mathrm{e}^{\mathrm{i}\hat{H}(t_1+t_2+t_3)} \hat{\mu}^4_{[ef]} \mathrm{e}^{-\mathrm{i}\hat{H}t_3} \hat{\mu}^3_{[fe]} \mathrm{e}^{-\mathrm{i}\hat{H}t_2} \hat{\mu}^2_{[eg]} \mathrm{e}^{-\mathrm{i}\hat{H}t_1} \hat{\rho}_{gg}\right\}\right\rangle_{\mathrm{or}}; \end{aligned} \tag{2.89}$$

$$R^{\mathrm{ESE}}_{\vec{k}_{\mathrm{I}}}\left(t_3, t_2, t_1\right) =$$

$$\left\langle \mathrm{Tr}\left\{ \hat{\mu}^1_{[ge]} \mathrm{e}^{\mathrm{i}\hat{H}(t_1+t_2)} \hat{\mu}^3_{[eg]} \mathrm{e}^{\mathrm{i}\hat{H}t_3} \hat{\mu}^4_{[ge]} \mathrm{e}^{-\mathrm{i}\hat{H}(t_3+t_2)} \hat{\mu}^2_{[eg]} \mathrm{e}^{-\mathrm{i}\hat{H}t_1} \hat{\rho}_{gg} \right\} \right\rangle_{\mathrm{or}} ; \tag{2.90}$$

$$R^{\mathrm{GSB}}_{\vec{k}_{\mathrm{I}}}(t_3,t_2,t_1) = \left\langle \mathrm{Tr}\left\{ \hat{\mu}^1_{[ge]} \mathrm{e}^{\mathrm{i}\hat{H}t_1} \hat{\mu}^2_{[eg]} \mathrm{e}^{\mathrm{i}\hat{H}(t_2+t_3)} \hat{\mu}^4_{[ge]} \mathrm{e}^{-\mathrm{i}\hat{H}t_3} \hat{\mu}^3_{[eg]} \mathrm{e}^{-\mathrm{i}\hat{H}(t_2+t_1)} \hat{\rho}_{gg} \right\} \right\rangle_{\mathrm{or}} ; \tag{2.91}$$

$$R^{\mathrm{ESA}}_{\vec{k}_{\mathrm{II}}}(t_3,t_2,t_1) = -\left\langle \mathrm{Tr}\left\{ \mathrm{e}^{\mathrm{i}\hat{H}t_1} \hat{\mu}^2_{[ge]} \mathrm{e}^{\mathrm{i}\hat{H}(t_2+t_3)} \hat{\mu}^4_{[ef]} \mathrm{e}^{-\mathrm{i}\hat{H}t_3} \hat{\mu}^3_{[fe]} \mathrm{e}^{-\mathrm{i}\hat{H}(t_2+t_1)} \hat{\mu}^1_{[eg]} \hat{\rho}_{gg} \right\} \right\rangle_{\mathrm{or}} ; \tag{2.92}$$

$$R^{\mathrm{ESE}}_{\vec{k}_{\mathrm{II}}}(t_3,t_2,t_1) = \left\langle \mathrm{Tr}\left\{ \mathrm{e}^{\mathrm{i}\hat{H}t_1} \hat{\mu}^2_{[ge]} \mathrm{e}^{\mathrm{i}\hat{H}t_2} \hat{\mu}^3_{[eg]} \mathrm{e}^{\mathrm{i}\hat{H}t_3} \hat{\mu}^4_{[ge]} \mathrm{e}^{-\mathrm{i}\hat{H}(t_3+t_2+t_1)} \hat{\mu}^1_{[eg]} \hat{\rho}_{gg} \right\} \right\rangle_{\mathrm{or}} ; \tag{2.93}$$

$$R^{\mathrm{GSB}}_{\vec{k}_{\mathrm{II}}}(t_3,t_2,t_1) = \left\langle \mathrm{Tr}\left\{ \mathrm{e}^{\mathrm{i}\hat{H}(t_1+t_2+t_3)} \hat{\mu}^4_{[ge]} \mathrm{e}^{-\mathrm{i}\hat{H}t_3} \hat{\mu}^3_{[eg]} \mathrm{e}^{-\mathrm{i}\hat{H}t_2} \hat{\mu}^2_{[ge]} \mathrm{e}^{-\mathrm{i}\hat{H}t_1} \hat{\mu}^1_{[eg]} \hat{\rho}_{gg} \right\} \right\rangle_{\mathrm{or}} . \tag{2.94}$$

Now we need to calculate these expressions. The simplest is to deal with the GSB terms. We will assume the secular approximation. Then, expanding the response function in the system eigenbasis, we obtain

$$R^{\mathrm{GSB}}_{\vec{k}_{\mathrm{I}}}(t_3,t_2,t_1) = \sum_{e_1}^{N_{\mathrm{tot}}} \sum_{e_2}^{N_{\mathrm{tot}}} \left\langle \mu^4_{ge_2} \mu^3_{e_2 g} \mu^2_{e_1 g} \mu^1_{g e_1} \right\rangle \times \mathrm{Tr}_{\mathrm{B}} \left\{ \langle e_1 | \mathrm{e}^{\mathrm{i}\hat{H}t_1} | e_1 \rangle \langle g | \mathrm{e}^{\mathrm{i}\hat{H}(t_2+t_3)} | g \rangle \langle e_2 | \mathrm{e}^{-\mathrm{i}\hat{H}t_3} | e_2 \rangle \langle g | \mathrm{e}^{-\mathrm{i}\hat{H}(t_2+t_1)} | g \rangle \hat{\rho}^{\mathrm{eq}}_{\mathrm{B}} \right\}, \tag{2.95}$$

and similarly for $R^{\mathrm{GSB}}_{\vec{k}_{\mathrm{II}}}(t_3,t_2,t_1)$. The trace then can be calculated using the second order cumulant expansion (see discussion in Appendix A).

The treatment of the ESA and ESE terms is slightly more complicated. First, we separate these contributions into coherence and population terms: $\mathrm{ESA} = \mathrm{ESA_c} + \mathrm{ESA_p}$. We have coherence term when interaction with the first two light pulses creates coherence $|e_1\rangle\langle e_2|$, with $e_1 \neq e_2$. On the other hand, we have population term, when the first two light pulses create population $|e_1\rangle\langle e_1|$. Coherence terms can be treated in the same way as the GSB terms. For example,

$$R^{\mathrm{ESA_c}}_{\vec{k}_{\mathrm{I}}}(t_3,t_2,t_1) = -\sum_{e_1}^{N_{\mathrm{tot}}} \sum_{e_2}^{e_1 \neq e_2} \sum_{f_1}^{N_{2\mathrm{tot}}} \left\langle \mu^4_{e_1 f_1} \mu^3_{f_1 e_2} \mu^2_{e_2 g} \mu^1_{g e_1} \right\rangle_{\mathrm{or}}$$

$$\times \mathrm{Tr_B}\left\{\langle e_1|\mathrm{e}^{\mathrm{i}\hat{H}(t_1+t_2+t_3)}|e_1\rangle\langle f_1|\mathrm{e}^{-\mathrm{i}\hat{H}t_3}|f_1\rangle\langle e_2|\mathrm{e}^{-\mathrm{i}\hat{H}t_2}|e_2\rangle\langle g|\mathrm{e}^{-\mathrm{i}\hat{H}t_1}|g\rangle\hat{\rho}_{\mathrm{B}}^{\mathrm{eq}}\right\}. \tag{2.96}$$

Again, the trace can be evaluated using the second order cumulant expansion. Other coherence terms can be calculated similarly.

The treatment of populations terms is much less straightforward. The reason behind this is that a direct application of the cumulant expansion would give expressions accurate only for small t_2 values. Thus, population transfer at long time would be poorly described. Therefore, additional assumptions and approximations are necessary. First, we will assume that population transfer happens only during the t_2 interval. Then, taking one term as an example,

$$\begin{aligned} R_{\vec{k}_{\mathrm{I}}}^{\mathrm{ESE_p}}(t_3,t_2,t_1) = &\sum_{e_1}^{N_{\mathrm{tot}}}\sum_{e_2}^{N_{\mathrm{tot}}}\left\langle \mu_{ge_2}^4\mu_{e_2g}^3\mu_{e_1g}^2\mu_{ge_1}^1\right\rangle_{\mathrm{or}} \\ &\times \mathrm{Tr_B}\Bigg\{\langle e_1|\mathrm{e}^{\mathrm{i}\hat{H}t_1}|e_1\rangle\langle e_1|\mathrm{e}^{\mathrm{i}\hat{H}t_2}|e_2\rangle\langle g|\mathrm{e}^{\mathrm{i}\hat{H}t_3}|g\rangle \\ &\times \langle e_2|\mathrm{e}^{-\mathrm{i}\hat{H}t_3}|e_2\rangle\langle e_2|\mathrm{e}^{-\mathrm{i}\hat{H}t_2}|e_1\rangle\langle g|\mathrm{e}^{-\mathrm{i}\hat{H}t_1}|g\rangle\hat{\rho}_{\mathrm{B}}^{\mathrm{eq}}\Bigg\}. \end{aligned} \tag{2.97}$$

Now we assume that the trace over the different time periods can be performed independently. Unfortunately, this Markovian approximation would destroy the correlations between the different time intervals. To mitigate this, we assume a different state of the bath for each time interval. We thus obtain

$$\begin{aligned} R_{\vec{k}_{\mathrm{I}}}^{\mathrm{ESE_p}}(t_3,t_2,t_1) = &\sum_{e_1}^{N_{\mathrm{tot}}}\sum_{e_2}^{N_{2\mathrm{tot}}}\left\langle \mu_{ge_2}^4\mu_{e_2g}^3\mu_{e_1g}^2\mu_{ge_1}^1\right\rangle_{\mathrm{or}} \\ &\times \mathrm{Tr_B}\left\{\langle g|\mathrm{e}^{\mathrm{i}\hat{H}t_3}|g\rangle\langle e_2|\mathrm{e}^{-\mathrm{i}\hat{H}t_3}|e_2\rangle\hat{\rho}_{\mathrm{B}}(e_1e_1,t_2;ge_1,t_1)\right\}/\mathrm{Tr_B}\left\{\hat{\rho}_{\mathrm{B}}(ge_1,t_1)\right\} \\ &\times \mathrm{Tr_B}\left\{\langle e_1|\mathrm{e}^{\mathrm{i}\hat{H}t_2}|e_2\rangle\langle e_2|\mathrm{e}^{-\mathrm{i}\hat{H}t_2}|e_1\rangle\hat{\rho}_{e_1}^{\mathrm{eq}}\right\} \\ &\times \mathrm{Tr_B}\left\{\langle e_1|\mathrm{e}^{\mathrm{i}\hat{H}t_1}|e_1\rangle\langle g|\mathrm{e}^{-\mathrm{i}\hat{H}t_1}|g\rangle\hat{\rho}_{\mathrm{B}}^{\mathrm{eq}}\right\}. \end{aligned} \tag{2.98}$$

Here

$$\hat{\rho}_{\mathrm{B}}(e_1e_1,t_2;ge_1,t_1) = \mathrm{e}^{-\mathrm{i}\left(\hat{F}_{e_1e_1}+\hat{H}_{\mathrm{B}}\right)t_2}\mathrm{e}^{-\mathrm{i}\hat{H}_{\mathrm{B}}t_1}\hat{\rho}_{\mathrm{B}}^{\mathrm{eq}}\mathrm{e}^{\mathrm{i}\left(\hat{F}_{e_1e_1}+\hat{H}_{\mathrm{B}}\right)t_1}\mathrm{e}^{\mathrm{i}\left(\hat{F}_{e_1e_1}+\hat{H}_{\mathrm{B}}\right)t_2} \tag{2.99}$$

and

$$\hat{\rho}_{e_1}^{\mathrm{eq}} = \lim_{t'\to\infty}\mathrm{e}^{-\mathrm{i}\left(\hat{F}_{e_1e_1}+\hat{H}_{\mathrm{B}}\right)t'}\hat{\rho}_{\mathrm{B}}^{\mathrm{eq}}\mathrm{e}^{\mathrm{i}\left(\hat{F}_{e_1e_1}+\hat{H}_{\mathrm{B}}\right)t'}. \tag{2.100}$$

In Eq. (2.98) the traces in the second and fourth lines are evaluated using the cumulant expansion. Note that in the second line the division by $\mathrm{Tr_B}\left\{\hat{\rho}_{\mathrm{B}}(ge_1,t_1)\right\}$

is to prevent the double counting of the evolution of the bath state during the t_1 interval, which is already accounted for by the trace in the fourth line. Meanwhile, it can be shown that the trace in the third line can be identified with the population Green function as [113]:

$$G_{e_2e_1}(t_2) = \mathrm{Tr_B}\left\{\langle e_1|\mathrm{e}^{\mathrm{i}\hat{H}t_2}|e_2\rangle\langle e_2|\mathrm{e}^{-\mathrm{i}\hat{H}t_2}|e_1\rangle\hat{\rho}^{\mathrm{eq}}_{e_1}\right\}. \tag{2.101}$$

It represents probability the system to be in state e_2 at time t_2 if at initial time it was in state e_1. Green's function is the solution of the Pauli master equation:

$$\frac{\mathrm{d}}{\mathrm{d}t}G_{e_2e_1}(t) = -\sum_{e_3}^{e_3\neq e_2} K^{\mathrm{mR}}_{e_3e_2}G_{e_2e_1}(t) + \sum_{e_3}^{e_3\neq e_2} K^{\mathrm{mR}}_{e_2e_3}G_{e_3e_1}(t). \tag{2.102}$$

Here $K^{\mathrm{mR}}_{e_3e_2}$ are the mR transfer rates, see Eq. (2.50). All the rest of the population terms are evaluated similarly.

For completeness, now we list all the response function terms derived using the approach described here:

$$\begin{aligned}
&R^{\mathrm{ESA_c}}_{\vec{k}_{\mathrm{I}}}(t_1,t_2,t_3) = \\
&\quad -\sum_{e_1}^{N_{\mathrm{tot}}}\sum_{e_2}^{e_1\neq e_2}\sum_{f_1}^{N_{2\mathrm{tot}}}\left\langle \mu^4_{e_1f_1}\mu^3_{f_1e_2}\mu^2_{e_2g}\mu^1_{ge_1}\right\rangle_{\mathrm{or}}\exp\Big\{\mathrm{i}\omega_{e_1g}t_1 + \mathrm{i}\omega_{e_1e_2}t_2 - \mathrm{i}\omega_{f_1e_1}t_3 \\
&\qquad - g_{e_2e_2,e_2e_2}(t_2) - \xi_{e_2}(t_2) + g_{f_1f_1,e_2e_2}(t_2) + g_{f_1f_1,e_2e_2}(t_3) \\
&\qquad - g_{f_1f_1,e_2e_2}(t_2+t_3) - g_{f_1f_1,f_1f_1}(t_3) - \xi_{f_1}(t_3) + g^*_{e_1e_1,e_2e_2}(t_1+t_2) \\
&\qquad - g^*_{e_1e_1,e_2e_2}(t_1) - g_{e_1e_1,e_2e_2}(t_3) + g_{e_1e_1,e_2e_2}(t_2+t_3) \\
&\qquad + g^*_{e_1e_1,f_1f_1}(t_1+t_2+t_3) - g^*_{e_1e_1,f_1f_1}(t_1+t_2) + g_{e_1e_1,f_1f_1}(t_3) \\
&\qquad - g^*_{e_1e_1,e_1e_1}(t_1+t_2+t_3) - \xi^*_{e_1}(t_1+t_2+t_3)\Big\};
\end{aligned} \tag{2.103}$$

$$\begin{aligned}
&R^{\mathrm{ESA_p}}_{\vec{k}_{\mathrm{I}}}(t_1,t_2,t_3) = \\
&\quad -\sum_{e_1}^{N_{\mathrm{tot}}}\sum_{e_2}^{N_{\mathrm{tot}}}\sum_{f_1}^{N_{2\mathrm{tot}}}G_{e_2e_1}(t_2)\left\langle \mu^4_{e_2f_1}\mu^3_{f_1e_2}\mu^2_{e_1g}\mu^1_{ge_1}\right\rangle_{\mathrm{or}}\exp\Big\{\mathrm{i}\omega_{e_1g}t_1 - \mathrm{i}\omega_{f_1e_2}t_3 \\
&\qquad - g^*_{e_1e_1,e_1e_1}(t_1) - \xi^*_{e_1}(t_1) - g_{f_1f_1,f_1f_1}(t_3) - \xi_{f_1}(t_3) \\
&\qquad - g^*_{e_2e_2,e_2e_2}(t_3) - \xi^*_{e_2}(t_3) + g^*_{f_1f_1,e_2e_2}(t_3) + g_{e_2e_2,f_1f_1}(t_3) \\
&\qquad + g^*_{f_1f_1,e_1e_1}(t_1+t_2+t_3) - g^*_{f_1f_1,e_1e_1}(t_1+t_2)
\end{aligned}$$

$$
\begin{aligned}
&- g^*_{f_1 f_1, e_1 e_1}(t_2 + t_3) + g^*_{f_1 f_1, e_1 e_1}(t_2) \\
&- g^*_{e_2 e_2, e_1 e_1}(t_1 + t_2 + t_3) + g^*_{e_2 e_2, e_1 e_1}(t_1 + t_2) \\
&+ g^*_{e_2 e_2, e_1 e_1}(t_2 + t_3) - g^*_{e_2 e_2, e_1 e_1}(t_2) \\
&+ 2\mathrm{i}\mathrm{Im}\Big[g_{e_2 e_2, e_1 e_1}(t_2 + t_3) - g_{e_2 e_2, e_1 e_1}(t_2) - g_{e_2 e_2, e_1 e_1}(t_3) \\
&\qquad - g_{f_1 f_1, e_1 e_1}(t_2 + t_3) + g_{f_1 f_1, e_1 e_1}(t_2) + g_{f_1 f_1, e_1 e_1}(t_3) \Big] \Bigg\}; \qquad (2.104)
\end{aligned}
$$

$$
\begin{aligned}
&R^{\mathrm{ESE_c}}_{\vec{k}_\mathrm{I}}(t_1, t_2, t_3) = \\
&\sum_{e_1}^{N_\mathrm{tot}} \sum_{e_2}^{e_1 \neq e_2} \left\langle \mu^4_{g e_2} \mu^3_{e_1 g} \mu^2_{e_2 g} \mu^1_{g e_1} \right\rangle_\mathrm{or} \exp\Big\{ \mathrm{i}\omega_{e_1 g} t_1 + \mathrm{i}\omega_{e_1 e_2} t_2 - \mathrm{i}\omega_{e_3 g} t_3 \\
&\quad - g_{e_2 e_2, e_2 e_2}(t_2 + t_3) - \xi_{e_2}(t_2 + t_3) + g^*_{e_2 e_2, e_1 e_1}(t_1 + t_2 + t_3) \\
&\quad - g^*_{e_2 e_2, e_1 e_1}(t_1) - g^*_{e_2 e_2, e_1 e_1}(t_3) + g_{e_1 e_1, e_2 e_2}(t_2) \\
&\quad - g^*_{e_1 e_1, e_1 e_1}(t_1 + t_2) - \xi^*_{e_1}(t_1 + t_2) \Big\}; \qquad (2.105)
\end{aligned}
$$

$$
\begin{aligned}
&R^{\mathrm{ESE_p}}_{\vec{k}_\mathrm{I}}(t_1, t_2, t_3) = \\
&\sum_{e_1}^{N_\mathrm{tot}} \sum_{e_2}^{N_\mathrm{tot}} G_{e_2 e_1}(t_2) \left\langle \mu^4_{g e_2} \mu^3_{e_2 g} \mu^2_{e_1 g} \mu^1_{g e_1} \right\rangle_\mathrm{or} \exp\Big\{ \mathrm{i}\omega_{e_1 g} t_1 - \mathrm{i}\omega_{e_2 g} t_3 \\
&\quad - g^*_{e_1 e_1, e_1 e_1}(t_1) - \xi^*_{e_1}(t_1) - g_{e_2 e_2, e_2 e_2}(t_3) - \xi_{e_2}(t_3) \\
&\quad + g^*_{e_2 e_2, e_1 e_1}(t_1 + t_2 + t_3) - g^*_{e_2 e_2, e_1 e_1}(t_1 + t_2) \\
&\quad - g^*_{e_2 e_2, e_1 e_1}(t_2 + t_3) + g^*_{e_2 e_2, e_1 e_1}(t_2) \\
&\quad + 2\mathrm{i}\mathrm{Im}\Big[g_{e_2 e_2, e_1 e_1}(t_2) + g_{e_2 e_2, e_1 e_1}(t_3) - g_{e_2 e_2, e_1 e_1}(t_2 + t_3) \Big] \Big\}; \qquad (2.106)
\end{aligned}
$$

$$
\begin{aligned}
&R^{\mathrm{GSB_c}}_{\vec{k}_\mathrm{I}}(t_1, t_2, t_3) = \\
&\sum_{e_1}^{N_\mathrm{tot}} \sum_{e_2}^{N_\mathrm{tot}} \left\langle \mu^4_{g e_2} \mu^3_{e_2 g} \mu^2_{e_1 g} \mu^1_{g e_1} \right\rangle_\mathrm{or} \exp\Big\{ \mathrm{i}\omega_{e_1 g} t_1 - \mathrm{i}\omega_{e_2 g} t_3 \\
&\quad - g_{e_2 e_2, e_2 e_2}(t_3) - \xi_{e_2}(t_3) + g^*_{e_2 e_2, e_1 e_1}(t_1 + t_2 + t_3) - g^*_{e_2 e_2, e_1 e_1}(t_1 + t_2) \\
&\quad - g^*_{e_2 e_2, e_1 e_1}(t_2 + t_3) + g^*_{e_2 e_2, e_1 e_1}(t_2) - g^*_{e_1 e_1, e_1 e_1}(t_1) - \xi^*_{e_1}(t_1) \Big\}; \qquad (2.107)
\end{aligned}
$$

$$
\begin{aligned}
&R_{\vec{k}_{\mathrm{II}}}^{\mathrm{ESA_c}}(t_1,t_2,t_3) = \\
&\quad\sum_{e_1}^{N_{\mathrm{tot}}}\sum_{e_2}^{e_1\neq e_2}\sum_{f_1}^{N_{2\mathrm{tot}}}\left\langle \mu_{e_2f_1}^4\mu_{f_1e_1}^4\mu_{ge_2}^2\mu_{e_1g}^1\right\rangle_{\mathrm{or}}\exp\Big\{-\mathrm{i}\omega_{e_1g}t_1+\mathrm{i}\omega_{e_2e_1}t_2 \\
&\qquad-\mathrm{i}\omega_{f_1e_2}t_3-g_{e_1e_1,e_1e_1}(t_1+t_2)-\xi_{e_1}(t_1+t_2)+g_{f_1f_1,e_1e_1}(t_1+t_2) \\
&\qquad+g_{f_1f_1,e_1e_1}(t_3)-g_{f_1f_1,e_1e_1}(t_1+t_2+t_3)-g_{f_1f_1,f_1f_1}(t_3)-\xi_{f_1}(t_3) \\
&\qquad+g_{e_1e_1,e_2e_2}^*(t_2)-g_{e_2e_2,e_1e_1}(t_1)-g_{e_2e_2,e_1e_1}(t_3)+g_{e_2e_2,e_1e_1}(t_1+t_3+t_3) \\
&\qquad+g_{f_1f_1,e_2e_2}^*(t_2+t_3)-g_{f_1f_1,e_2e_2}^*(t_2)+g_{e_2e_2,f_1f_1}(t_3) \\
&\qquad-g_{e_2e_2,e_2e_2}^*(t_2+t_3)-\xi_{e_2}^*(t_2+t_3)\Big\}; \qquad (2.108)
\end{aligned}
$$

$$
\begin{aligned}
&R_{\vec{k}_{\mathrm{II}}}^{\mathrm{ESA_p}}(t_1,t_2,t_3) = \\
&\quad\sum_{e_1}^{N_{\mathrm{tot}}}\sum_{e_2}^{N_{\mathrm{tot}}}\sum_{f_1}^{N_{2\mathrm{tot}}}G_{e_2e_1}(t_2)\left\langle \mu_{e_2f_1}^4\mu_{f_1e_2}^3\mu_{ge_1}^2\mu_{e_1g}^1\right\rangle_{\mathrm{or}}\exp\Big\{-\mathrm{i}\omega_{e_1g}t_1-\mathrm{i}\omega_{f_1e_2}t_3 \\
&\qquad-g_{e_1e_1,e_1e_1}(t_1)-\xi_{e_1}(t_1)-g_{f_1f_1,f_1f_1}(t_3)-\xi_{f_1}(t_3) \\
&\qquad-g_{e_2e_2,e_2e_2}^*(t_3)-\xi_{e_2}^*(t_3)+g_{f_1f_1,e_2e_2}^*(t_3)+g_{e_2e_2,f_1f_1}(t_3) \\
&\qquad-g_{f_1f_1,e_1e_1}(t_1+t_2+t_3)+g_{f_1f_1,e_1e_1}(t_1+t_2)+g_{f_1f_1,e_1e_1}(t_2+t_3) \\
&\qquad-g_{f_1f_1,e_1e_1}(t_2)+g_{e_2e_2,e_1e_1}(t_1+t_2+t_3)-g_{e_2e_2,e_1e_1}(t_1+t_2) \\
&\qquad-g_{e_2e_2,e_1e_1}(t_2+t_3)+g_{e_2e_2,e_1e_1}(t_2) \\
&\qquad+2\mathrm{i}\mathrm{Im}\Big[g_{e_2e_2,e_1e_1}(t_2+t_3)-g_{e_2e_2,e_1e_1}(t_2)-g_{e_2e_2,e_1e_1}(t_3) \\
&\qquad\qquad-g_{f_1f_1,e_1e_1}(t_2+t_3)+g_{f_1f_1,e_1e_1}(t_2)+g_{f_1f_1,e_1e_1}(t_3)\Big]\Big\}; \qquad (2.109)
\end{aligned}
$$

$$
\begin{aligned}
&R_{\vec{k}_{\mathrm{II}}}^{\mathrm{ESE_c}}(t_1,t_2,t_3) = \\
&\quad\sum_{e_1}^{N_{\mathrm{t}}}\sum_{e_2}^{e_1\neq e_2}\left\langle \mu_{ge_1}^4\mu_{e_2g}^3\mu_{ge_2}^2\mu_{e_1g}^1\right\rangle_{\mathrm{or}}\exp\Big\{-\mathrm{i}\omega_{e_1g}t_1+\mathrm{i}\omega_{e_2e_1}t_2-\mathrm{i}\omega_{e_1g}t_3 \\
&\qquad-g_{e_1e_1,e_1e_1}(t_1+t_2+t_3)-\xi_{e_1}(t_1+t_2+t_3) \\
&\qquad+g_{e_1e_1,e_2e_2}^*(t_2+t_3)-g_{e_2e_2,e_1e_1}(t_1) \\
&\qquad-g_{e_1e_1,e_2e_2}^*(t_3)+g_{e_2e_2,e_1e_1}(t_1+t_2)-g_{e_2e_2,e_2e_2}^*(t_2)-\xi_{e_2}^*(t_2)\Big\}; \qquad (2.110)
\end{aligned}
$$

$$
\begin{aligned}
&R_{\vec{k}_{\mathrm{II}}}^{\mathrm{ESE_p}}(t_1,t_2,t_3) = \\
&\sum_{e_1}^{N_{\mathrm{tot}}}\sum_{e_2}^{N_{\mathrm{tot}}} G_{e_2e_1}(t_2)\left\langle \mu^4_{ge_2}\mu^3_{e_2g}\mu^2_{ge_1}\mu^1_{e_1g}\right\rangle_{\mathrm{or}} \exp\Big\{ -\mathrm{i}\omega_{e_1g}t_1 - \mathrm{i}\omega_{e_2g}t_3 \\
&\quad - g_{e_1e_1,e_1e_1}(t_1) - \xi_{e_1}(t_1) - g_{e_2e_2,e_2e_2}(t_3) - \xi_{e_2}(t_3) \\
&\quad - g_{e_2e_2,e_1e_1}(t_2) + g_{e_2e_2,e_1e_1}(t_1+t_2) \\
&\quad + g_{e_2e_2,e_1e_1}(t_2+t_3) - g_{e_2e_2,e_1e_1}(t_1+t_2+t_3) \\
&\quad + 2\mathrm{i}\mathrm{Im}\Big[g_{e_2e_2,e_1e_1}(t_2) + g_{e_2e_2,e_1e_1}(t_3) - g_{e_2e_2,e_1e_1}(t_2+t_3)\Big]\Big\};
\end{aligned}
\tag{2.111}
$$

$$
\begin{aligned}
&R_{\vec{k}_{\mathrm{II}}}^{\mathrm{GSB_c}}(t_1,t_2,t_3) = \\
&\sum_{e_1}^{N_{\mathrm{tot}}}\sum_{e_2}^{N_{\mathrm{tot}}} \left\langle \mu^4_{ge_2}\mu^3_{e_2g}\mu^2_{ge_1}\mu^1_{e_1g}\right\rangle_{\mathrm{or}} \exp\Big\{ -\mathrm{i}\omega_{e_1g}t_1 - \mathrm{i}\omega_{e_2g}t_3 \\
&\quad - g_{e_1e_1,e_1e_1}(t_1) - \xi_{e_1}(t_1) - g_{e_2e_2,e_1e_1}(t_2) + g_{e_2e_2,e_1e_1}(t_1+t_2) \\
&\quad + g_{e_2e_2,e_1e_1}(t_2+t_3) - g_{e_2e_2,e_1e_1}(t_1+t_2+t_3) - g_{e_2e_2,e_2e_2}(t_3) - \xi_{e_2}(t_3)\Big\}.
\end{aligned}
\tag{2.112}
$$

The transition dipole moments connecting the single and double excitation manifolds are

$$
\mu^i_{e_1f_1} = \langle e_1|\hat{\mu}^i|f_1\rangle. \tag{2.113}
$$

Lineshape functions related to the double-excited states are defined by generalizing expressions pertaining the single excitation manifold:

$$
g_{\alpha\beta,\gamma\delta}(t) = \int_0^t \mathrm{d}\tau_2 \int_0^{\tau_2} \mathrm{d}\tau_1 C_{\alpha\beta,\gamma\delta}(\tau_2-\tau_1)\,; \tag{2.114}
$$

$$
C_{\alpha\beta,\gamma\delta}(\tau_2-\tau_1) = \mathrm{Tr_B}\left(\hat{F}^{\mathrm{I}}_{\alpha\beta}(\tau_2)\,\hat{F}^{\mathrm{I}}_{\gamma\delta}(\tau_1)\,\hat{\rho}^{\mathrm{eq}}_{\mathrm{B}}\right), \tag{2.115}
$$

with $\hat{F}_{\alpha\beta} = \langle\alpha|\hat{H}_{\mathrm{SB}}|\beta\rangle$. $\alpha,\beta,\ldots$ can number both single-excited states $(e_1,e_2,\ldots)$ and double-excited states $(f_1,f_2,\ldots)$. The ctR theory term pertaining the double excitations is

$$
\xi_{f_1}(t) = \sum_{f_2\neq f_1}^{N_{2\mathrm{tot}}} \int_0^t \mathrm{d}\tau_2 \int_0^{\tau_2} \mathrm{d}\tau_1 \mathrm{e}^{\mathrm{i}\omega_{f_1f_2}(\tau_2-\tau_1)} C_{f_1f_2,f_2f_1}(\tau_2-\tau_1)\,. \tag{2.116}
$$

Assuming the pulses and the response polarized in the same direction, the relevant orientational average is [64, 87, 109]:

$$\left\langle \mu^4_{\alpha_4\beta_4}\mu^3_{\alpha_3\beta_3}\mu^2_{\alpha_2\beta_2}\mu^1_{\alpha_1\beta_1}\right\rangle_{\text{or}} = \frac{1}{15}\Big\{\left(\vec{\mu}_{\alpha_1\beta_1}\cdot\vec{\mu}_{\alpha_2\beta_2}\right)\left(\vec{\mu}_{\alpha_3\beta_3}\cdot\vec{\mu}_{\alpha_4\beta_4}\right) + \left(\vec{\mu}_{\alpha_1\beta_1}\cdot\vec{\mu}_{\alpha_3\beta_3}\right)\left(\vec{\mu}_{\alpha_2\beta_2}\cdot\vec{\mu}_{\alpha_4\beta_4}\right) + \left(\vec{\mu}_{\alpha_1\beta_1}\cdot\vec{\mu}_{\alpha_4\beta_4}\right)\left(\vec{\mu}_{\alpha_2\beta_2}\cdot\vec{\mu}_{\alpha_3\beta_3}\right)\Big\}. \tag{2.117}$$

Here α_i or β_i can also label the ground state, in addition to the single- or double-excited states.

Expressions for the response functions presented in this work are overall similar to Refs. [81, 87]. Nonetheless, the key novelty of this work is the inclusions of the ctR theory terms, which was not done before. In earlier works the lifetime broadening was mostly accounted for phenomenologically. As demonstrated in Section 2.3, inclusion of the ctR theory terms significantly improved the quality of the absorption lineshapes, thus similar improvement can be expected in the calculations of the 2D spectra.

2.6 Conclusions

In this chapter we presented the tight-binding Hamiltonian suitable to describe the dynamical and spectroscopic properties of various molecular aggregates. In the next chapter, it will be applied for the PSII RC.

We also presented derivations of expressions for the spectroscopic lineshapes in terms of the ctR theory. Though originally derived for absorption lineshapes by Renger and Marcus more than a decade ago [47], it was never used in actual calculations. Here we presented an investigation of several methods that account for the off-diagonal fluctuations when calculating the absorption lineshape. Our results clearly indicate that the ctR theory gives very good agreement with the HEOM results over a wide parameter range and should be considered for simulations when an exact theory is unavailable or too costly computationally. Comparison of other theories leads to the **second statement of the thesis**: Accounting for the lifetime broadening with complex and time-dependent terms significantly improves the quality of spectroscopic lineshapes, when the lineshape function formalism is used. Neglecting the imaginary part means ignoring the time-dependent reorganization and thus induces non-uniform peak shifts, while the Markovian approximation assumes relaxation independent of bath state and thus reduces the overall accuracy of the calculated lineshapes.

Additionally, we found that accounting for the off-diagonal fluctuations with the mR lifetimes gives much poorer agreement with the exact lineshapes. This was explained by analyzing the approximations needed to obtain that level of description. Since this approach was used in a number of studies of optical lineshapes of molecular systems, the parameters obtained might be misestimated and should be rechecked. This is done for the PSII RC in the next chapter.

In this chapter we also extended the ctR theory to describe the Stark spectrum. Our description is a considerable theoretical improvement over previous works [106, 136]. Though the obtained expression is somewhat computationally expensive, it allows calculations of the Stark spectrum on the same footing as absorption.

Finally, here we presented expressions needed to calculate the 2D spectra (see Chapter 1). Our results are similar to those of previous works [81, 87]. Nonetheless, whereas earlier the lifetime broadening was included phenomenologically, our expressions demonstrate how faithful application of theoretical principles gives terms that are complex, time-dependent and not generalizeable from simpler expressions. This level of theory will be applied for the first time to simulate the 2D spectra of the PSII RC in the next chapter.

The tight-binding Hamiltonian presented in this chapter is based on [**p9**] and [**P2**]. The ctR theory for absorption and the calculations of the absorption lineshapes for a dimer system is presented in [**P7**]. The Stark spectrum response function with ctR terms is developed in [**p9**], where expressions for the LD and CD spectra are also given. Response functions with ctR terms for the 2D spectra calculations are not published at the time of the writing.

Chapter 3

Microscopic model of PSII RC

For what, pray, is the pleasure of doing an easy thing?

JOHN CARTER in "The Gods of Mars"
by Edgar Rice Burroughs

Oxygenic photosynthesis in plants, cyanobacteria and algae begins in PSII, which is the only known biological complex with strong enough redox potential to split water. PSII is a dimeric supercomplex, consisting of major and minor light-harvesting complexes and the RC. Excitation within the light-harvesting antennae of PSII is transferred to the RC, leading to the oxidation of water, the reduction of plastoquinone and the formation of a proton gradient across the thylakoid membrane. The PSII is thus the main producer of oxygen on Earth [1, 61].

The PSII RC itself contains six Chl and two pheophytin (Pheo) molecules arranged into two almost symmetric branches, corresponding to the D1 and D2 proteins [37]. The pigment arrangement in the PSII RC is shown in Fig. 3.1. Two closely situated Chls, P_{D1} and P_{D2}, are known as the "special pair" (from the analogous attribution in the bacterial RC). Each branch also contains an accessory chlorophyll $Chl_{D1/D2}$ and a pheophytin $Pheo_{D1/D2}$. Two peripheral chlorophylls $Chlz_{D1/D2}$ are about 25 Å away from the other six RC pigments, and they do not participate in the primary charge separation. *In vivo*, the electron transfer proceeds through the D1 branch to $Pheo_{D1}$ and then further to plastoquinone Q_A and finally to Q_B [1]. The most often studied PSII RC preparation (the so-called D1D2cytb_{559} complex), however, lacks the oxygen evolving complex, the redox active tyrosine Tyr_Z and the quinone acceptors [137, 138], thus allowing the electrons to accumulate on $Pheo_{D1}$. Meanwhile, the hole remains

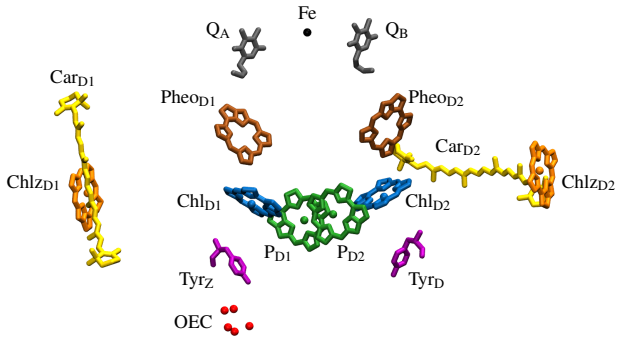

Figure 3.1: The structural arrangement of pigments and other cofactors in the PSII RC. Data taken from 3WU2 PDB structure [37]. The tails of chlorophylls, pheophytins and plastoquinones are truncated for clarity. Figure made with VMD software [147].

localized on P_{D1}.

The energy and charge transfer processes in the isolated PSII RC, the PSII core (which includes the CP43 and CP47 antenna complexes) or the whole PSII have been extensively studied over the last few decades, as reviewed in Refs. [54–61]. Nonetheless, the pathways of charge separation and the identities of the participating states are still under debate. Many studies claim that the primary electron donor is the Chl_{D1} pigment, thus the primary CT state is $Chl^+_{D1}Pheo^-_{D1}$ [110, 139–142]. In addition, a series of works [106, 107, 143] have highlighted the importance of the special pair CT state $P^+_{D2}P^-_{D1}$, which has been proposed to be strongly mixed with the exciton states, providing an alternative charge separation pathway. These suggestions have to be tested against an increasing amount of experimental data using appropriate theoretical modeling.

Most of the theoretical work on the PSII RC is based on the exciton concept [25]. The first exciton model that captured some features of the PSII RC spectroscopic data was the so-called multimer model [144]. It was formulated by taking the structural data of the bacterial reaction center into account and additionally assuming equal transition energies for all the core pigments. Later, as the PSII structural data became available with increasing resolution [34, 37, 145, 146], the theoretical models were refined [**P2**, 105–107, 110, 111, 119, 130], and many spectroscopic properties of the PSII RC were successfully described. Some models have included one or more CT states phenomenologically, treating them as additional exciton states [105–107, 130]. Only a few works have accounted for the relevant properties of electrons and holes [**P2**, 101].

Although there have been attempts to obtain the PSII RC site energies directly from the structural data [119, 148, 149], the majority of the theoretical

models derive their parameters from fits to the optical spectra. Since exact calculations are almost always too computationally expensive, approximate methods have to be applied to calculate optical lineshapes and dynamics. We have recently analyzed various approaches to calculating absorption lineshapes (see [**P7**] and Section 2.3) and have found that the ctR theory gives results very close to the exact ones. On the other hand, the mR theory, used in Refs. [105–107, 130] and in our previous work on the PSII RC [**P2**] was found to perform significantly worse. The Markovian Redfield approach (or cR), used in Refs. [110, 111, 119], showed improvements but did not perform as well as the ctR theory. These findings raise some doubts about the optimization of the parameters of the previous models of the PSII RC [**P2**, 105–107, 110, 111, 130] and motivate our use of the ctR theory for describing its spectroscopic properties.

The CT states, being optically dark, are insensitive to most spectroscopic measurements like absorption, LD or CD. Nonetheless, due to their strong static dipole moments, they are sensitive to the presence of static electric fields, and thus can influence the results of Stark spectroscopy. Stark experiments have been performed on the PSII RC [150], but the results were not easy to understand without a detailed theoretical description. Previously, the PSII RC Stark spectrum was fitted using mR theory [106]. Even though significant progress in understanding the observed features was achieved, a check of the obtained conclusions, especially the parameters of the CT states, using a more accurate lineshape theory is definitely called for.

In this chapter we revisit the spectroscopic properties of the PSII RC using the ctR theory (Chapter 2 and Ref. [**P7**]). We construct a model that includes a single CT state together with MEs. We obtain model parameters by fitting a number of linear optical spectra. We also extend the ctR theory to calculate the Stark spectrum, which is then used to tune the parameters of the CT state. Due to the more advanced lineshape theory, in our current model we improve upon the parameters obtained in our previous work based on mR [**P2**].

3.1 The model parameters of PSII RC

Since the PSII RC has 8 pigments, in addition to 8 ME states, there could be 56 possible CT states. If we limit the CT states to the particular pigments ($\mathrm{Chl_{D1}}$, $\mathrm{Pheo_{D1}}$, $\mathrm{P_{D1}}$, $\mathrm{P_{D2}}$) that have been proposed to be involved in charge separation, and take into consideration the directionality of the charge transfer, this number is significantly reduced to 6. Restricting the CT states to neighboring pigment

Table 3.1: Single excitation Hamiltonian matrix elements (in cm^{-1}), energies of the states in nanometers, and standard deviations of energy distributions (in cm^{-1}). See text for details.

	P_{D1}	P_{D2}	Chl_{D1}	Chl_{D2}	$Pheo_{D1}$	$Pheo_{D2}$	$Chlz_{D1}$	$Chlz_{D2}$	$Chl^+_{D1}Pheo^-_{D1}$	E_λ	σ
P_{D1}	15080	158	−27.3	−41.8	−4	12.6	0.5	0.6	0	663	80
P_{D2}	158	15015	−46.8	−22	15.1	−3	0.6	0.6	0	666	80
Chl_{D1}	−27.3	−46.8	14800	3.5	43.5	−2.2	1.7	−0.1	125	675.5	80
Chl_{D2}	−41.8	−22	3.5	15010	−2.4	41.7	−0.1	1.8	0	666	80
$Pheo_{D1}$	−4	15.1	43.5	−2.4	14950	1.5	−2.5	−0.2	125	669	80
$Pheo_{D2}$	12.6	−3	−2.2	41.7	1.5	14850	−0.2	−2.6	0	673.5	80
$Chlz_{D1}$	0.5	0.6	1.7	−0.1	−2.5	−0.2	14985	0.1	0	667.5	80
$Chlz_{D2}$	0.6	0.6	−0.1	1.8	−0.2	−2.6	0.1	15065	0	664	80
$Chl^+_{D1}Pheo^-_{D1}$	0	0	125	0	125	0	0	0	14270	701	550

pairs further reduces this number to 3. Given that the majority of the spectra that we fit (absorption, LD, CD) are not significantly affected by the dark CT states, we include a single CT state in our model. We note that only the Stark spectrum is sensitive to CT states, and previous attempts to fit the Stark spectrum of the PSII RC included a single CT state [106]. We performed calculations that considered either the $P^+_{D2}P^-_{D1}$ or $Chl^+_{D1}Pheo^-_{D1}$ CT states and from the fits of the Stark spectrum (see Section 3.2.1 for details) we have chosen $Chl^+_{D1}Pheo^-_{D1}$ as the primary CT state. Thus, our model includes 9 states in the single excitation manifold.

We obtain the site energies of the pigments from the fitting procedure. The resonance couplings between the pigments were taken from Ref. [151], where they were calculated using the Poisson TrEsp method [152–154]. The CT state energy and the coupling between the CT state and molecular states were also obtained from the fits. Formally, there are two couplings involving a single CT state,

$$\langle Phe^*_{D1}|\hat{H}_S|Chl^+_{D1}Pheo^-_{D1}\rangle = t^{\boldsymbol{h}}_{Pheo_{D1}Chl_{D1}}; \tag{3.1}$$

$$\langle Chl^*_{D1}|\hat{H}_S|Chl^+_{D1}Pheo^-_{D1}\rangle = t^{\boldsymbol{e}}_{Pheo_{D1}Chl_{D1}}; \tag{3.2}$$

but we have chosen $t^{\boldsymbol{e}}_{mn} = t^{\boldsymbol{h}}_{mn}$ for simplicity. The entire single excitation Hamiltonian matrix is given in Table 3.1.

Our model takes into account the disorder of the energies of the pigments and CT states. We assume the disorder for all pigments to be the same, and the CT state to have different disorder. In both cases, the disorder was described by a Gaussian distribution with standard deviations obtained from the fits (given in Table 3.1).

The strengths of the transition dipole moments of Chl and Pheo pigments are taken to be 4.4 and 3.4 debye respectively [**P2**, 111]. The transition dipole vectors are assumed to be directed from N_B to N_D atoms (for nomenclature see,

Table 3.2: The transition dipole moments in D, the static dipole moments in D, and the geometric center of the pigments in Å. Data taken from the 3WU2 crystal structure [37] obtained from OPM database [155].

	μ_x	μ_y	μ_z	$\Delta\mu_x$	$\Delta\mu_y$	$\Delta\mu_z$	R_x	R_y	R_z
P_{D1}	1.08	−3.74	2.05	0.32	−1.07	1.07	37.87	4.05	11.99
P_{D2}	−0.66	3.73	2.24	−0.13	1.03	1.15	32.57	9.55	11.12
Chl_{D1}	−0.33	4.06	1.67	0.29	1.34	0.73	30.65	−2.13	9.30
Chl_{D2}	0.11	−4.04	1.74	−0.36	−1.31	0.75	40.19	15.45	8.24
$Pheo_{D1}$	1.65	−0.55	−2.92	0.84	0.10	−0.99	33.73	−4.13	−0.31
$Pheo_{D2}$	−1.77	0.19	−2.90	−0.89	−0.19	−0.93	36.67	16.71	−1.41
$Chlz_{D1}$	−1.91	−0.64	3.91	−1.01	−0.32	1.13	31.92	−27.24	8.07
$Chlz_{D2}$	2.07	0.98	3.76	1.06	0.41	1.05	38.91	39.35	4.76

e. g., Ref. [156]) as obtained from the 3WU2 crystal structure [37]. The CT state was assumed to have no transition dipole strength. The static dipole moments are assumed to be rotated by 15° in the direction of the N_C atom from the N_B to N_D axis. This was based on the calculations of absorption difference spectra corresponding to the $P^+_{D1}Pheo^-_{D1}$ CT state, see Sec. 3.2.1 for details. Their strengths are taken to be 1.55 and 1.3 debyes for Chls and Pheos, respectively. The static dipole moment of the CT state was calculated by assuming charges fully localized at the geometric centers of the four N atoms of the involved pigments. This gives a static dipole strength of 49.3 debyes for the $Chl^+_{D1}Pheo^-_{D1}$ state. The transition dipole moments, the static dipole moments and the geometric centers of the pigments of the PSII RC are given in Table 3.2. Here the z axis is perpendicular to the membrane plane, with data taken from the 3WU2 crystal structure [37] obtained from the OPM database [155].

We assume that fluctuations of the energies are uncorrelated, thus $C''_{AB}(\omega) = C''_A\delta_{AB}$. All pigments (both Chls and Pheos) are described by the same spectral density consisting of two parts, $C''_{m^*}(\omega) = C''_{\mathrm{LF}}(\omega) + C''_{\mathrm{HF}}(\omega)$. In our previous work [**P2**] we assumed that the low frequency part was given by a Debye spectral density. However, this form is unsuitable for low temperature spectra calculations due to the divergence of the total Huang-Rhys factor [80]. Instead we adopt the superohmic spectral density which is free from this deficiency, consisting of two terms:

$$C''_{\mathrm{LF}}(\omega) = \sum_{j=1,2} \lambda_j \frac{\pi}{2} \frac{\omega^3}{\omega_j^{\mathrm{c}}} \exp\left(-|\omega|/\omega_j^{\mathrm{c}}\right). \tag{3.3}$$

The two cut-off frequencies were chosen to be $\omega_1^{\mathrm{c}} = 20\,\mathrm{cm}^{-1}$ and $\omega_2^{\mathrm{c}} = 80\,\mathrm{cm}^{-1}$. The values for reorganization energy were obtained from the fits of spectra and

Table 3.3: Parameters of the underdamped vibrations included in the spectral density (from ΔFLN measurements of Chl *a* in solution [157]).

Mode	1	2	3	4	5	6	7	8
W_j, cm^{-1}	93	189	262	352	389	519	573	745
s_j	0.012	0.010	0.013	0.023	0.015	0.016	0.017	0.034

found to be $\lambda_1 = 15\,\mathrm{cm}^{-1}$ and $\lambda_2 = 35\,\mathrm{cm}^{-1}$. The high frequency part is represented by 8 underdamped vibrational modes:

$$C''_{\mathrm{HF}}(\omega) = \sum_{j=1}^{8} \frac{4 s_j W_j \omega^3 \Gamma}{\left(\omega^2 - W_j^2 - \Gamma^2\right)^2 + 4\omega^2\Gamma^2}. \tag{3.4}$$

The damping parameter was chosen to be the same for all modes, $\Gamma^{-1} = 1\,\mathrm{ps}$. The frequencies W_j and the Huang-Rhys factors s_j were taken from Δ fluorescence line-narrowing (ΔFLN) measurements of Chl *a* in solution [157], and are given in Table 3.3. We included only the modes with center frequencies less than $750\,\mathrm{cm}^{-1}$, as higher frequency modes are not expected to influence system dynamics, being completely non-resonant. For the CT state we keep the high frequency part of the spectral density the same, but introduce an additional multiplicative factor for the low frequency part, as CT states are expected to couple more strongly to the environment. Thus, $C''_{\mathrm{CT}}(\omega) = \eta C''_{\mathrm{LF}}(\omega) + C''_{\mathrm{HF}}(\omega)$. From the fits of the Stark spectrum, we obtained $\eta = 12$ for the $\mathrm{Chl}^{+}_{\mathrm{D1}}\mathrm{Pheo}^{-}_{\mathrm{D1}}$ state.

3.2 Spectroscopy of PSII RC

3.2.1 Fits of optical spectra

Most of the model parameters were obtained from a fit of nine linear spectra shown in Fig. 3.2. In particular, we fitted absorption at 6, 77 and 298 K, linear and circular dichroism at 6 and 298 K, and absorption difference spectra with exchanged pheophytins at 6 K. The latter spectra correspond to the so-called RC1x and RC2x complexes [158, 159], where in the RC1x complexes 80 % of the $\mathrm{Pheo}_{\mathrm{D2}}$ is estimated to be replaced by 13^1-OH-Pheo, and in the RC2x complexes all $\mathrm{Pheo}_{\mathrm{D2}}$ and 50 % of $\mathrm{Pheo}_{\mathrm{D1}}$ is replaced. When calculating RC1x/RC2x spectra, we took this into account accordingly. The energies of the exchanged Pheos were also free parameters of the fit. In the fitting procedure, we minimized the sum of the deviations from the experimental data at each wavelength for each spectra and added them with different weights (1.0 for

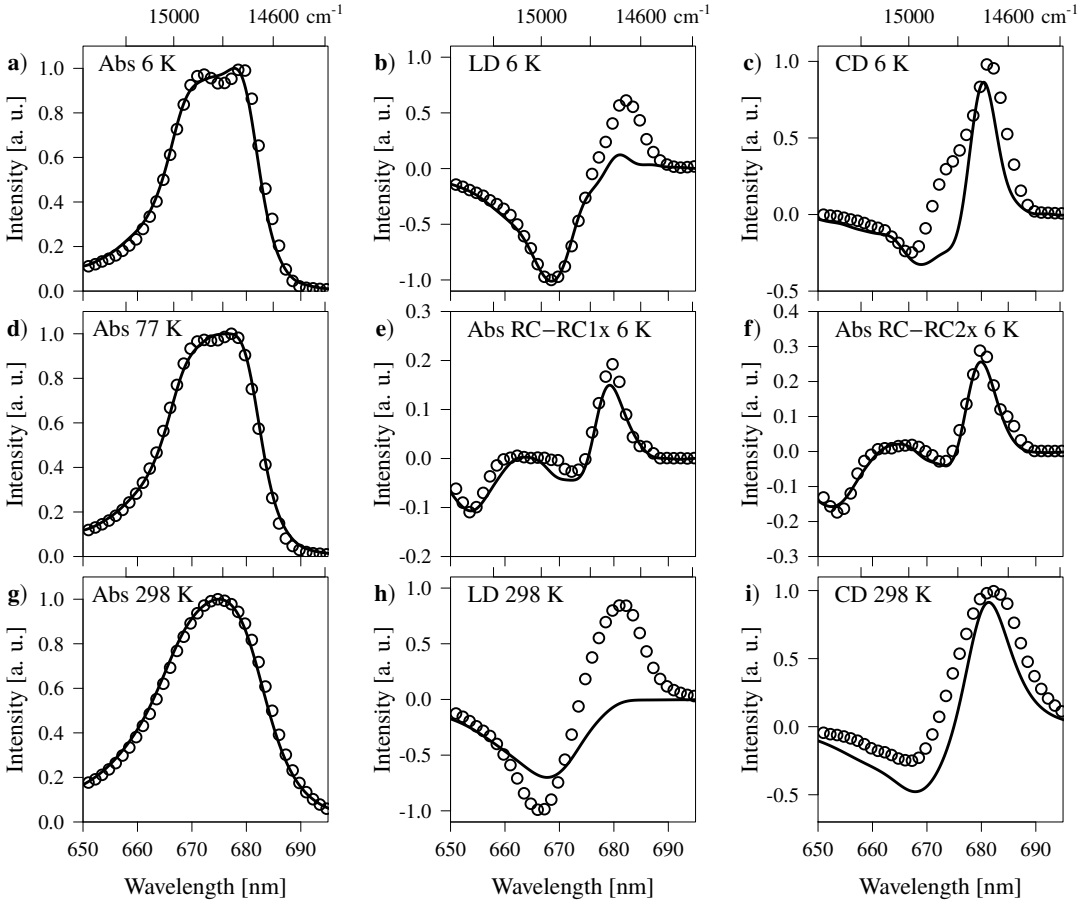

Figure 3.2: Fits of the PSII RC spectroscopic data. Open circles denote experimental values, while black lines denote theoretical calculations. a) absorption at 6 K. b) linear dichroism at 6 K. c) circular dichroism at 6 K. d) absorption at 77 K. e) absorption difference RC−RC1x preparations (with pheophytin exchange) at 6 K. f) absorption difference RC−RC2x preparations (with pheophytin exchange) at 6 K. g) absorption at 298 K. h) linear dichroism at 298 K. i) circular dichroism at 298 K. Experimental data for a) taken from Ref. [158], for b), c), e), f) and i) taken from Ref. [159], for d) taken from Ref. [160], for g) taken from Ref. [161].

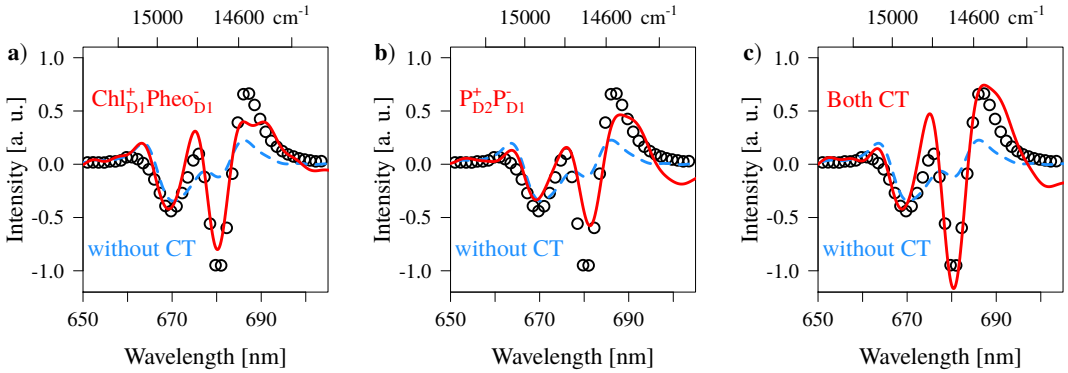

Figure 3.3: Fit of Stark spectrum of the PSII RC at 77 K. Open circles denote experimental values (data taken from Ref. [150]), red line corresponds to calculations with a) $\mathrm{Chl}^{+}_{\mathrm{D1}}\mathrm{Pheo}^{-}_{\mathrm{D1}}$ CT state, b) $\mathrm{P}^{+}_{\mathrm{D2}}\mathrm{P}^{-}_{\mathrm{D1}}$ CT state, c) both CT states. The parameters for CT states were fitted separately in a) and b). For c) calculations were made by taking parameters corresponding to the best fit from a) and b), and were not further adjusted. Blue dashed line denotes calculations without any CT states.

Abs 6 K and 298 K, 2.0 for Abs 77 K, 5.0 for Abs RC−RC1x/RC2x 6 K, 0.05 for LD 6 K, 0.005 for CD 6 K and 298 K, 0.01 for LD 298 K). Smaller weights were chosen for some spectra due to the poorer quality of the fit. Before calculating the differences, the calculated spectra were normalized in the following way: absorption spectra were normalized by setting the maximum amplitudes to unity, CD/LD spectra were normalized in such a way that the difference between experimental and calculated spectra would be the smallest, and absorption difference RC and RC1x/RC2x spectra were normalized to unity separately (this was done also to the experimental data) and then subtracted. Fitting was performed using R software [99] with a differential evolution algorithm [162] as implemented in Ref. [163].

We obtain excellent fits for all the absorption experiments, and good qualitative fits for CD. Note, however, that the experimental CD spectrum of the PSII RC is non-conservative, while our theoretical approach can give only conservative spectra in the Q_y region. There is some quantitative difference for the calculated LD spectra, with positive feature at $\sim 680\,\mathrm{nm}$ having less amplitude than in the experimental data. Overall, our results are of similar quality to previous works on the PSII RC [106, 110].

We have adjusted the CT state parameters (its energy, coupling with molecular states, disorder values and multiplicative factor describing coupling with low frequency vibrations) from the fits of the Stark spectrum measured at 77 K [150],

with results given in Fig. 3.3. During the fitting procedure both the experimental and the simulated Stark spectra were normalized with respect to the absorption spectrum. We tried including either $P^+_{D2}P^-_{D1}$ or $Chl^+_{D1}Pheo^-_{D1}$ CT states in our model. We found that a better fit was obtained with the $Chl^+_{D1}Pheo^-_{D1}$ state. Results with the $P^+_{D2}P^-_{D1}$ state are also reasonable but are somewhat worse – the amplitude of the ~ 680 nm feature is underestimated, and a negative feature at ~ 700 nm appears, which is absent in the experimental data. Therefore, we hold that $Chl^+_{D1}Pheo^-_{D1}$ should be the primary CT state, contrary to the conclusions obtained previously [106]. We also note that calculations without any CT states roughly reproduce the amplitude of the ~ 670 nm feature but severely underestimate the amplitude of the ~ 680 nm feature. This is a clear indication that CT states significantly influence the Stark spectrum of the PSII RC, much more than in previous calculations [106].

In previous theoretical works on the PSII RC, fitting of the relaxed fluorescence was employed to obtain the model parameters [105, 106, 110]. In our view, this approach is problematic and could lead to erroneous results. Since a normal RC performs charge separation with high efficiency, it should barely fluoresce. Thus, the majority of the fluorescence may originate from those RCs that cannot perform charge separation, due to their particular realization of static disorder that provides an unfavorable energy landscape. Fits of the relaxed fluorescence would then depend not on the normal RC, but only on a specific subensemble. A better approach to calculations of the fluorescence of the RC may be to simulate the time-resolved fluorescence, and then integrate over all times. Unfortunately this requires including all the relevant CT states in the model, and thus is out of scope of the present study.

3.2.2 Calculations of independent spectra

Having performed the fits and obtained the optimal values of the parameters, we checked our model by calculating other linear spectra, for which experimental results are available in literature.

We calculated the CD spectra of different PSII RC preparations (normal RC, RC1x and RC2x) at 6 K. The comparison of calculations with experimental data (taken from. Ref. [159]) is presented in Fig. 3.4. Our simulations qualitatively reproduce the changes observed in the CD spectra upon the increase of exchanged Pheo (going from RC to RC1x to RC2x). First, the main positive feature at ~ 680 nm loses a significant amount of amplitude. Second, a positive feature at ~ 675 nm appears. Third, the negative feature at ~ 670 nm loses its

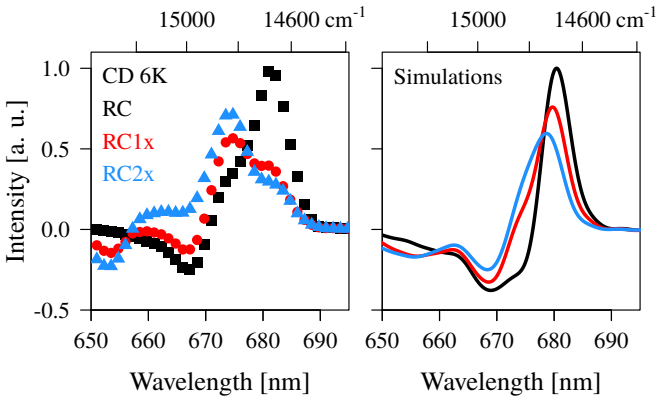

Figure 3.4: Comparison of 6 K CD spectra of different PSII RC preparations (with partial exchange of Pheos). Experimental data (taken from. Ref. [159]) denoted by symbols on the left, simulations denoted by lines on the right.

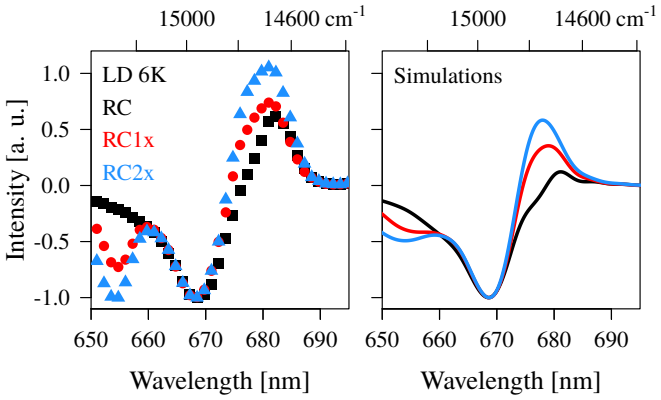

Figure 3.5: Comparison of 6 K LD spectra of different PSII RC preparations (with partial exchange of Pheos). Experimental data (taken from. Ref. [159]) denoted by symbols on the left, simulations denoted by lines on the right.

amplitude. Fourth, a negative feature at ~ 655 nm appears.

We also calculated LD spectra at 6 K of RC, RC1x and RC2x preparations. Comparison with experimental data is presented in Fig. 3.5. Again, our simulations qualitatively reproduce the main changes upon the increase of exchanged Pheo – appearance of negative feature at ~ 655 nm, lack of changes in negative feature at ~ 670 nm and increase of amplitude of positive feature at ~ 680 nm. Nonetheless, we have to note that the overall amplitudes of both the negative feature at ~ 655 nm and the positive feature at ~ 680 nm are considerably smaller in our simulations.

In Fig. 3.6 we compare the calculated triplet minus singlet absorption difference spectrum of the PSII RC with experimental data [159]. Calculations were

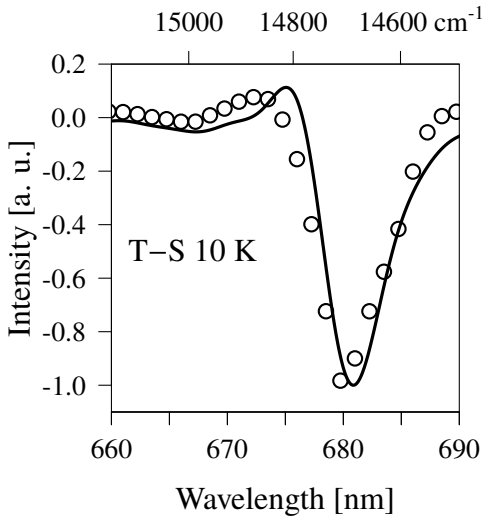

Figure 3.6: Triplet minus singlet absorption difference spectrum at 10 K. Open circles denote experimental values (data taken from Ref. [159]), black line corresponds to calculations, which were performed assuming triplet localized at Chl_{D1}.

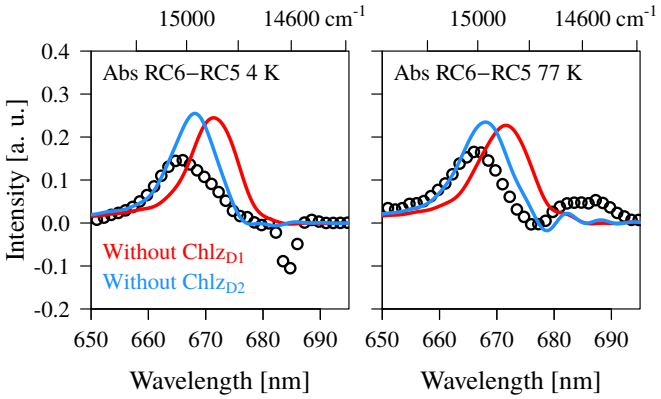

Figure 3.7: Comparison of experimental and calculated RC6−RC5 absorption difference spectra at 4 K (left, experimental data taken from Ref. [164]) and 77 K (right, experimental data taken from Ref. [165]). Experimental data denoted by open circles, red lines denote calculations done by neglecting $ChlzD_{1}$, blue lines – neglecting $ChlzD_{2}$.

performed assuming triplet localized at Chl_{D1}, and ignoring its couplings and dipole strength. We obtain good agreement with experimental data, similar to other works [106, 110, 119].

We calculated absorption difference spectra of normal RC preparations (here called RC6) and the so-called RC5 preparations, which lack one of the peripheral chlorophylls [164, 165]. Comparison with experimental data is presented in Fig. 3.7. Experimental spectra were calculated by normalizing both RC6 and

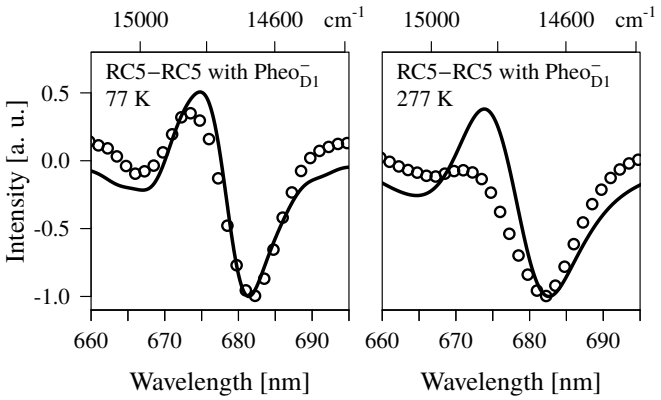

Figure 3.8: Comparison of experimental and calculated RC5−RC5 with Pheo_{D1} reduced absorption difference absorption difference spectra at 77 K (left) and 277 K (right). Experimental data (taken from Ref. [166] denoted by open circles, black lines denote calculations.

RC5 absorption at the $\sim$ 678 nm peak and subtracting the spectra, then normalizing with respect to the RC6 spectra. Simulated spectra were obtained by calculating normal RC6 spectra, then calculating the spectra without the $\text{Chlz}_{\text{D1/D2}}$ pigment, subtracting, and normalizing with respect to the RC6 spectra. Our calculations are consistent with Chlz_{D2} being lost in the RC5 preparations, with both peak position at $\sim$ 666 nm and its half-width agreeing with experimental data. The amplitude of the $\sim$ 666 nm peak is higher in the calculations, which could be related to differences in the low temperature experimental absorption spectra, as the amplitude of the $\sim$ 672 nm peak varies in different reports [158–160, 164].

In Fig. 3.8 we show a comparison of experimental and calculated $\text{RC5}-\text{RC5}_{\text{Pheo}^-_{\text{D1}}}$ absorption difference spectra (here $\text{RC5}_{\text{Pheo}^-_{\text{D1}}}$ means RC5 with reduced Pheo_{D1}) , with experimental data taken from Ref. [166]. Calculations were done assuming that in RC5 preparations the Chlz_{D2} is lost, consistent with our RC6−RC5 absorption difference calculations. When calculating spectra with reduced Pheo_{D1}, we neglected the couplings and dipole strength of this pigment. In addition, as suggested in Ref. [110], we took the electrochromic shifts into account. This was done by assuming a negative charge localized at the geometric center of the four nitrogen atoms of Pheo_{D1}, and then calculating the interaction of that charge with the static dipole moments of the other

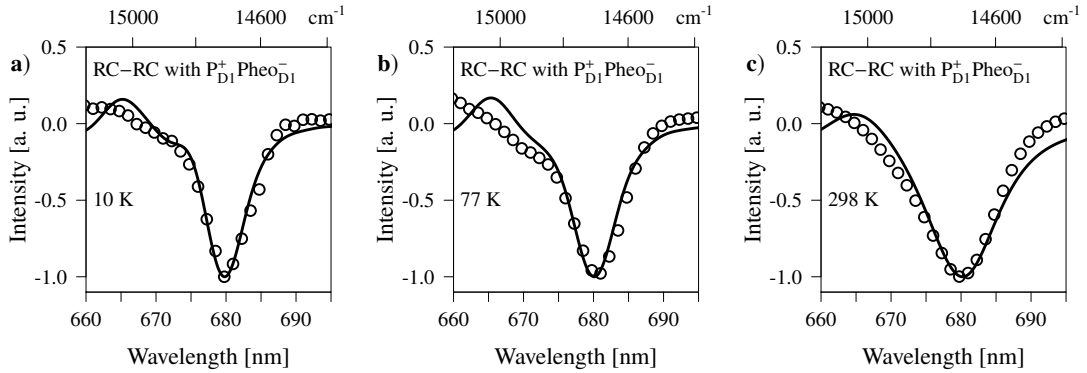

Figure 3.9: Comparison of experimental and calculated absorption difference spectra corresponding to the CT state $P^+_{D1}Pheo^-_{D1}$. Experimental data denoted by open circles, black lines denote calculations. a) 10 K (curve 2 from Fig. 2 of Ref. [167]). b) 77 K (EADS corresponding to 20 ns component of 660 nm excitation from Ref. [143]). c) 298 K (DADS corresponding to non-decaying component of 400 nm excitation from Ref. [161]).

pigments. That is,

$$\Delta\varepsilon_{n^*} = \frac{1}{4\pi\epsilon_0\epsilon_r}(-e)\frac{\left(\vec{R}_{\mathrm{Pheo_{D1}}} - \vec{R}_n\right)\cdot\Delta\vec{\mu}_n}{\left|\vec{R}_{\mathrm{Pheo_{D1}}} - \vec{R}_n\right|^3}. \tag{3.5}$$

Here ϵ_r is the relative dielectric constant, which was assumed to be equal to 2.5 in our calculations. The CT state was neglected in the calculations for the reduced $\mathrm{Pheo_{D1}}$, since we expect that due to its huge energy shift, it would effectively decouple from the ME states. As seen from Fig. 3.8, we obtain excellent agreement for 77 K data, with both the main negative feature at ~ 682 nm and the positive feature at ~ 673 nm reproduced. In calculations for 277 K we still reproduce the main negative feature, but obtain a larger amplitude for the positive one than it is in the experimental data.

We also calculated the absorption difference spectrum corresponding to the CT state $P^+_{D1}Pheo^-_{D1}$ taken from pump–probe measurements [143, 161, 167]. This state is the final CT state in the PSII RC preparations lacking the quinone acceptors. Comparison of the experimental data with simulations is presented in Fig. 3.9 for 10, 77 and 298 K. In calculations of the absorption with the CT state, we neglected the couplings and dipole strength of the involved pigments and accounted for the electrochromic shifts. The effective dielectric constant ϵ_r was assumed to be equal to 2.5, as before. We obtain good agreement between experiment and calculations for all temperatures. It is important to note that agreement was obtained only by assuming an angle of 15° between the N_B to

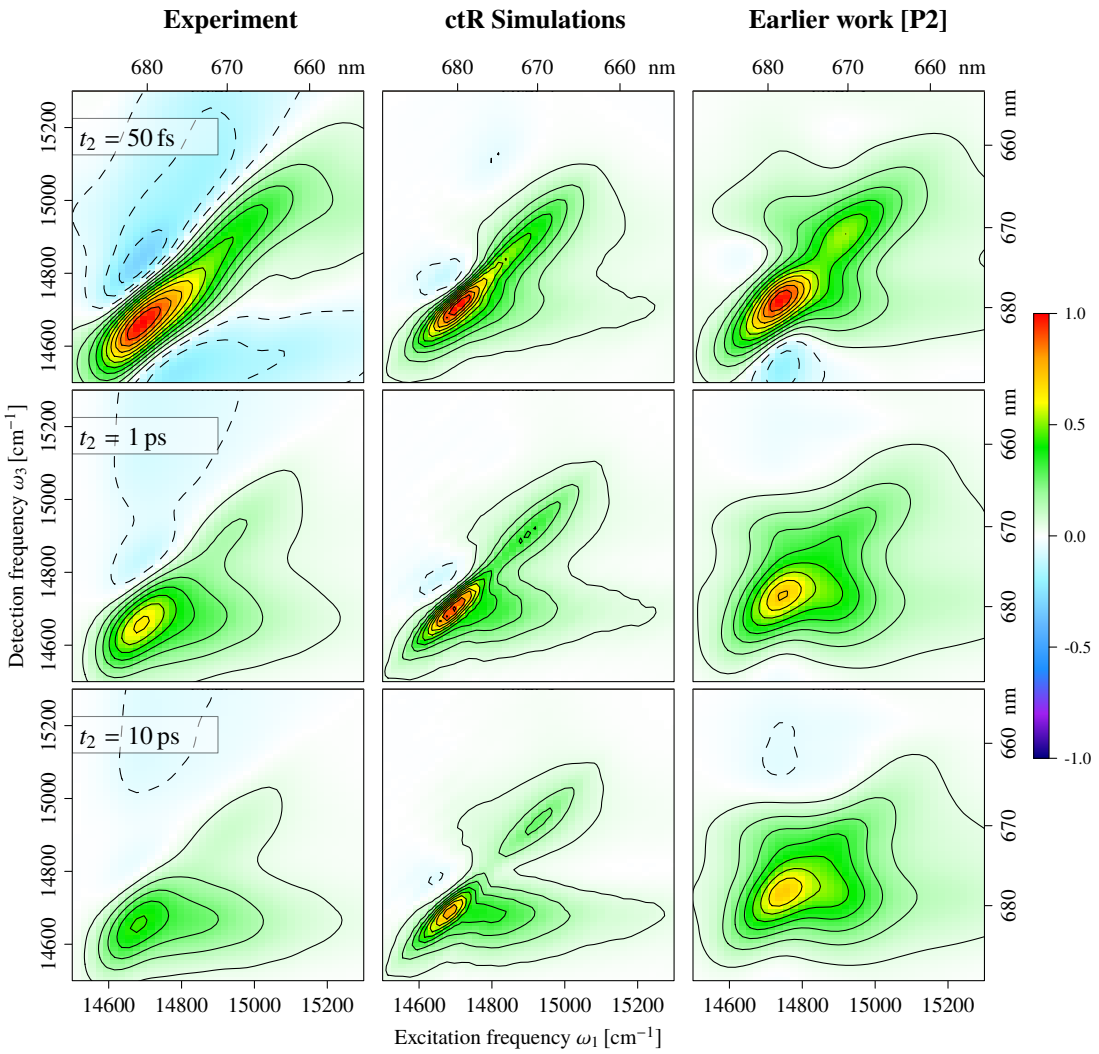

Figure 3.10: Experimental and simulated 2D spectra of the PSII RC at 77 K. Left column shows experimental data, middle column shows calculations based on the model and expressions presented in this thesis (Sections 3.1 and 2.5, respectively), right column shows calculations from our previous work [**P2**], which were based on the modified Redfield theory. Rows correspond to waiting times equal to 50 fs, 1 ps and 10 ps.

N_D axis towards the N_C atom for the static dipole moments of both Chls and Pheos.

3.2.3 2D spectroscopy of PSII RC

In this subsection, we report preliminary calculations of the 2D spectra of the PSII RC based on the model presented in this chapter. We used expressions given in Section 2.5. For simplicity, however, we neglected the CT state and considered only MEs.

Comparison of the simulated spectra with experimental data[1] is presented in Fig. 3.10. Note that the model parameters were not adjusted to fit the 2D spectra better, but just taken from the fits of linear spectra. There we also present our previous calculations, which were based on the mR theory and included several CT states [**P2**].

A few things can be noted. First, our current model does not give the upper cross-peak (at $\omega_1 \approx 14700\,\mathrm{cm}^{-1}$ and $\omega_3 \approx 14900\,\mathrm{cm}^{-1}$), which is absent in experimental data, but is present in calculations based on our previous model. Indeed, in that work [**P2**] the model parameters of the fit were specifically adjusted to fit the 2D spectra, but that upper cross-peak could not be avoided.

Second, the overall peak pattern looks somewhat better in the new simulations, especially considering later waiting times (1 or 10 ps). The peak intensities, however, differ. But that is not surprising, as in our current calculations we did not include any CT states, thus only energy transfer, and not charge separation, was present.

Third, our current model gives smaller homogeneous broadening than is observed in experiment. This implies that the reorganization energy values obtained from the fits of the optical spectra will have to be slightly adjusted.

Thus, our preliminary calculations appear to be an improvement over our previous work. Adjusting the homogeneous broadening and adding CT states to match the experimental kinetics should provide even better agreement with the experimental data.

3.3 Comparison with other models

3.3.1 Site energies

We obtained our site energies from the fit of nine linear spectra, and then verified them by calculating more independent spectra. In this subsection, we will compare our results to other works. We have to note, however, that direct comparison of the site energies can sometimes be misleading, due to the type of spectral density employed and the amount of reorganization energy included in different models. Therefore, comparing the site energies relatively, e. g. between the corresponding pigments of different branches of the RC, is a better approach.

[1] Experiments were performed by S. Seckin Senlik at the lab of Jennifer P. Ogilvie, University of Michigan, USA.

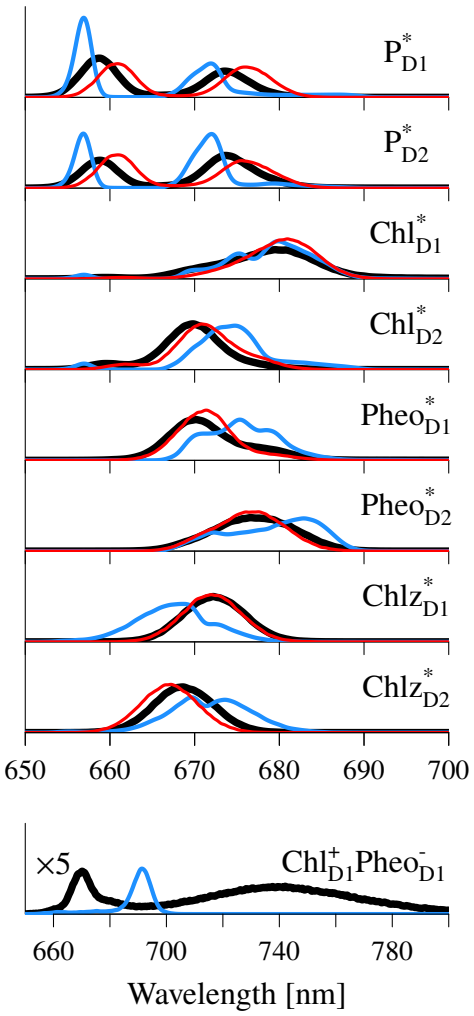

Figure 3.11: The excited state energy distributions showing the energies of the states that each pigment or CT state participate in. See text for more details. Black lines denote the present model, blue lines denote our previous work [**P2**] and red lines denote recent work from Müh *et al.* [119].

Our model finds that the lowest site energy is of the $\mathrm{Chl}_{\mathrm{D1}}$ pigment, in agreement with many previous works [**P2**, 106, 110, 119]. This is consistent with the triplet minus singlet absorption difference spectrum calculations, which can be well described assuming that at low temperatures, the triplet is localized at the $\mathrm{Chl}_{\mathrm{D1}}$ pigment. On the other hand, some works assign a considerably higher energy for this pigment [168, 169]. Our fitting shows that the latter assignment is not consistent with the experimental data.

Another somewhat controversial issue is the assignment of the $\mathrm{Pheo}_{\mathrm{D1/D2}}$ energies. We find that $\mathrm{Pheo}_{\mathrm{D2}}$ has the second lowest energy, while that of $\mathrm{Pheo}_{\mathrm{D1}}$ is considerably higher. This is in general agreement with the findings of Ref. [119], although contrary to other reports in the literature [170].

Since we can accurately reproduce not only absorption difference spectra RC−RC1x/RC2x, but also the absorption difference corresponding to the reduced $\mathrm{Pheo}_{\mathrm{D1}}$ and the CT state $\mathrm{P}^{+}_{\mathrm{D1}}\mathrm{Pheo}^{-}_{\mathrm{D1}}$, we hold that our assignment accurately reflects the system.

In previous work, the energies of the special pair pigments have mostly been found to be the highest of the pigments in the RC [**P2**, 105–107, 110]. Our findings suggest high, but not necessarily the highest energies for these pigments, with $\mathrm{Chl}_{\mathrm{D2}}$ having a similar energy to P_{D1} and $\mathrm{Chlz}_{\mathrm{D2}}$ to P_{D2}. Due to a relatively large resonance coupling between the special pair pigments it is rather difficult to pinpoint their energies from a specific experiment. Having simulated the absorption difference spectra corresponding to the $\mathrm{P}^{+}_{\mathrm{D1}}\mathrm{Pheo}^{-}_{\mathrm{D1}}$ CT state and obtained good agreement with experimental data, our energy for the P_{D1} pigment should be accurate.

Regarding the peripheral chlorophylls, our results are in general agreement with other works [**P2**, 106, 110, 119]. Nonetheless, previous models often suggested very similar energies between the two Chlz molecules, while in the present work we found a somewhat larger energy for $\mathrm{Chlz}_{\mathrm{D2}}$, which suggests that it is the pigment lost in the RC5 preparations [164, 165]. This is in agreement with the assignment from Ref. [119].

A convenient way to compare the site energies is to present the excited state energy distributions that show the energies of the eigenstates in which each pigment or CT state participate. These distributions are defined as:

$$D_A(\omega) = \left\langle \sum_{e}^{N_{\mathrm{tot}}} \left|\psi_{e,A}\right|^2 \delta\left(\omega - \left(\omega_{eg} - \lambda_{ee,ee}\right)\right) \right\rangle_{\mathrm{dis}} . \tag{3.6}$$

Here $\lambda_{ee,ee} = \sum_A \left|\psi_{e,A}\right|^4 \lambda_A$ is the eigenstate reorganization energy. For our model, these distributions are presented in Fig. 3.11. In addition, we also present distributions from our previous model [**P2**] and from Ref. [119], where the energies of the sites were obtained by taking into account electrostatic interactions as calculated from the structural data.

It can be seen that there is good agreement between our current model and that of Ref. [119]. We note that this agreement is because Eq. (3.6) accounts for differences in reorganization energy, thus even though our model has higher state energies it also has larger reorganization energies and the combined result is very similar to Ref. [119]. The only noticeable difference is in the special pigment energy distributions, which are somewhat blueshifted in our model.

On the other hand, the differences between the excited state distributions

of the present model and our previous work [**P2**] are larger, though the overall pattern is somewhat similar. The largest differences are for $\mathrm{Chl}_{\mathrm{D2}}$, $\mathrm{Pheo}_{\mathrm{D1}}$ and both Chlzs. One main difference is that the energy distributions for our previous work show more structure. This is because of the differences in disorder values between both models. Our previous work [**P2**], following previous models based on the mR theory [105–107], assumed about three times smaller disorder than in the current model. Taking into account that presently we used a more advanced lineshape theory, a spectral density suitable for low temperature calculations and that the disorder value that we obtain is very similar to Refs. [110, 111, 119], we believe that our current values are more accurate and that disorder in the previous works [**P2**, 105–107, 130] might have been severely underestimated. These differences in disorder are expected to have significant influence to the time-resolved spectroscopic data and will have to be investigated more closely in the future.

3.3.2 Stark spectrum and CT states

In this thesis we extended the ctR theory to describe the Stark spectrum. This was done using the perturbative expansion in terms of the strength of the static electric field. Our expressions thus significantly improve upon Ref. [106], where the Markovian approximation and the mR lineshapes were used. Even though here we presented only the term corresponding to the RWA, other terms can be easily formulated. Nonetheless, our approach, though straightforward to compute, is computationally expensive, involving a double time integral over a triple sum. This means that it scales rather badly for larger systems. Additionally, the Stark spectrum is sensitive to the CT states and our results indicate that they possess very large disorder. Thus, Stark spectrum calculations need a large number of realizations to converge. We performed our fits with 25000 realizations, and the obtained spectra were still somewhat noisy. The Stark spectra presented in this chapter (Fig. 3.3) were calculated using 600000 realizations. For comparison, 5000 realizations are sufficient to achieve good convergence for the absorption spectrum at 77 K. Although this suggests that our determined CT state parameters might possess some uncertainty, they still should be reasonably accurate.

Several conclusions can be made from our calculations of the Stark spectrum of the PSII RC. First, our results show that CT states influence the Stark spectrum more than was obtained previously [106]. Without the CT states we cannot obtain a reasonable agreement with experimental data. This implies that the

coupling between the ME states and the CT states is somewhat larger than was estimated before [106]. If so, this should affect calculations of the time-resolved spectroscopic data.

Second, our results indicate that *if* the Stark spectrum is mostly influenced by a single CT state, it is probably $\mathrm{Chl}^+_{\mathrm{D1}}\mathrm{Pheo}^-_{\mathrm{D1}}$ rather than $\mathrm{P}^+_{\mathrm{D2}}\mathrm{P}^-_{\mathrm{D1}}$, contrary to what was previously concluded [106]. Although agreement between theory and experiment is poorer with the $\mathrm{P}^+_{\mathrm{D2}}\mathrm{P}^-_{\mathrm{D1}}$ state than with $\mathrm{Chl}^+_{\mathrm{D1}}\mathrm{Pheo}^-_{\mathrm{D1}}$, inclusion of the $\mathrm{P}^+_{\mathrm{D2}}\mathrm{P}^-_{\mathrm{D1}}$ state does provide better agreement than when CT states are neglected entirely. The agreement that we obtain with the single $\mathrm{Chl}^+_{\mathrm{D1}}\mathrm{Pheo}^-_{\mathrm{D1}}$ state (Fig. 3.3a) is good but not excellent. It is likely that instead of a single state, more CT states are coupled to the ME states strongly enough to influence the Stark spectrum. We did not try to fit the experimental Stark spectrum with 2 CT states because the fit would have been very poorly constrained (fitting a single spectrum with eight free parameters). Instead we chose to make separate optimizations with the individual $\mathrm{Chl}^+_{\mathrm{D1}}\mathrm{Pheo}^-_{\mathrm{D1}}$ and $\mathrm{P}^+_{\mathrm{D2}}\mathrm{P}^-_{\mathrm{D1}}$ states. Using the parameters obtained from the individual optimizations, if we include both CT states (see Fig. 3.3c) we obtain improved agreement of the $\sim 680\,\mathrm{nm}$ feature (if compared to Fig. 3.3a) but at a cost of an appearance of a negative feature at $\sim 700\,\mathrm{nm}$.

Third, we have obtained very large disorder of the CT state ($\sigma_{\mathrm{Chl}^+_{\mathrm{D1}}\mathrm{Pheo}^-_{\mathrm{D1}}} = 550\,\mathrm{cm}^{-1}$), which is clearly visible in its energy distribution in Fig. 3.11. Our value of disorder is considerably larger than previous estimates [**P2**, 105–107]. This result is in line with previous suggestions that disorder might control different charge separation pathways in the PSII RC.

Overall, we would like to suggest that calculations of the Stark spectrum of the PSII RC should be made not to extract the values of the system parameters (due to the computational expense), but to constrain them. Thus, models which include a number of CT states needed to calculate the charge separation dynamics [**P2**, 107] should be tested against the experimental Stark spectrum using the level of theory developed in this thesis. Since each CT state necessarily adds a number of parameters to the model, their values could be severely constrained by their sensitivity to the Stark spectrum.

We would also like to draw attention to our calculations of the absorption difference spectra corresponding to the CT state $\mathrm{P}^+_{\mathrm{D1}}\mathrm{Pheo}^-_{\mathrm{D1}}$ at different temperatures (Fig. 3.9). The good agreement between theory and experiment implies that even at room temperature the relaxed pump–probe spectra correspond to this specific state. Therefore, the energy gap between this state and all the other

CT states should be relatively large, a few times more than the thermal energy at room temperature. This information should be useful in simulating time-resolved spectroscopic data.

3.4 Effect of vibrations to charge transfer

In Ref. [**P4**] a very high quality of 2D data on the PSII RC was reported, where an excellent signal-to-noise ratio allowed to reveal highly oscillatory nature of the spectral features. Oscillations in the 2D data were a hot topic for quite some time, as in a Nature paper by Engel *et al*. in 2007 [13] the data on the FMO complex from purple bacteria were presented, showing oscillatory features. It was suggested, though without theoretical calculations, that energy might travel through the FMO in wavelike manner, utilizing the electronic quantum coherence. Even though in later years the focus shifted more on vibrational coherences [134, 171, 172], the general question remained – can either vibrational or electronic coherences influence energy transfer in a biological molecular system?

For this reason, the findings of Ref. [**P4**] were of particular interest, as in the PSII RC not only energy, but charge transfer occurs. Thus, the question turned to whether or not coherence can influence *charge* separation?

From the analysis of the 2D data it was demonstrated that major oscillation frequencies corresponded to 91, 127, 251, 337 and 730 cm^{-1}. Simulations in terms of the so-called Fourier maps [171] demonstrated that the oscillatory features corresponding to 91, 251, 337 and 730 cm^{-1} were mostly related to vibrational effects, while that of 127 cm^{-1} was due to vibronic (combined electron-vibrational) effects.

To qualitatively investigate the effects of underdamped vibrations to the charge transfer dynamics, we performed calculations of the density operator evolution for a three state system – two states represent the special pair molecular excitations and the last corresponds to the $\mathrm{P}^{+}_{\mathrm{D2}}\mathrm{P}^{-}_{\mathrm{D1}}$ CT state. The energies and couplings were taken from Ref. [**P2**], but we reduced the coupling between the special pair molecules to 120 cm^{-1} in the present modeling. The system Hamiltonian is (in cm^{-1}):

$$\hat{H}_{\mathrm{S}} = \begin{pmatrix} 15280 & 120 & 45 \\ 120 & 15210 & 45 \\ 45 & 45 & 15200 \end{pmatrix}. \tag{3.7}$$

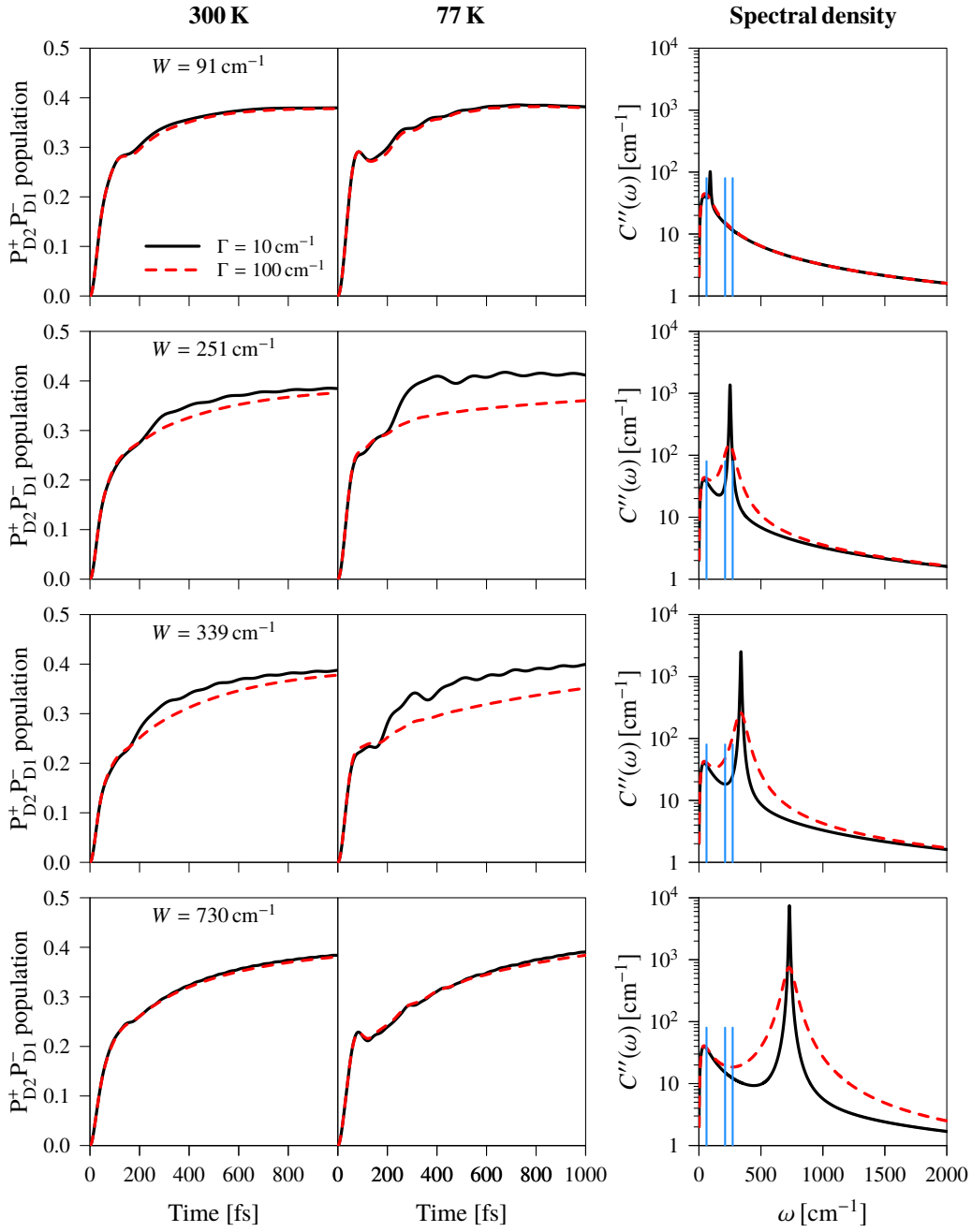

Figure 3.12: Evolutions of the $P^{+}_{D2}P^{-}_{D1}$ CT state population with different spectral densities (shown in the last column) including single vibrational modes at frequencies 91 cm^{-1} (first row), 251 cm^{-1} (second row), 339 cm^{-1} (third row), and 730 cm^{-1} (last row). Simulations were performed for the special pair heterodimer and $P^{+}_{D2}P^{-}_{D1}$ state included in the model. Population evolution was calculated using the HEOM theory. Red lines denote incoherent (strongly damped) mode and black line denotes coherent (weakly damped) mode. Blue lines in the figures of spectral density mark optical excitonic splittings (at 272 cm^{-1}, 211 cm^{-1} and 61 cm^{-1}).

Each state is coupled to a two mode environment, thus the spectral density is

$$C''(\omega) = \frac{2\lambda_L \gamma \omega}{\omega^2 + \gamma^2} + \frac{2\lambda_H \omega W^2 \Gamma}{\left(\omega^2 - W^2\right)^2 + \Gamma^2 \omega^2}. \tag{3.8}$$

The first mode corresponds to Debye spectral density and its parameters are $\lambda_L = 40\,\mathrm{cm}^{-1}$ and $\gamma = 40\,\mathrm{cm}^{-1}$ as in Ref. [**P2**]. The second mode corresponds to coupling with specific frequency vibration. Its damping parameter is either $\Gamma = 10\,\mathrm{cm}^{-1}$, representing weakly damped vibration, or $\Gamma = 100\,\mathrm{cm}^{-1}$, representing strongly damped vibration. Following the experimental data, we performed calculations for four vibrational modes. The reorganization energies for the specific modes were based on the Huang-Rhys factors of specific modes in Ref. [105]. obtained from the FLN data. For $W = 91\,\mathrm{cm}^{-1}$ mode we have $\lambda_H = 4\,\mathrm{cm}^{-1}$ (based on 97 cm^{-1} mode from FLN), for $W = 251\,\mathrm{cm}^{-1}$ we have $\lambda_H = 27\,\mathrm{cm}^{-1}$ (based on 213 and 260 cm^{-1} modes from FLN), for $W = 339\,\mathrm{cm}^{-1}$ we have $\lambda_H = 37\,\mathrm{cm}^{-1}$ (based on 298, 342 and 388 cm^{-1} modes from FLN) and for $W = 730\,\mathrm{cm}^{-1}$ we have $\lambda_H = 51\,\mathrm{cm}^{-1}$ (based on 700, 722, 742, 752 and 795 cm^{-1} modes from FLN). Additionally, CT state has 1.5 times bigger reorganization energy as in Ref. [**P2**].

We calculate density operator evolution using the HEOM approach [173], which is exact for a Gaussian bath. We thus avoid perturbative calculations and can be sure that our results are correct for all the parameters used.

All calculated evolutions of the CT state populations and corresponding spectral densities are presented in Fig. 3.12. The main results are the following. First, the 91 cm^{-1} vibrational mode has very little effect to the charge separation dynamics, as it has very small reorganization energy. Second, for both 251 and 339 cm^{-1} vibrations, we can observe different evolutions, depending on the nature of the vibrational mode. If the mode is weakly damped, sudden increases in CT state populations can be observed. In both of these cases the vibrational frequency is close to the excitonic resonances in the system. Note that the observed effect is stronger for 77 K, which is not surprising, since coherences survive longer at lower temperatures. For vibrational mode of 730 cm^{-1}, no such speed up is observed, which should be related to the fact that this frequency is not close enough to any excitonic resonance.

The observed speed up effect is not a simple transfer rate increase, which would be expected from the traditional Redfield transfer rate formula, which says that the transfer rate is proportional to the value of spectral density at frequency, corresponding to the energy difference between the states, see Eq. (2.49). We should emphasize that the Redfield formula is dependent on the Markov ap-

proximation, which is valid, when the bath relaxes much slower than all the timescales of system dynamics. In case of long lived coherent vibration, this assumption is not true, and conversely, the Redfield formula does not give an accurate picture of transfer rates.

3.5 Conclusions

In this chapter, we revisited the spectroscopic properties of the PSII RC using the ctR theory for optical lineshapes. We constructed a model based on the tight-binding Hamiltonian (based on the theory of Chapter 2), including a single CT state. The parameters of the model were obtained by fitting nine linear spectra (absorption, LD and CD), and then further tested by calculations of other independent spectra. Our simulations are in a good to excellent agreement with all the calculated spectra. The parameter values of our model differ from previous models based on the mR theory and are mostly in agreement with recent structure based estimations, which accounted for the electrostatic effects.

Additionally, we used the ctR theory expressions, derived in Section 2.4 to calculate the Stark spectrum of the PSII RC. Comparison with experimental data leads to the **third statement of the thesis**: By using the ctR theory the characteristics of the PSII RC were determined from a fit of multiple spectroscopic data. The primary CT state is identified to be $\mathrm{Chl}^{+}_{\mathrm{D1}}\mathrm{Pheo}^{-}_{\mathrm{D1}}$ from the fits of the Stark spectrum.

We also presented some preliminary calculations of the 2D spectra of the PSII RC, using our model and the ctR theory expressions given in Section 2.5. Our resent results appear to better match the experimental data than our previous model, but to improve the agreement even more additional steps are needed, which were identified.

Finally, we reported a proof of concept demonstrations of how the presence of vibrations could influence the rate of charge separation in the PSII RC. It was found that noticeable effects can be obtained only when the frequency of vibration is close to the energy gaps in the system. Nonetheless, the mechanism is not of Redfield type, as exact resonance conditions are not needed.

Most of this chapter is based on [**p9**], with results often compared to [**P2**]. Section 3.4 is adapted from the author's contributions to [**P4**].

Afterword

> Thou wilt say it brought me good luck and victory in battle.
> But it brought not to me, as to Zeldornius, this last best
> luck of all: that earth should gape for me when my great
> deeds were ended.
>
> LORD BRANDOCH DAHA in "The Worm Ouroboros"
> by E. R. Eddison

In this thesis, several things were accomplished. First, a pedagogical introduction to the 2D optical spectroscopy was made, followed with a report on the analysis of the experimental 2D spectroscopy data of the FCP complex, a major light-harvesting antenna from diatoms. Second, a tight-binding Hamiltonian was presented and the ctR theory was developed to describe linear and non-linear optical spectra of photosynthetic molecular complexes. Third, the ctR theory then was applied to construct a microscopic model of the PSII RC.

This thesis is not unified by a single system, a single spectroscopic technique or even a single theoretical approach. Instead, at least, according to the author's perspective, this thesis shows a unity of purpose. Methods, theories, techniques, and even concrete systems are but tools. The real goal is learning. The real purpose is to enrich the knowledge of oneself and of mankind even with a tiny bit. Whether the author succeeded in that, let the reader judge.

Appendix A

Cumulant expansion

Cumulant expansion is a specific form of a resummation technique, which allows one to estimate higher order terms from lower order terms. It is mostly used in probability theory [174], but it can be applied for any function. Consider a function $A(x)$ which we expand in powers of x:

$$A(x) = A_0 (1 + A_1 x + A_2 x + \dots). \tag{A.1}$$

Alternatively, we can make an exponential ansatz

$$A(x) = A_0 \exp(F(x)) \tag{A.2}$$

and expand function $F(x)$:

$$F(x) = F_1 x + F_2 x^2 + \dots \tag{A.3}$$

Then we have

$$\begin{aligned} A(x) &= A_0 \exp\left(F_1 x + F_2 x^2 + \dots\right) \\ &= A_0 \left(1 + F_1 x + F_2 x^2 + \frac{1}{2}\left(F_1 x + F_2 x^2\right)^2 + \dots\right) \\ &= A_0 \left(1 + F_1 x + \left(F_2 + \frac{1}{2} F_1^2\right) x^2 + \dots\right). \end{aligned} \tag{A.4}$$

In this way, we establish relationships between the coefficients of different expansions:

$$F_1 = A_1; \tag{A.5}$$

$$F_2 = A_2 - \frac{1}{2} A_1^2. \tag{A.6}$$

With this, a second order cumulant expansion of $A(x)$ would be

$$A^{2c}(x) = A_0 \exp\left(A_1 x + \left(A_2 - \frac{1}{2} A_1^2\right) x^2\right). \tag{A.7}$$

So, by performing the cumulant expansion we approximate the higher order terms from the Taylor expansion.

Now we turn to the second order cumulant expansion of Eq. (2.42), which we repeat here for convenience:

$$\varphi_{e_1}(t) = \mathrm{Tr}_\mathrm{B}\left[\mathrm{e}^{\mathrm{i}\hat{H}_\mathrm{B}t}\langle e_1|\mathrm{e}^{-\mathrm{i}\hat{H}t}|e_1\rangle\hat{\rho}_\mathrm{B}^\mathrm{eq}\right]. \tag{A.8}$$

First, we rewrite the matrix element of the evolution operator as

$$\begin{aligned}\langle e_1|\mathrm{e}^{-\mathrm{i}\hat{H}t}|e_1\rangle &= \langle e_1|\mathrm{e}^{-\mathrm{i}\left(\hat{H}_\mathrm{S}+\hat{H}_\mathrm{B}\right)t}\exp_+\left(-\mathrm{i}\int_0^t \mathrm{d}\tau\hat{H}_\mathrm{SB}^\mathrm{I}(\tau)\right)|e_1\rangle. \\ &= \mathrm{e}^{-\varepsilon_{e_1}t}\mathrm{e}^{-\mathrm{i}\hat{H}_\mathrm{B}t}\langle e_1|\exp_+\left(-\mathrm{i}\int_0^t \mathrm{d}\tau\hat{H}_\mathrm{SB}^\mathrm{I}(\tau)\right)|e_1\rangle\end{aligned} \tag{A.9}$$

Here the positive time ordered exponential is defined by its expansion [86]:

$$\begin{aligned}\exp_+\left(-\mathrm{i}\int_0^t \mathrm{d}\tau\hat{H}_\mathrm{SB}^\mathrm{I}(\tau)\right) = \hat{I} - \mathrm{i}\int_0^t \mathrm{d}\tau\hat{H}_\mathrm{SB}^\mathrm{I}(\tau) \\ - \int_0^t \mathrm{d}\tau_2\int_0^{\tau_2}\mathrm{d}\tau_1\hat{H}_\mathrm{SB}^\mathrm{I}(\tau_2)\,\hat{H}_\mathrm{SB}^\mathrm{I}(\tau_1) + \ldots\end{aligned} \tag{A.10}$$

Thus,

$$\begin{aligned}\varphi_{e_1}(t) = \mathrm{e}^{-\varepsilon_{e_1}t}\mathrm{Tr}_\mathrm{B}\Bigg[&\langle e_1|\hat{I}|e_1\rangle \\ &- \mathrm{i}\int_0^t \mathrm{d}\tau\langle e_1|\hat{H}_\mathrm{SB}^\mathrm{I}(\tau)|e_1\rangle \\ &- \int_0^t \mathrm{d}\tau_2\int_0^{\tau_2}\mathrm{d}\tau_1\langle e_1|\hat{H}_\mathrm{SB}^\mathrm{I}(\tau_2)\,\hat{H}_\mathrm{SB}^\mathrm{I}(\tau_1)|e_1\rangle + \ldots\Bigg] \\ = \mathrm{e}^{-\varepsilon_{e_1}t}\mathrm{Tr}_\mathrm{B}\Bigg[&\hat{I}_\mathrm{B} \\ &- \mathrm{i}\int_0^t \mathrm{d}\tau\hat{F}_{e_1e_1}^\mathrm{I}(\tau) \\ &- \int_0^t \mathrm{d}\tau_2\int_0^{\tau_2}\mathrm{d}\tau_1\hat{F}_{e_1e_1}^\mathrm{I}(\tau_2)\,\hat{F}_{e_1e_1}^\mathrm{I}(\tau_1) +\end{aligned}$$

$$
\begin{aligned}
&\quad - \sum_{e_2 \neq e_1}^{N_{\mathrm{tot}}} \int_0^t \mathrm{d}\tau_2 \int_0^{\tau_2} \mathrm{d}\tau_1 \mathrm{e}^{\mathrm{i}\omega_{e_1 e_2}(\tau_2-\tau_1)} \hat{F}^{\mathrm{I}}_{e_1 e_2}(\tau_2)\, \hat{F}^{\mathrm{I}}_{e_2 e_1}(\tau_1) + \dots \Bigg] \\
&= \mathrm{e}^{-\varepsilon_{e_1} t} \Bigg(1 - 0 \\
&\quad - \int_0^t \mathrm{d}\tau_2 \int_0^{\tau_2} \mathrm{d}\tau_1 C_{e_1 e_1, e_1 e_1}(\tau_2 - \tau_1) \\
&\quad - \sum_{e_2 \neq e_1}^{N_{\mathrm{tot}}} \int_0^t \mathrm{d}\tau_2 \int_0^{\tau_2} \mathrm{d}\tau_1 \mathrm{e}^{\mathrm{i}\omega_{e_1 e_2}(\tau_2-\tau_1)} C_{e_1 e_2, e_2 e_1}(\tau_2 - \tau_1) + \dots \Bigg) \\
&= \mathrm{e}^{-\varepsilon_{e_1} t} \left(1 - g_{e_1 e_1, e_1 e_1}(t) - \xi_{e_1}(t) + \dots \right) \\
&= \exp\left(-\varepsilon_{e_1} t - g_{e_1 e_1, e_1 e_1}(t) - \xi_{e_1}(t) \right). \qquad \text{(A.11)}
\end{aligned}
$$

In these lines we used Eqs. (2.22), (2.13), (2.21), (2.23) and (2.44). In the last equality, the second order cumulant expansion was performed (thus it should not be an equality in a strict sense).

Cumulant expansion of the response functions corresponding to the Stark spectra (Section (2.4)) and the 2D spectra (Section (2.5)) are performed in the same manner, just more terms are obtained. In those derivations a few more expressions are needed. First, we need a property of trace operation:

$$
\left(\mathrm{Tr}\left(\hat{A} \right) \right)^* = \mathrm{Tr}\left(\hat{A}^\dagger \right). \qquad \text{(A.12)}
$$

Second, a more complicated double time integral over the correlation function is

$$
\begin{aligned}
&\int_{t_3}^{t_4} \mathrm{d}\tau_2 \int_{t_1}^{t_2} \mathrm{d}\tau_1 C(\tau_2 - \tau_1 + T) = \\
&\qquad g(t_3 + T - t_2) - g(t_3 + T - t_1) - g(t_4 + T - t_2) + g(t_4 + T - t_1). \qquad \text{(A.13)}
\end{aligned}
$$

Additionally, the lineshape function of negative times can be expressed as

$$
g_{\alpha\beta,\gamma\delta}(-t) = g^*_{\gamma\delta,\alpha\beta}(t). \qquad \text{(A.14)}
$$

Finally, there is the symmetry of the lineshape function indices:

$$
g_{\alpha\beta,\gamma\delta}(t) = g_{\beta\alpha,\gamma\delta}(t) = g_{\alpha\beta,\delta\gamma}(t) = g_{\beta\alpha,\delta\gamma}(t). \qquad \text{(A.15)}
$$

Bibliography

[1] R. E. Blankenship, *Molecular Mechanisms of Photosynthesis*, 2nd edition (Wiley Blackwell, Chichester, 2014).

[2] A. V. Ruban, *The Photosynthetic Membrane: Molecular Mechanisms and Biophysics of Light Harvesting* (Wiley, Chichester, 2013).

[3] P. Hannaford, ed., *Femtosecond Laser Spectroscopy* (Springer, New York, 2005).

[4] W. W. Parson, *Modern Optical Spectroscopy*, 2nd edition (Springer-Verlag, Berlin, 2015).

[5] M. G. Rockley, M. W. Windsor, R. J. Cogdell, and W. W. Parson, Proc. Natl. Acad. Sci. U. S. A. **72**, 2251–2255, 1975.

[6] D. Holten and M. W. Windsor, Annu. Rev. Biophys. Bioeng. **7**, 189–227, 1978.

[7] V. Shuvalov, A. Klevanik, A. Sharkov, P. Kryukov, and K. Bacon, FEBS Lett. **107**, 313–316, 1979.

[8] N. W. Woodbury, M. Becker, D. Middendorf, and W. W. Parson, Biochemistry **24**, 7516–7521, 1985.

[9] M. R. Wasielewski, D. G. Johnson, M. Seibert, and Govindjee, Proc. Natl. Acad. Sci. U. S. A. **86**, 524–528, 1989.

[10] S. Hess, M. Chachisvilis, K. Timpmann, M. R. Jones, G. J. Fowler, C. N. Hunter, and V. Sundström, Proc. Natl. Acad. Sci. U. S. A. **92**, 12333–12337, 1995.

[11] D. M. Jonas, Annu. Rev. Phys. Chem. **54**, 425–463, 2003.

[12] T. Brixner, J. Stenger, H. M. Vaswani, M. Cho, R. E. Blankenship, and G. R. Fleming, Nature **434**, 625–628, 2005.

[13] G. S. Engel, T. R. Calhoun, E. L. Read, T. K. Ahn, T. Mančal, Y. C. Cheng, R. E. Blankenship, and G. R. Fleming, Nature **446**, 782–786, 2007.

[14] J. A. Myers, K. L. M. Lewis, F. D. Fuller, P. F. Tekavec, C. F. Yocum, and J. P. Ogilvie, J. Phys. Chem. Lett. **1**, 2774–2780, 2010.

[15] J. Dostál, T. Mančal, R. Augulis, F. Vácha, J. Pšenčik, and D. Zigmantas, J. Am. Chem. Soc. **134**, 11611–11617, 2012.

[16] E. Harel and G. S. Engel, Proc. Natl. Acad. Sci. U. S. A. **109**, 706–711, 2012.

[17] J. M. Anna, E. E. Ostroumov, K. Maghlaoui, J. Barber, and G. D. Scholes, J. Phys. Chem. Lett. **3**, 3677–3684, 2012.

[18] G. S. Schlau-Cohen, A. Ishizaki, T. R. Calhoun, N. S. Ginsberg, M. Ballottari, R. Bassi, and G. R. Fleming, Nat. Chem. **4**, 389–395, 2012.

[19] E. Romero, R. Augulis, V. I. Novoderezhkin, M. Ferretti, J. Thieme, D. Zigmantas, and R. V. Grondelle, Nat. Phys. **10**, 676–682, 2014.

[20] P. Tian, D. Keusters, Y. Suzaki, and W. S. Warren, Science **300**, 1553–1555, 2003.

[21] S. T. Cundiff, J. Opt. Soc. Am. B **29**, A69–A81, Feb. 2012.

[22] S. Ruetzel, M. Diekmann, P. Nuernberger, C. Walter, B. Engels, and T. Brixner, Proc. Natl. Acad. Sci. U. S. A. **111**, 4764–4769, 2014.

[23] J. R. Lakowicz, *Principles of Fluorescence Spectroscopy*, 3rd edition (Springer, New York, 2011).

[24] M. Pope and C. E. Swenberg, *Electron Processes in Organic Crystals* (Oxford University Press, New York/Oxford, 1999).

[25] H. van Amerongen, L. Valkunas, and R. van Grondelle, *Photosynthetic Excitons* (World Scientific, Singapore, 2000).

[26] J. Jortner, M. Bixon, T. Langenbacher, and M. E. Michel-Beyerle, Proc. Natl. Acad. Sci. U. S. A. **95**, 12759–12765, 1998.

[27] J.-L. Brédas, D. Beljonne, V. Coropceanu, and J. Cornil, Chem. Rev. **104**, 4971–5004, 2004.

[28] U. Weiss, *Quantum Dissipative System*, 3rd edition (World Scientific, Singapore, 2008).

[29] H.-P. Breuer and F. Petruccione, *The theory of open quantum systems* (Oxford University Press, New York, 2002).

[30] V. May and O. Kühn, *Charge and Energy Transfer Dynamics in Molecular Systems*, 2nd edition (Wiley-VCH, Weinheim, 2011).

[31] L. Valkunas, D. Abramavicius, and T. Mančal, *Molecular Excitation Dynamics and Relaxation: Quantum Theory and Spectroscopy* (Wiley-VCH, Berlin, 2013).

[32] J. Deisenhofer, O. Epp, K. Miki, R. Huber, and H. Michel, J. Mol. Biol. **180**, 385–398, 1984.

[33] J. Koepke, X. Hu, C. Muenke, K. Schulten, and H. Michel, Structure **4**, 581–597, 1996.

[34] N. Kamiya and J.-R. Shen, Proc. Natl. Acad. Sci. U. S. A. **100**, 98–103, 2003.

[35] A. Ben-Shem, F. Frolow, and N. Nelson, Nature **426**, 630–635, 2003.

[36] Z. Liu, H. Yan, K. Wang, T. Kuang, J. Zhang, L. Gui, X. An, and W. Chang, Nature **428**, 287–292, 2004.

[37] Y. Umena, K. Kawakami, J.-R. Shen, and N. Kamiya, Nature **473**, 55–60, 2011.

[38] X. Wei, X. Su, P. Cao, X. Liu, W. Chang, M. Li, X. Zhang, and Z. Liu, Nature **534**, 69–74, 2016.

[39] T. Renger, Photosynth. Res. **102**, 471–485, 2009.

[40] E. Papagiannakis, I. H. M. van Stokkum, H.Fey, C. Büchel, and R. van Grondelle, Photosynth. Res. **86**, 241–50, 2005.

[41] N. Gildenhoff, J. Herz, K. Gundermann, C. Büchel, and J. Wachtveitl, Chem. Phys. **373**, 104–109, 2010.

[42] N. Gildenhoff, S. Amarie, K. Gundermann, A. Beer, C. Büchel, and J. Wachtveitl, Biochim. Biophys. Acta **1797**, 543–549, 2010.

[43] D. Kosumi, M. Kita, R. Fujii, M. Sugisaki, N. Oka, Y. Takaesu, T. Taira, M. Iha, and H. Hashimoto, J. Phys. Chem. Lett. **3**, 2659–2664, 2012.

[44] L. Chen, R. Zheng, Q. Shi, and Y. J. Yan, J. Chem. Phys. **131**, 094502, 2009.

[45] J. Ma and J. Cao, J. Chem. Phys. **142**, 094106, 2015.

[46] K. Ohta, M. Yang, and G. R. Fleming, J. Chem. Phys. **115**, 7609–7621, 2001.

[47] T. Renger and R. A. Marcus, J. Chem. Phys. **116**, 9997–10019, 2002.

[48] M. Yang, J. Chem. Phys. **123**, 124705, 2005.

[49] M. Schröder, U. Kleinekathöfer, and M. Schreiber, J. Chem. Phys. **124**, 084903, 2006.

[50] M. Schröder, M. Schreiber, and U. Kleinekathöfer, J. Lumin. **125**, 126–132, 2007.

[51] T. Mančal, V. Balevičius, and L. Valkunas, J. Phys. Chem. A **115**, 3845–3858, 2011.

[52] L. Banchi, G. Costagliola, A. Ishizaki, and P. Giorda, J. Chem. Phys. **138**, 184107, 2013.

[53] T.-C. Dinh and T. Renger, J. Chem. Phys. **142**, 034104, 2015.

[54] S. R. Greenfield and M. R. Wasielewski, Photosynth. Res. **48**, 83–97, 1996.

[55] J. Dekker and R. Van Grondelle, Photosynth. Res. **63**, 195–208, 2000.

[56] B. A. Diner and F. Rappaport, Annu. Rev. Plant Biol. **53**, 551–580, 2002.

[57] F. Rappaport and B. A. Diner, Coord. Chem. Rev. **252**, 259–272, 2008.

[58] G. Renger and T. Renger, Photosynth. Res. **98**, 53–80, 2008.

[59] S. Vassiliev and D. Bruce, Photosynth. Res. **97**, 75–89, 2008.

[60] T. Renger and E. Schlodder, J. Photochem. Photobiol. B: Biol. **104**, 126–141, 2011.

[61] H. van Amerongen and R. Croce, Photosynth. Res. **116**, 251–263, 2013.

[62] F. D. Fuller and J. P. Ogilvie, Annu. Rev. Phys. Chem. **66**, 667–690, 2015.

[63] J. A. Myers, K. L. Lewis, P. F. Tekavec, and J. P. Ogilvie, Opt. Express **16**, 17420–17428, 2008.

[64] M. Cho, *Two-Dimensional Optical Spectroscopy* (CRC Press, Boca Raton, 2009).

[65] P. Hamm and M. Zanni, *Concepts and Methods of 2D Infrared Spectroscopy* (Cambridge University Press, New York, 2011).

[66] D. Brida, C. Manzoni, and G. Cerullo, Opt. Lett. **37**, 3027–3029, 2012.

[67] H. Zheng, J. R. Caram, P. D. Dahlberg, B. S. Rolczynski, S. Viswanathan, D. S. Dolzhnikov, A. Khadivi, D. V. Talapin, and G. S. Engel, Appl. Opt. **53**, 1909–1917, 2014.

[68] I. H. van Stokkum, D. S. Larsen, and R. van Grondelle, Biochim. Biophys. Acta **1657**, 82–104, 2004.

[69] E. E. Ostroumov, R. M. Mulvaney, J. M. Anna, R. J. Cogdell, and G. D. Scholes, J. Phys. Chem. B **117**, 11349–11362, 2013.

[70] J. Alster, H. Lokstein, J. Dostál, A. Uchida, and D. Zigmantas, J. Phys. Chem. B **118**, 3524–3531, 2014.

[71] P. G. Falkowski, R. T. Barber, and V. Smetacek, Science **281**, 200–206, 1998.

[72] C. B. Field, M. J. Behrenfeld, J. T. Randerson, and P. Falkowski, Science **281**, 237–240, 1998.

[73] D. G. Mann, Phycologia **38**, 437–495, 1999.

[74] C. Büchel, Biochemistry **42**, 13027–13034, 2003.

[75] R. Croce and H. van Amerongen, Nat. Chem. Biol. **10**, 492–501, 2014.

[76] B. Grabowski, F. X. Cunningham, and E. Gantt, Proc. Natl. Acad. Sci. U. S. A. **98**, 2911–2916, 2001.

[77] M. Eppard and E. Rhiel, English, Mol. Gen. Genet. **260**, 335–345, 1998.

[78] L. Premvardhan, B. Robert, A. Beer, and C. Büchel, Biochim. Biophys. Acta **1797**, 1647–1656, 2010.

[79] F. Milota, J. Sperling, A. Nemeth, D. Abramavicius, S. Mukamel, and H. F. Kauffmann, J. Chem. Phys. **131**, 054510, 2009.

[80] A. Kell, X. Feng, M. Reppert, and R. Jankowiak, J. Phys. Chem. B **117**, 7317–7323, 2013.

[81] D. Abramavicius, L. Valkunas, and S. Mukamel, Europhys. Lett. **80**, 17005, 2007.

[82] A. Ishizaki and G. R. Fleming, J. Chem. Phys. **130**, 234111, 2009.

[83] A. Gelzinis, D. Abramavicius, and L. Valkunas, Phys. Rev. B **84**, 245430, 2011.

[84] V. Balevičius Jr., A. Gelzinis, D. Abramavicius, and L. Valkunas, J. Phys. Chem. B **117**, 11031–11041, 2013.

[85] V. Balevičius Jr., A. Gelzinis, D. Abramavicius, T. Mančal, and L. Valkunas, Chem. Phys. **404**, 94–102, 2012.

[86] S. Mukamel, *Principles of Nonlinear Optical Spectroscopy* (Oxford University Press, New York, 1995).

[87] D. Abramavicius, B. Palmieri, D. V. Voronine, F. Šanda, and S. Mukamel, Chem. Rev. **109**, 2350–2408, 2009.

[88] N. Metropolis, A. W. Rosenbluth, M. N. Rosenbluth, A. H. Teller, and E. Teller, J. Chem. Phys. **21**, 1087–1092, 1953.

[89] J. Chmeliov, W. P. Bricker, C. Lo, E. Jouin, L. Valkunas, A. V. Ruban, and C. D. P. Duffy, Phys. Chem. Chem. Phys. **17**, 15857–15867, 2015.

[90] M. Yang and G. R. Fleming, Chem. Phys. **275**, 355–372, 2002.

[91] C. C. Gradinaru, A. A. Pascal, F. van Mourik, B. Robert, P. Horton, R. van Grondelle, and H. van Amerongen, Biochemistry **37**, 1143–1149, 1998.

[92] X. Pan, M. Li, T. Wan, L. Wang, C. Jia, Z. Hou, X. Zhao, J. Zhang, and W. Chang, Nat. Struct. Mol. Biol. **18**, 309–315, 2011.

[93] S. Akimoto, A. Teshigahara, M. Yokono, M. Mimuro, R. Nagao, and T. Tomo, Biochim. Biophys. Acta **1837**, 1514–1521, 2014.

[94] M. Kullmann, S. Ruetzel, J. Buback, P. Nuernberger, and T. Brixner, J. Am. Chem. Soc. **133**, 13074–13080, 2011.

[95] N. Krebs, I. Pugliesi, J. Hauer, and E. Riedle, New J. Phys. **15**, 085016, 2013.

[96] Fuller, F. D. and Ogilvie, J. P., EPJ Web of Conferences **41**, 08018, 2013.

[97] F. Milota, V. I. Prokhorenko, T. Mancal, H. von Berlepsch, O. Bixner, H. F. Kauffmann, and J. Hauer, J. Phys. Chem. A **117**, 6007–6014, 2013.

[98] R. Byrd, P. Lu, J. Nocedal, and C. Zhu, SIAM J. Sci. Comput. **16**, 1190–1208, 1995.

[99] R Development Core Team, *R: A Language and Environment for Statistical Computing*, R Foundation for Statistical Computing (Vienna, Austria, 2015).

[100] L. Premvardhan, L. Bordes, A. Beer, C. Büchel, and B. Robert, J. Phys. Chem. B **113**, 12565–12574, 2009.

[101] D. Abramavicius and S. Mukamel, J. Chem. Phys. **133**, 184501, 2010.

[102] M. Hoffmann, K. Schmidt, T. Fritz, T. Hasche, V. Agranovich, and K. Leo, Chem. Phys. **258**, 73–96, 2000.

[103] N. J. Hestand, R. V. Kazantsev, A. S. Weingarten, L. C. Palmer, S. I. Stupp, and F. C. Spano, J. Am. Chem. Soc. **138**, 11762–11774, 2016.

[104] R. Tempelaar and D. R. Reichman, J. Chem. Phys. **146**, 174703, 2017.

[105] V. I. Novoderezhkin, E. G. Andrizhiyevskaya, J. P. Dekker, and R. van Grondelle, Biophys. J. **89**, 1464–1481, 2005.

[106] V. I. Novoderezhkin, J. P. Dekker, H. van Amerongen, and R. van Grondelle, Biophys. J. **93**, 1293–1311, 2007.

[107] V. I. Novoderezhkin, E. Romero, J. P. Dekker, and R. van Grondelle, ChemPhysChem **12**, 681–688, 2011.

[108] J. Rammer, *Quantum Field Theory of Non-eqilibrium States* (Cambridge University Press, New York, 2007).

[109] S. S. Andrews, J. Chem. Educ. **81**, 877, 2004.

[110] G. Raszweski, W. Saenger, and T. Renger, Biophys. J. **88**, 986–998, 2005.

[111] G. Raszewski, B. A. Diner, E. Schlodder, and T. Renger, Biophys. J. **95**, 105–119, 2008.

[112] T. Renger, M. E. Madjet, F. Müh, I. Trostmann, F.-J. Schmitt, C. Theiss, H. Paulsen, H. J. Eichler, A. Knorr, and G. Renger, J. Phys. Chem. B **113**, 9948–9957, 2009.

[113] W. M. Zhang, T. Meier, V. Chernyak, and S. Mukamel, J. Chem. Phys. **108**, 7763–7774, 1998.

[114] V. I. Novoderezhkin, M. A. Palacios, H. van Amerongen, and R. van Grondelle, J. Phys. Chem. B **108**, 10363–10375, 2004.

[115] G. Garab and H. van Amerongen, Photosynth. Res. **101**, 135–146, 2009.

[116] D. Abramavicius and S. Mukamel, J. Chem. Phys. **122**, 134305, 2005.

[117] D. Lindorfer, F. Müh, and T. Renger, Phys. Chem. Chem. Phys. **19**, 7524–7536, 2017.

[118] J. Hu, R. X. Xu, and Y. Yan, J. Chem. Phys. **133**, 101106, 2010.

[119] F. Müh, M. Plöckinger, and T. Renger, J. Phys. Chem. Lett. **8**, 850–858, 2017.

[120] G. Ritschel and A. Eisfeld, J. Chem. Phys. **141**, 094101, 2014.

[121] Y.-H. Hwang-Fu, W. Chen, and Y.-C. Cheng, Chem. Phys. **447**, 46–53, 2015.

[122] Y. Chang and Y.-C. Cheng, J. Chem. Phys. **142**, 034109, 2015.

[123] T.-C. Dinh and T. Renger, J. Chem. Phys. **145**, 034105, 2016.

[124] V. I. Novoderezhkin, M. A. Palacios, H. van Amerongen, and R. van Grondelle, J. Phys. Chem. B **109**, 10493–10504, 2005.

[125] D. Rutkauskas, V. Novoderezkhin, R. J. Cogdell, and R. van Grondelle, Biochemistry **43**, 4431–4438, 2004.

[126] V. I. Novoderezhkin, D. Rutkauskas, and R. van Grondelle, Biophys. J. **90**, 2890–2902, 2006.

[127] L. Valkunas, J. Janusonis, D. Rutkauskas, and R. van Grondelle, J. Lumin. **127**, 269–275, 2007.

[128] V. I. Novoderezhkin, T. A. Cohen Stuart, and R. van Grondelle, J. Phys. Chem. A **115**, 3834–3844, 2011.

[129] J. Meldaikis, O. Zerlauskiene, D. Abramavicius, and L. Valkunas, Chem. Phys. **423**, 9–14, 2013.

[130] K. L. M. Lewis, F. D. Fuller, J. A. Myers, C. F. Yocum, S. Mukamel, D. Abramavicius, and J. P. Ogilvie, J. Phys. Chem. A **117**, 34–41, 2013.

[131] V. I. Novoderezhkin, A. B. Doust, C. Curutchet, G. D. Scholes, and R. van Grondelle, Biophys. J. **99**, 344–352, 2010.

[132] M. Yang, J. Mol. Spectrosc. **239**, 108–114, 2006.

[133] S. Polyutov, O. Kühn, and T. Pullerits, Chem. Phys. **394**, 21–28, 2012.

[134] V. Butkus, L. Valkunas, and D. Abramavicius, J. Chem. Phys. **140**, 034306, 2014.

[135] G. U. Bublitz and S. G. Boxer, Annu. Rev. Phys. Chem. **48**, 213–242, 1997.

[136] O. J. G. Somsen, V. Chernyak, R. N. Frese, R. van Grondelle, and S. Mukamel, J. Phys. Chem. B **102**, 8893–8908, 1998.

[137] O. Nanba and K. Satoh, Proc. Natl. Acad. Sci. U. S. A. **84**, 109–112, 1987.

[138] P. J. van Leeuwen, M. C. Nieveen, E. J. van de Meent, J. P. Dekker, and H. J. van Gorkom, Photosynth. Res. **28**, 149–153, 1991.

[139] M. E. van Brederode and R. van Grondelle, FEBS Lett. **455**, 1–7, 1999.

[140] V. I. Prokhorenko and A. R. Holzwarth, J. Phys. Chem. B **104**, 11563–11578, 2000.

[141] B. A. Diner, E. Schlodder, P. J. Nixon, W. J. Coleman, F. Rappaport, J. Lavergne, W. F. J. Vermaas, and D. A. Chisholm, Biochemistry **40**, 9265–9281, 2001.

[142] A. R. Holzwarth, M. G. Müller, M. Reus, M. Nowaczyk, J. Sander, and M. Rögner, Proc. Natl. Acad. Sci. U. S. A. **103**, 6895–6900, 2006.

[143] E. Romero, I. H. M. van Stokkum, V. I. Novoderezhkin, J. P. Dekker, and R. van Grondelle, Biochemistry **49**, 4300–4307, 2010.

[144] J. R. Durrant, D. R. Klug, S. L. Kwa, R. van Grondelle, G. Porter, and J. P. Dekker, Proc. Natl. Acad. Sci. U. S. A. **92**, 4798–4802, 1995.

[145] J. Biesiadka, B. Loll, J. Kern, K.-D. Irrgang, and A. Zouni, Phys. Chem. Chem. Phys. **6**, 4733–4736, 2004.

[146] B. Loll, J. Kern, W. Saenger, A. Zouni, and J. Biesiadka, Nature **438**, 1040–1044, 2005.

[147] W. Humphrey, A. Dalke, and K. Schulten, J. Mol. Graphics **14**, 33–38, 1996.

[148] L. Zhang, D.-A. Silva, H. Zhang, A. Yue, Y. Yan, and X. Huang, Nat. Commun. **5**, 4170, 2014.

[149] T. J. Frankcombe, Phys. Chem. Chem. Phys. **17**, 3295–3302, 2015.

[150] R. N. Frese, M. Germano, F. L. de Weerd, I. H. M. van Stokkum, A. Y. Shkuropatov, V. A. Shuvalov, H. J. van Gorkom, R. van Grondelle, and J. P. Dekker, Biochemistry **42**, 9205–9213, 2003.

[151] Y. Shibata, S. Nishi, K. Kawakami, J.-R. Shen, and T. Renger, J. Am. Chem. Soc. **135**, 6903–6914, 2013.

[152] J. Adolphs, F. Müh, M. E.-A. Madjet, and T. Renger, Photosynth. Res. **95**, 197–209, 2008.

[153] T. Renger and F. Müh, Photosynth. Res. **111**, 47–52, 2012.

[154] T. Renger, M. E.-A. Madjet, M. Schmidt am Busch, J. Adolphs, and F. Müh, Photosynth. Res. **116**, 367–388, 2013.

[155] M. A. Lomize, A. L. Lomize, I. D. Pogozheva, and H. I. Mosberg, Bioinformatics **22**, 623, 2006.

[156] F. Müh and T. Renger, "Structure-Based Calculation of Pigment–Protein and Excitonic Pigment–Pigment Coupling in Photosynthetic Light-Harvesting Complexes", in: *The Biophysics of Photosynthesis*, ed. by J. Golbeck and A. van der Est (Springer, New York, 2014), pp. 3–44.

[157] M. Rätsep, J. Linnanto, and A. Freiberg, J. Chem. Phys. **130**, 194501, 2009.

[158] M. Germano, A. Shkuropatov, H. Permentier, R. Khatypov, V. Shuvalov, A. Hoff, and H. Van Gorkom, Photosynth. Res. **64**, 189–198, 2000.

[159] M. Germano, A. Y. Shkuropatov, H. Permentier, R. de Wijn, A. J. Hoff, V. A. Shuvalov, and H. J. van Gorkom, Biochemistry **40**, 11472–11482, 2001.

[160] L. Konermann and A. R. Holzwarth, Biochemistry **35**, 829–842, 1996.

[161] E. G. Andrizhiyevskaya, D. Frolov, R. van Grondelle, and J. P. Dekker, Phys. Chem. Chem. Phys. **6**, 4810–4819, 2004.

[162] K. V. Price, R. M. Storn, and J. A. Lampinen, *Differential Evolution. A Practical Approach to Global Optimization*, Natural Computing Series (Springer-Verlag, Berlin, 2005).

[163] D. Ardia, K. M. Mullen, B. G. Peterson, and J. Ulrich, *DEoptim: Differential Evolution in R*, version 2.2-3 (2015).

[164] C. Eijckelhoff, F. Vácha, R. van Grondelle, J. P. Dekker, and J. Barber, Biochim. Biophys. Acta **1318**, 266–274, 1997.

[165] F. Vácha, D. M. Joseph, J. R. Durrant, A. Telfer, D. R. Klug, and J. Barber, Proc. Natl. Acad. Sci. U. S. A. **92**, 2929–2933, 1995.

[166] F. Vácha, M. Durchan, and P. Šiffel, Biochim. Biophys. Acta **1554**, 147–152, 2002.

[167] P. J. van Kan, S. C. Otte, F. A. Kleinherenbrink, M. C. Nieveen, T. J. Aartsma, and H. J. van Gorkom, Biochim. Biophys. Acta **1020**, 146–152, 1990.

[168] I. V. Shelaev, F. E. Gostev, V. A. Nadtochenko, A. Y. Shkuropatov, A. A. Zabelin, M. D. Mamedov, A. Y. Semenov, O. M. Sarkisov, and V. A. Shuvalov, Photosynth. Res. **98**, 95–103, 2008.

[169] I. Shelaev, F. Gostev, M. Vishnev, A. Shkuropatov, V. Ptushenko, M. Mamedov, O. Sarkisov, V. Nadtochenko, A. Semenov, and V. Shuvalov, J. Photochem. Photobiol., B **104**, 44–50, 2011.

[170] K. Acharya, B. Neupane, V. Zazubovich, R. T. Sayre, R. Picorel, M. Seibert, and R. Jankowiak, J. Phys. Chem. B **116**, 3890–3899, 2012.

[171] V. Butkus, D. Zigmantas, L. Valkunas, and D. Abramavicius, Chem. Phys. Lett. **545**, 40–43, 2012.

[172] V. Butkus, L. Valkunas, and D. Abramavicius, J. Chem. Phys. **137**, 044513, 2012.

[173] Y. Tanimura, J. Phys. Soc. Jpn. **75**, 082001, 2006.

[174] R. Kubo, M. Toda, and N. Hashitsume, *Statistical Physics II: Nonequilibrium Statistical Mechanics* (Springer-Verlag, Berlin, 1985).